Krzysztof Wiśniewski

Kaon and Antikaon production in Heavy-Ion Collisions for the reactions Ru+Ru and Ru+Zr at 1.69 AGeV beam kinetic energy

PhD Thesis supervised by
dr hab. Krystyna Siwek-Wilczyńska

Institute of Experimental Physics
Warsaw University

June 2000

Contents

List of Figures

Chapter 1

Introduction

Heavy-ion collisions at beam kinetic energies between 1 and 2 GeV per atomic mass unit are very complex processes. It is commonly believed that in the early phase of a central collision a highly dense and hot system is formed. The matter is compressed to a density which exceeds 3 times the normal nuclear matter density ($\rho_0 \simeq 0.16\ \frac{\mathrm{nucl.}}{\mathrm{fm}^3}$), and is heated to a temperature in the order of 100 MeV [1]. About 10 fm/c ($3.3 \cdot 10^{-23}$ s) after the beginning of the reaction, the compression energy starts being released in the form of a collective expansion of the system. This leads to a so-called freeze-out of the participating matter after about 30 fm/c. The available energy is sufficiently high so that internal degrees of freedom of nucleons are excited, and other baryons and mesons are produced.

It is very important that the system which is formed during the collision stays in the hot and dense state for a considerably long period of time, longer than the strong-interaction time scale $\simeq 10^{-24}$ s. Thus, for example, heavy-ion experiments are uniquely suitable for studying the compressibility of the nuclear matter far from its ground state (ρ_0, T=0) and for testing parameters of the nuclear equation of state (EOS).

Yet, due to their complexity, heavy-ion experiments are difficult to carry out and interpret. Often conclusions can be drawn only from comparing the experimental results to the predictions of the microscopic, non-equilibrium transport models, like Quantum Molecular Dynamics (QMD) [2, 3] or Boltzmann-Uehling-Uhlenbeck (BUU) [4, 5] models.

Another major problem is the lack of observables that reflect directly the collision scenario, especially its early phase, when the high density is reached, and the most interesting phenomena take place. The weakly interacting probes (leptons) can escape the dense zone undisturbed, but their abundances are scarce. In spite of that, a few experiments aim (or will aim) at the detection of the weakly interacting products of the heavy-ion reactions [6, 7, 8].

The hadronic matter, produced very abundantly during the collisions, interacts strongly. Thus, the information possibly carried out by the hadronic probes is obscured by the copious final-state interactions. Nonetheless, recently there has been a considerable effort, both experimentally and theoretically, to investigate the production of *strange* hadrons, among which K^+ and K^- mesons were of particular interest.

The K^+ meson consists of the $u\bar{s}$ pair, whereas the K^- meson is made of $\bar{u}s$ pair. The threshold kinetic energy for the production of K^+ mesons in an elementary, nucleon-nucleon collision on a stationary target, $\mathrm{NN}\rightarrow\mathrm{K}^+\mathrm{YN}$, is of the order of 1.6 GeV (Y being a strange hyperon Λ or Σ). The threshold kinetic energy for the K^- mesons production in the process $\mathrm{NN}\rightarrow\mathrm{NNK}^+\mathrm{K}^-$ is around 2.5 GeV.

Many predictions based on transport-model calculations show consistently that at beam energies in the range from 1 to 2 A GeV, which are near or below the threshold energies, strange mesons are produced in the early phase of the collisions, in the dense and hot reaction zone. The dominant production channels go via many-step processes, and involve intermediate baryon resonances and/or pions [9]. This interesting hypothesis is supported by the experimental observation that there are more K^+ mesons produced per participant in central than in peripheral Au+Au collisions at 1 A GeV beam kinetic energy [10].

Strange particles are in a sense different from other hadronic probes. They contain the s quark. Strangeness is conserved in the strong interactions. Thus, for example, strange and antistrange particles are produced together, like in the elementary processes mentioned above. Strange particles decay weakly. The mean life time of both K^+ and K^- mesons is 12.37 ns, which corresponds to $c\tau$ of about 3.7 m. The most important decay modes are the leptonic one into the (μ, ν_μ) pair (63.5% branching ratio) and the hadronic one into the (π, π^0) pair (21.2% branching ratio) [11].

Once produced, the strangeness can rarely be re-absorbed during the collision. For a strong interaction this would require a collision of particles that contain the s and $\bar{s}$ quarks, which is not very likely. On the other hand, weak processes, which may not conserve strangeness, occur very rarely by themselves.

There is, however, a tremendous difference between the interactions of K^+ and K^- mesons in the hadronic matter, especially at low relative momenta [12]. K^- mesons can easily interact with nucleons to form Λ or Σ resonances, of which the strangeness content is the same as that of the K^- mesons (S=-1). Therefore, the cross section for the reaction $\mathrm{K}^-\mathrm{N}\rightarrow\pi\mathrm{Y}$ is relatively high – in vacuum, $\sigma\simeq$45–100 mb for momenta lower than 0.7 GeV/c [13]. Due to the anti-strange quark content, K^+ meson interact mainly elasticly. For momenta lower than 0.7 GeV/c the cross section of the elastic scattering $\mathrm{K}^+\mathrm{N}\rightarrow\mathrm{K}^+\mathrm{N}$ is in the order of $\simeq$10 mb [14]. This corresponds to a relatively long mean-free path, which at the normal nuclear matter density would be about 5-7 fm. The dominant charge-exchange process $\mathrm{K}^+n\rightarrow\mathrm{K}^0p$ has a 2–10 times smaller cross section [15]. Therefore, particularly K^+ mesons are considered to be penetrating probes and a promising tool to infer information about the conditions reached in the early phase of a collision.

First heavy-ion experiments that aimed at studies of strange-particle production slightly above the threshold energies were performed in the early 80's in Berkeley and in Dubna. The Λ hyperon production was investigated with streamer chambers [16, 17, 18], whereas the production of K^+ mesons was studied with magnetic spectrometers [19, 20]. Experiments on subthreshold production of K^- mesons were performed at BEVALAC [20] and, later, with the Fragment Separator at SIS [21]. Already at that time, an enhanced production rate of K^- meson was observed as compared to theoretical predictions.

In heavy ion collisions, the abundances of produced particles depend directly on the bulk properties of the nuclear matter, the EOS, and the collision scenario. Already in early theoretical works [22], it was suggested that, depending on the parameters of the EOS, the K^+ meson yield in central Au+Au collisions at 0.7 A GeV beam kinetic energy can change 2-3 times. A systematic comparison of the K^+ meson production rates for systems of different sizes and energies to the predictions of the QMD transport model favoured the soft EOS, with a small value of the incompressibility parameter, $\kappa \simeq 200$ MeV [23, 24, 25]. The discussion presented recently in [26] addressed the question of thermal equilibrium of the reaction products. It was argued that the final-state momentum-space distribution of K^+ mesons in Ni+Ni collisions at 1.93 A GeV beam kinetic energy is compatible with an isotropic emission pattern with a radial flow component. In contrast, the results obtained for reactions at higher beam energies suggested a sizable anisotropy due to the longitudinal expansion of the system [27].

In this work greater emphasis is put on another subject connected to the production of strange mesons, for which heavy ion experiments offer excellent testing grounds. The studies of in-medium modifications of hadron properties, their effective masses and interactions, were triggered by the idea of the breakdown and the restoration of the chiral symmetry of Quantum Chromodynamics (QCD) [28, 29, 30]. In the low energy limit, the properties of QCD are defined by the symmetries of its Lagrangian. In a world of an exact chiral symmetry, all the quarks should be massless. From the hadron masses, which are evidently not equal to zero, it is obvious that this state is not realized by nature and that the QCD Lagrangian contains terms which are not chirally symmetric. These terms, with the light quark masses in the order of : $m_u \simeq 5$ MeV/c^2, $m_d \simeq 9$ MeV/c^2, $m_s \simeq 175$ MeV/c^2 [31, 32], mix the left- and right-handed quarks, and break the symmetry of QCD explicitly. Moreover, since the hadron-mass spectrum does not exhibit systematic degeneracy with respect to parity, it is believed that the symmetry of QCD is broken spontaneously as well. However, it is also anticipated that the spontaneously broken symmetry of QCD is partially restored in a compressed and hot baryonic matter [29, 33]. And, as the symmetry governs the properties of hadrons, its restoration should manifest itself in modifications of hadron interactions and effective masses in a dense and hot environment [34, 35], such as that reached in heavy-ion collisions.

The in-medium modifications of kaons were first investigated theoretically in [36, 37]. Since then, it has become questionable whether these effects originate directly from the restoration of the chiral symmetry, as anticipated hitherto [34]. Nonetheless, at present, a wide variety of theoretical approaches still predict consistently that the K^+-nucleon interaction should become slightly more repulsive and the K^--

nucleon potential strongly attractive in the dense nuclear environment [39]. In other words, it is expected that in the medium the kaon effective masses change. The K^+ meson mass increases slightly, while the K^- meson mass drops considerably with increasing baryon density. This phenomenon is of particular interest, as it would lead to the formation of a kaon condensate in a dense nuclear matter [36, 37], which, in turn, would have consequences for the evolution of neutron stars. As pointed out in [40], stars with masses smaller then previously estimated would collapse into black holes.

The evidence for the modifications of kaon properties at low densities is based on the analysis of K^+-nucleus scattering [41] and on the studies on kaonic atoms [42]. The results of K^+-nucleus scattering experiments favour moderate repulsion of the K^+N interaction at the normal nuclear matter density (ρ_0), which is what one expects on grounds of K^+-nucleon scattering lengths [43, 44]. On the other hand, the results on kaonic atoms imply considerable attraction of the K^-N interaction at ρ_0, whereas from the empirical K^--nucleon scattering lengths [43] it is expected that the K^-N interaction is repulsive. As pointed out in [38], this transition, from repulsion in vacuum to attraction at non-vanishing densities, can be understood as an effect of the in-medium modifications of the $\Lambda(1405)$ properties.

In heavy-ion collisions higher densities are reached. Therefore, the in-medium effects can be probed in conditions in which they are thought to be much more pronounced. One expects that their influence on kaons is twofold.

First of all, because the kaon effective masses are modified, the production threshold energies change. It means a small reduction of the production rate of K^+ mesons, of which the effective mass is supposed to grow slightly, and a substantial rise of the production rate of K^- mesons, the effective mass of which is thought to drop considerably. This hypothesis was confirmed experimentally by the results of the KaoS collaboration [45]. The K^+ and K^- meson yields were measured at around mid-rapidity in Ni+Ni collisions at two beam energies equally distant from the threshold energies for the production of mesons in elementary, NN collisions. The production cross sections of both meson species turned out to be similar at these equivalent energies, whereas the respective production rates in NN collisions slightly above the production thresholds differ by one order of magnitude. This intriguing result, which indeed suggested the changes of the kaon effective masses and production threshold energies, needs to be confirmed by independent measurements, possibly in different regions of the momentum space. However, it was suggested recently that in heavy ion experiments, the chaotic as well as the coherent movement of the baryonic matter may additionally mask the effect of the in-medium potentials on the measured antikaon yields [46].

Secondly, the effective kaon-nucleon potentials change as kaons propagate in the nuclear medium of varying density. The gradients of potentials, i.e., forces acting on kaons, are thought to modify their final-state phase-space distributions. In particular, K^+ mesons are expected to be pushed away from the regions of high baryon density by a slightly repulsive potential, while K^- mesons are thought to be attracted towards the dense collision zone by a strongly attractive force. In order to investigate this problem, the FOPI collaboration measured the directed side-flow pattern of K^+ mesons in the Ni+Ni system at 1.93 A GeV beam kinetic energy [47]. It was shown that K^+ mesons do not flow in the direction of baryons. This is surprising because the flow of Λ hyperons, which are produced together with K^+ mesons, clearly follows the proton flow. The observation was interpreted as a hint for additional repulsion felt by K^+ mesons during the propagation through the medium. Comparison of the result to the predictions of transport models revealed that it can be understood as an effect of the in-medium modifications of the K^+N potential [48]. However, it was pointed out that if the momentum dependence of the K^+N interaction is properly taken into account, the sensitivity of the observable to in-medium effects gets considerably reduced [49]. It was also suggested that the effect may depend strongly on the lifetimes of the nuclear resonances which are used in the model calculations [50]. Recently, the azimuthal anisotropy of the K^+ meson phase-space distribution was observed in the Au+Au system at 1 A GeV beam kinetic energy [51]. The results were compared to the predictions of a transport model, and again interpreted as a hint for the in-medium modifications of kaons. Certainly more experimental evidence is needed in order to elucidate the outstanding questions.

In this work, the measurements on K^+ and K^- mesons in ^{96}Ru+^{96}Ru and ^{96}Ru+^{96}ZrO$_2$ collisions at 1.69 A GeV beam kinetic energy are reported. The data were taken in 1996 with the FOPI detector system, installed on the beam of SIS at GSI/Darmstadt. The question of the in-medium modifications of kaons is addressed by comparing the experimental results to the predictions of the RBUU transport model of the Giessen group. Some detailed information about the model is given in Appendix A.4.

The work is organized in the following way. In Chapters 2 and 3, the details about the experiment, about the detector setup, and about the data analysis are given. In Chapter 4, the method and results of extracting the freeze-out conditions by analysis of pion, proton, and deuteron spectra is presented. In Chapter 5, the kaon identification procedure is described. In Chapter 6, the final-state momentum-space distribution of K^+ mesons and the centrality dependence of the K^+ mesons production are discussed. It is shown that the accuracy of the measurements does not allow to draw firm conclusions about the in medium effects on kaons. On the other hand, the results are exploited for studying the thermal and chemical equilibrium of the system. In Chapter 7, the directed side-flow pattern of K^+ mesons and the dependence of the measured signal on the transverse momentum are discussed. The comparison of the results to the predictions of the RBUU transport model reveals that there is a potentially high sensitivity of these observables to the in-medium effects on kaons. The experimental observations are best understood if the modifications of the K^+ meson effective mass are taken into account in the model. In Chapter 8, the K^- to K^+ meson yield ratio is studied. It is shown that the yield ratio varies across the measured fraction of the momentum space. It is argued that the observation can neither be explained as the effect of the final-state interactions nor can it have a purely kinematical origin. The experimental results can be reproduced by the RBUU transport model only if the in-medium modifications of kaons are considered. In Chapter 9, the concluding remarks are given.

Chapter 2

Experiment

2.1 Beam and target

The accelerator facility at Gesellschaft für Schwerionenforschung (GSI) in Darmstadt, which includes, among others, the Schwerionensynchrotron (SIS), nowadays delivers beams of light and heavy ions as well as protons and pions. In the case of ion beams, the available beam kinetic energy per atomic mass unit is described by the formula

$$E_{\text{beam}}/A = m_{\text{proton}}c^2 \left(\sqrt{1 + \left(\frac{B\rho \cdot c}{m_{\text{proton}}c^2} \frac{Q}{A} \right)^2} - 1 \right) . \tag{2.1}$$

Q and A denote the charge and the mass number of beam ions. $B\rho$ is the rigidity of the synchrotron. The maximum value for the rigidity of SIS equals 18.7 Tm. Hence, the available beam kinetic energies are as high as 2 GeV per nucleon.

In September 1996, a series of experiments was performed at SIS with the beams of $^{96}_{44}\text{Ru}$ and $^{96}_{40}\text{Zr}$ isotopes on $^{96}_{44}\text{Ru}$ and $^{96}_{40}\text{Zr}^{16}_{8}\text{O}_2$ targets. There were two primary goals of these experiments :

- investigation of transparency of the nuclear matter and its dependence on the collision energy,
- investigation of strange meson production.

According to formula 2.1, the available beam kinetic energy grows with the charge of the beam ions. On the other hand, the beam intensities decrease with increasing ion charge. For the Ru beam, the highest charge state that could be used in order to keep a sufficient beam intensity was the 42+ charge state. The resulting beam kinetic energy was 1.69 A GeV. The beam energy was slightly lower (1.58 A GeV) in the case of the Zr beam because the highest used charged state was 41+.

At about 2 A GeV beam kinetic energy, the production rate of K^+ mesons is in the order of 1 per 10 central collisions. It decreases rapidly with decreasing beam energy. The dependence of the production cross section of K^+ mesons on the beam kinetic energy can be approximated by the formula [26]

$$\sigma(K^+) \simeq (E_{\mathrm{beam}})^{5.3} . \tag{2.2}$$

At the same energy, the production cross section of K^- mesons is typically an order of magnitude lower [45]. Therefore, in this work, which concentrates on the production of both K^+ and K^- mesons, only reactions with the $^{96}_{44}$Ru beam at the highest kinetic energy of 1.69 A GeV were investigated. The production rate of K^- mesons was too low in the case of the reactions at lower beam energies.

Two target foils were used :

- 430 mg/cm^2 of Ru,
- 380 mg/cm^2 of ZrO_2.

Both target thicknesses were chosen to assure about 1% probability of reactions of the beam ions with the Ru and Zr nuclei from the target. The beam spills were typically 10–12 second long. In order to keep the reaction rate during the spills below $5 \cdot 10^2$ Hz (as required by the operation conditions of the detector apparatus), the beam intensity was kept below $5 \cdot 10^4$ ions per second. This corresponded to an average time interval between two incoming ions in the order of 20 μs. In these conditions, the average time between two reactions was about 2 ms.

The target foils were placed inside the FOPI detector setup, which will be described in greater detail in the following section.

2.2 The FOPI detector setup

The FOPI detector system [52, 53] is a general purpose, modular setup of several subdetectors, used for fixed target experiments. It has a nearly complete azimuthal symmetry and almost full geometrical acceptance[1]. A schematic view of the detector is shown in Figure 2.1.

The FOPI system is capable to detect simultaneously charged reaction products: heavy fragments of Z up to 20, light fragments (protons, deuterons, tritons) and mesons (pions, kaons, etc.). Particles are identified and their four-momenta are determined by the measurements of the specific energy loss in the detector material (dE/dx), the track curvature radius in the magnetic field (ρ), and the velocity (v), derived from the information on time-of-flight from the target position to the detector (TOF). In addition, shortly-lived neutral particles are identified by invariant mass reconstruction of their decay products.

---

[1] The name "FOPI" is an abbreviation of "*FOur PI*", and originates from the large, nearly completely 4π geometrical acceptance of the setup.

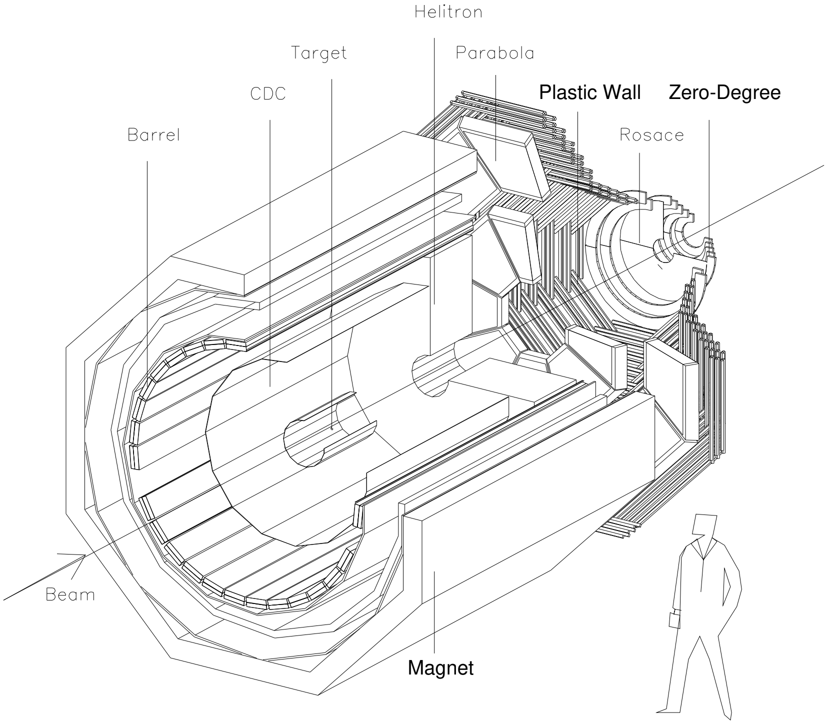

Figure 2.1: *The FOPI detector setup.*

2.2.1 Phase 1

The forward part of the FOPI setup, i.e., the so-called Phase 1, was completed in 1990 [52]. It consists of two systems of scintillating strips: the Zero Degree (ZD) and the Plastic Wall (PLAWA) detectors. The ZD detector allows the detection of charged particles emitted from the target position at laboratory polar angles (Θ_{lab}) between 1.2° and 7.5° over the full azimuthal range. The PLAWA detector covers the full azimuth of the polar angles from 7° to 30°. Both detectors provide the information about the TOF and the energy deposited by particles in the scintillator material (ΔE).

Identification of particles is possible for sufficiently high velocities, higher than the punch-through velocity. In such cases, the information about ΔE allows to determine the specific energy loss, dE/dx, of a particle. In order to provide the information on dE/dx for particles of which velocities are lower than the punch-through velocity, the Parabola (ionization chamber) and the Rosace (thin scintillator wall) were usually placed in front of the PLAWA and the ZD detectors respectively[2].

The information on dE/dx and v allows to derive easily particle charge but not particle mass (cf. formula A.1, and notice that the dE/dx of a particle passing through matter does not depend explicitly on its mass). Therefore, Phase 1 detectors are capable (only) of particle identification with respect to their charge. A series

---

[2] Since 1994, when the forward drift chamber, Helitron, was introduced to the detector setup, Parabola has no been used any more.

of successful experiments which focused on the production of nuclear fragments followed the completion of the Phase 1 system [54, 55, 56, 57, 58]. For almost all practical purposes of those experiments, an estimate that the mass of a fragment is given by $M_{fr}= 2\times Z_{fr}$ was sufficiently accurate.

Unfortunately, PLAWA and ZD detectors can not be used for the identification of K^+ and K^- mesons, which requires particle mass determination. Therefore, in this work, the information from Phase 1 detectors is used only for determining global event characteristics, like collision centrality or orientation of the reaction plane (see Sections 3.2 and 3.3 for details).

2.2.2 Phase 2

Phase 2 of the FOPI setup [53] was designed for experiments with beams of higher kinetic energies, up to maximal energies delivered by the SIS. Only lighter nuclear fragments survive such high-energy collisions. Moreover, the internal degrees of freedom of nucleons participating in the reactions are excited, and particles like pions, kaons and antikaons are produced. For their identification the information about their mass, not only charge, is essential. Phase 2 of FOPI was built to meet the requirement of particle mass determination. Its completion was followed by experiments which focused mainly on the production of mesons [47, 59, 26, 60].

Phase 2 of FOPI consists of the tracking device – Central Drift Chamber (CDC) – and the Plastic Scintillator Barrel (cf. Figure 2.1). Both detectors operate in the magnetic field of 0.6 T, homogenous and parallel to the beam axis (z), which is produced by the superconducting solenoid. The Barrel surrounds the CDC and provides additional reliability of the particle identification. Detailed information about the operation of the CDC and the Barrel as well as about the calibration procedures can be found in PhD theses [61, 62]. Here only the most important technical information will be given.

Up to 100 particles per central heavy-ion collision can make their way through the CDC. Figure 2.2 shows how such an event looks like in the plane perpendicular to the beam axis (xy). Dots represent individual hits from which particle tracks are reconstructed. The amount of energy lost by particles due to ionization is illustrated by the sizes of the dots. Trajectories of negatively and positively charged particles, depicted by the lines, are bent in opposite directions in the magnetic field. An average hit multiplicity per particle trajectory is about 50. Therefore, as many as 5000 hits can be registered in a single event. A correct assignment of hits to an appropriate trajectory is a serious challenge for the tracking algorithm, of which several different types are used [61, 63, 64]. Matching between tracks reconstructed in the CDC and hits registered in the Barrel [61, 62] (filled squares in Figure 2.2) brings in additional difficulty, but is necessary for identification of rare particles.

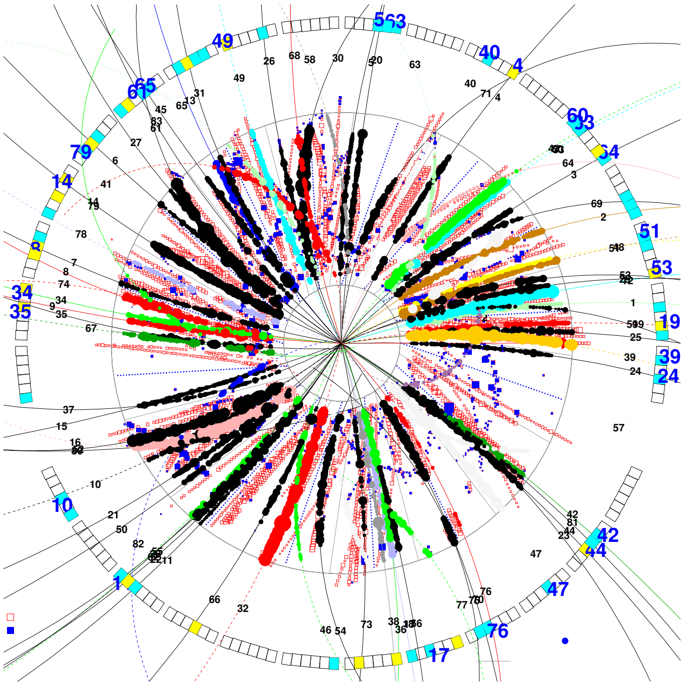

Figure 2.2: *Trajectories of charged products of a central Au+Au collision at 1 A GeV beam kinetic energy, as seen by the CDC and Barrel in the plane perpendicular to the beam axis. About 80 particle trajectories are reconstructed out of nearly 3800 hits.*

CDC

The CDC covers the full azimuth of the polar angles between 30° and 150°. It allows the tracking of charged particles at radial distances between 20 and 80 cm from target position. It is subdivided into 16 sectors in the xy plane. The view of one of the sectors in the xy plane is shown in Figure 2.3. In the middle of the sector, an anode plane is formed by 60 grounded read-out wires. A homogenous electric field of 750 V/cm is provided by the so-called drift wires located on the border of the sector and on the inner and outer radii of the chamber. In between the read-out wires, the potential wires, on -1.5 kV voltage, are located. They provide a strong electric field in the vicinity of the read-out wires so that charge multiplication can take place.

While passing through the CDC, charged particles ionize the gas, typically a mixture of 88% Argon, 10% isobutane, and 2% methane under the atmospheric pressure. The produced electrons drift towards the anode planes on straight trajectories, determined by the interplay between the electric and magnetic fields, with velocity in the order of 45 μm/ns. The maximum drift time of the electrons is about 5 μs. In the vicinity of each read-out wire, before the charge is collected, the multiplication of the charge occurs ($\times 10^3$). The signals are read on both ends of the read-out wires with a system of ADC's, which allows to digitize the complete signal shape over a 10 μs time interval.

The hit coordinates, i.e., the location at which the primary ionization took place, can be calculated back. From the arrival time of the signals on both ends of the wire, the hit position in the xy plane is derived with the accuracy of 300 μm. From the charge division between both ends of the wire, the hit coordinate along the z

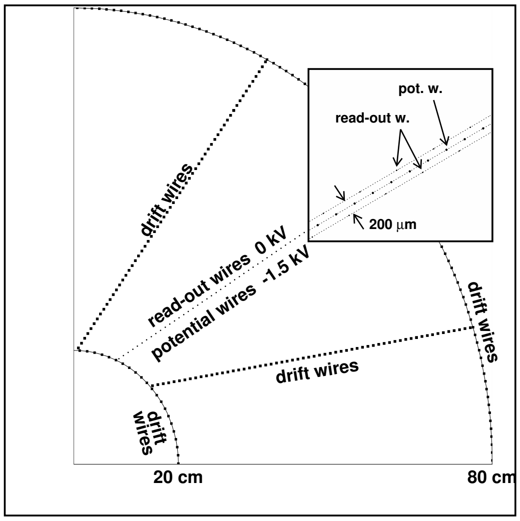

Figure 2.3: *A schematic view of one sector of the CDC in the plane perpendicular to the beam axis. The insert gives the magnified view of the anode plane in the middle of the sector. Staggering of the read-out wires on both sides of the anode plane can be observed.*

axis is deduced with a 5 cm accuracy. The energy loss of particle can be derived from the total charge collected on the wire, which is proportional to the primary ionization.

The tracking program groups individual hits to form particle trajectories, which are fitted with a helix curve. For each trajectory the curvature radius (ρ), the direction of emission (Θ_{lab} and ϕ_{lab}), and the mean value of the energy loss (dE/dx) are determined. The accuracy of dE/dx determination is momentum dependent. It varies form 5 to 15% with momenta increasing from 0.1 to 2 GeV/c.

The ratio of transverse momentum over charge of a particle is derived via formula

$$\frac{p_t}{Q} = B\rho \; . \tag{2.3}$$

The accuracy of p_t determination in the order of 5% to 15% is achieved.

Particle identification with the CDC

Figure 2.4a shows the identification plot in the form of a correlation matrix between the logarithm of dE/dx and the ratio p/Q of particles for which trajectories were reconstructed within the CDC. The data comes from the Ru+Ru experiment at 1.69 A GeV beam kinetic energy. The lines plotted on top of the data show the dependence of the specific energy loss on particle momenta, calculated according to the Bethe–Bloch formula A.1[3]. Figure 2.4b shows the mass spectrum, i.e., the projection of the matrix from panel (a) on the mass parameter in the Bethe–Bloch formula. The mass parameters are multiplied by -1 for particles of which trajectories have opposite curvature than proton trajectories. The plotted quantity is often called $Mass_{CDC}$ since its determination is based on the information delivered by the CDC only. The plot demonstrates a good separation between different particle

---

[3] Some modifications of formula A.1 are needed in order to account for non linear response of the detector.

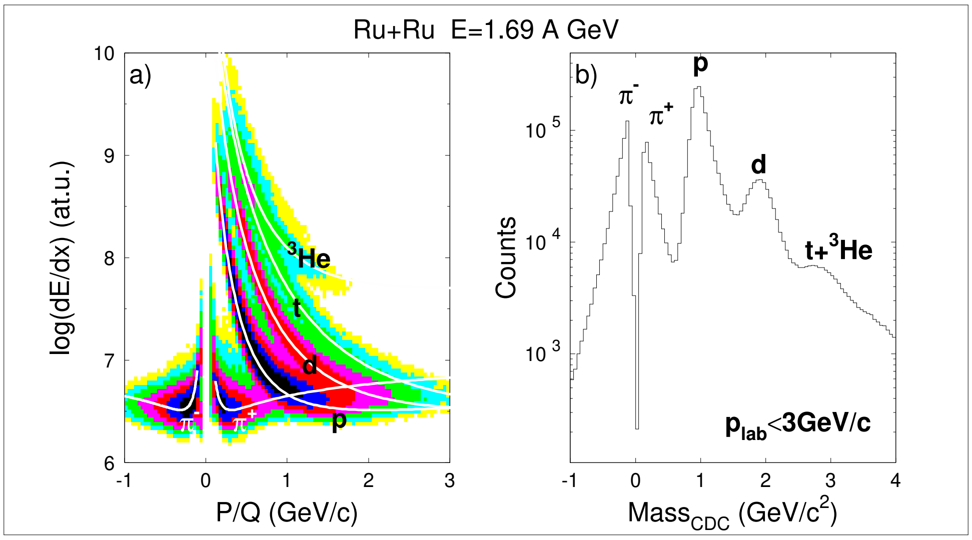

Figure 2.4: *Particle identification with the CDC. The data come from the Ru+Ru experiment at 1.69 GeV beam kinetic energy. (a) The matrix of correlations between energy loss dE/dx and ratio p/Q of particles. (b) The mass spectrum obtained by projection of the matrix from panel (a) on the mass parameter in the Bethe–Bloch formula.*

species: pions, protons and deuterons, which, however, gets worse with increasing momentum (cf. Figure 2.4a). Particles can be selected according to the values of the $Mass_{CDC}$ parameter. Studies on pions and on light fragments (p, d, t) are often performed using the information delivered by the CDC only.

Plastic Scintillator Barrel

The CDC is surrounded by the Plastic Scintillator Barrel, a set of 180 individual scintillator strips which form a cylinder of a 111 cm radius (cf. figures 2.1 and 2.2). The strips are 240 cm long, and have a 4×3 cm rectangular shape in cross section. It was originally planed that the polar-angle range covered by the Barrel matches that of the CDC. However, because of the high double-hit rate in the scintillator strips, the Barrel was moved backwards so that the opening angle, as seen from the target position, is currently $40° < \Theta_{lab} < 140°$. The Barrel covers about 85% of the full range in the azimuthal angle. Only two sets, of six strips each, are missing due to technical reasons (cf. Figure 2.2).

Scintillation light produced in a given strip by charged particles is collected on both strip ends by photomultipliers[4]. Both the light output and the arrival time of the signal are registered. The time is measured against the signal from the start detector (see Section 3.1 for more information). The delay due to the passage of the beam ions from the start detector to the target is subtracted.

---

[4] The role of the light guides which connect the scintillator strips with the photomultipliers is not discussed in this work.

The TOF of a particle from the target position to the point of the detection is derived via the formula

$$TOF = \frac{T_L + T_R}{2} - \frac{L}{2 \cdot v_{light}} , \tag{2.4}$$

where T_L and T_R denote the arrival time of the signal at the upstream and at the downstream ends of the strip respectively, and L=240 cm is the strip length. The accuracy of the TOF determination varies from strip to strip but is in the order of 300–400 ps.

The distance from the middle of the strip to the position at which a particle crossed the strip along the z axis (hit position) is derived via the formula

$$Z = \frac{T_L - T_R}{2} v_{light} . \tag{2.5}$$

$v_{light} \simeq 16$ cm/ns denotes the velocity of the light-pulse propagation in the scintillator material. The Z coordinate of the hit is determined with 8 cm accuracy, which is limited by the accuracy of time measurements. The hit position in the xy plane is given by the azimuthal angle ϕ of the strip with accuracy of 2°, limited by the dimensions of the strip.

The velocity of the particle is derived from the position of the hit and the TOF information via the relation

$$v = \frac{s}{TOF} = \frac{(2 \cdot \rho \cdot \arcsin(\frac{R_B}{2 \cdot \rho}))/\sin(\Theta_{lab})}{TOF} , \tag{2.6}$$

where s is particle flight path, ρ is curvature radius of particle trajectory in the magnetic field, Θ_{lab} is the emission polar angle, and R_B=111 cm is the radius of the Barrel.

In case if two or more adjacent strips of the Barrel register hits, the correspondence between TOF and the Z measurements on the subsequent strips is checked. When the differences in TOF and in the hit position along the z axis (ΔTOF and ΔZ) are smaller than 300 ps and 25 cm respectively, it is assumed that the hits originate from one particle, of which the trajectory is sufficiently bent so that it passed through several Barrel strips. The hit position and the TOF for this particle is taken from the strip which registered the highest energy deposited by the particle.

The operation of the CDC and the Barrel is essential for the analysis on which this work focuses. The procedure of particle identification with CDC–Barrel combined measurement will be described in greater detail in Chapter 5.

2.2.3 Helitron

The FOPI Phase 2 is completed by the Helitron (cf. Figure 2.1). It is the forward drift chamber, which will eventually play the same role as the CDC does in the backward hemisphere. It will add information about the mass to the charge derived

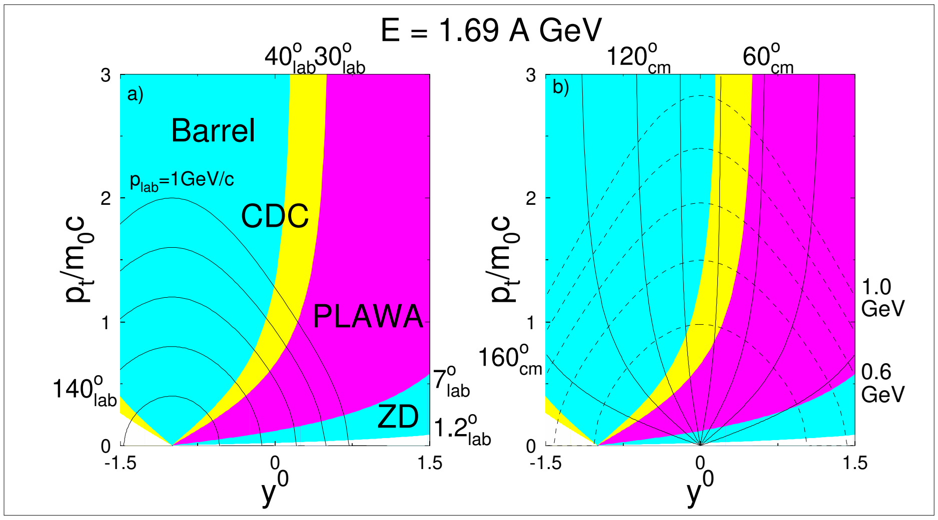

Figure 2.5: *The geometrical acceptance of the FOPI detector setup for a mass symmetric collision of a beam at 1.69 A GeV kinetic energy with a fixed target located in the middle of the setup. (a) The solid lines are drawn for kaons of momenta* p_{lab}*=0.2, 0.4, 0.6, 0.8 and 1.0 GeV/c. (b) The solid lines show different emission angles from* $\Theta_{cm}=20°$ *to* $\Theta_{cm}=160°$ *in 20° intervals. The dashed lines correspond to kaon kinetic energies in the center-of-the-momentum reference frame of* E^{kin}_{cm}*=0.2, 0.4, 0.6, 0.8 and 1.0 GeV.*

from the measurement by the Plastic Wall for particles emitted in the mid-rapidity region and at low transverse momenta. Most of the particle yields populate exactly this region of the momentum space. Therefore, it will be of high importance to combine the yields measured by the CDC in the backward direction with those estimated from the Helitron data. Among others, the effort to identify K^+ and K^- mesons with the Helitron is currently being pursued [65] but it is not described in this work. Here, no use is made out of the information from the Helitron.

2.2.4 Geometrical acceptance

In Figure 2.5a the geometrical acceptance of the individual subcomponents of the FOPI detector setup is shown for a mass-symmetric reaction of a beam at a kinetic energy of 1.69 GeV per nucleon. The acceptance is presented in terms of transverse momentum divided by the mass of a particle (p_t/m_0c)[5] versus the rapidity normalized to the rapidity of the center-of-the-momentum (CM) coordinate system $(y^{(0)})$ [6]. Due to the almost full coverage of the available momentum space, in an ideal case, only a small fraction of the charged reaction products will remain not detected by the FOPI setup.

---

[5] Particle mass is multiplied by the light velocity, c, in order to arrive at a dimensionless quantity.

[6] The definitions of the kinematic variables referred to throughout this work can be found in Appendix A.2.

Chapter 3

Event characteristics

Altogether around 4.8 million events were collected in the Ru+Ru experiment at 1.69 A GeV beam kinetic energy. The number of events registered in the Ru+ZrO_2 experiment at 1.69 A GeV beam kinetic energy was about 3.7 million.

3.1 Event Selection

Rejection of double interactions

From all the subdetectors of the FOPI setup the CDC has the longest operational dead-time. As mentioned in Section 2.2, the ADC system of CDC allows to digitize the complete signal shape over a 10 μs time interval, whereas the maximum drift-time of electrons in the CDC is about 5 μs. When a given event is accepted by the trigger system, it is important to assure that no reactions prior and after this event took place within a 5 μs time period. In an opposite case, a so-called double interaction is encountered and the events are mixed. Since the average time interval between two reactions is in the order of 2 ms, double interactions are in general rare.

In most of the cases, double interactions are rejected already on the trigger level, rejection being based upon the much faster signals from the plastic detectors of the Forward Wall and Barrel. In order to reject double interactions caused by two ions which came within a 100 ns time interval one after the other, the information from the start detector is needed. It is a thin scintillator placed about 2.5 m up-stream from the target. It registers both the arrival time and the energy deposited in the scintillator material by beam ions. Figure 3.1a shows the energy distribution of the signal from the start detector. A double-peak structure can be observed. The peak corresponding to a higher energy deposited by the beam ions (above the minimum in between the two peaks) is attributed to double interactions when two ions pass the start detector very shortly one after the other (within 100 ns interval of the QDC gate). The figure caption gives the condition which was used in order to reject double interaction from subsequent analysis.

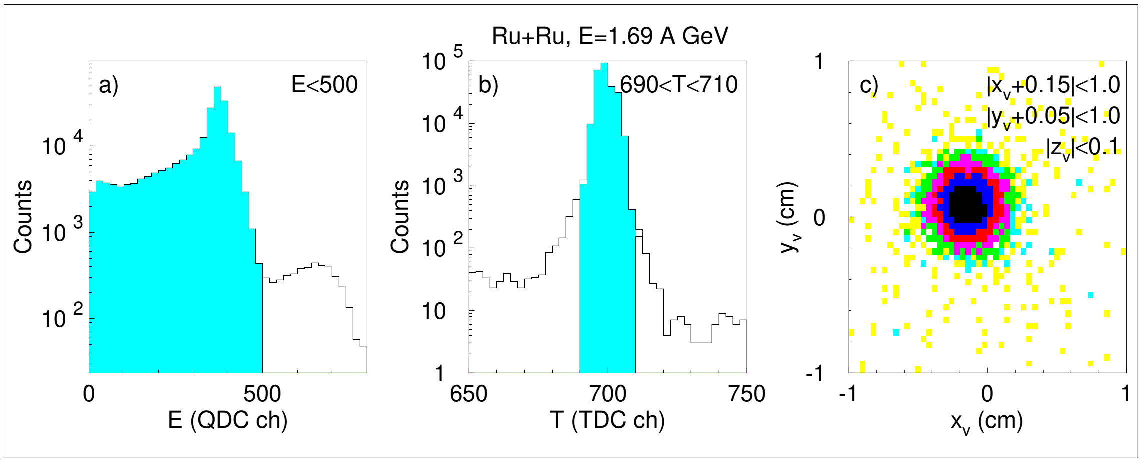

Figure 3.1: *(a, b) Time and energy spectra from the start detector. (c) The distribution of the coordinates of the event vertex in the plane perpendicular to the beam axis.*

The start detector delivers also the information about the reference time. Figure 3.1b shows the distribution of the arrival time of the signal from the start detector. The events for which the time was outside a certain limit around the central peak (indicated in the figure caption) were rejected as their reference time was wrong.

Rejection of non-target reactions

The halo detector, which is used to insure the focusing of the beam and as a veto device, consists of two components. The first one is a 2 mm thick scintillator with a cylindrical hole, 7 mm in diameter, placed close to the target. The second part is a 5 mm thick scintillator with a rectangular hole, 10 x 10 mm in cross section, located about 2.5 m upstream from the target, close to the start detector. In normal conditions 98–99% of the ions from the beam pass through the holes of the halo detector.

In order to further suppress the number of reactions that did not occur on target, the coordinates of the event vertex were calculated. First of all, the pairs of tracks in the CDC which intersect were found, and the coordinates of the interception points were calculated. The event-vertex coordinates (x_v, y_v, z_v) were computed as the mean values of the coordinates of the intersection points. The distribution of the event-vertex coordinates in the xy plane with respect to the target position is shown in Figure 3.1c. The caption indicates the conditions which are imposed in order to select only the reactions which took place on target.

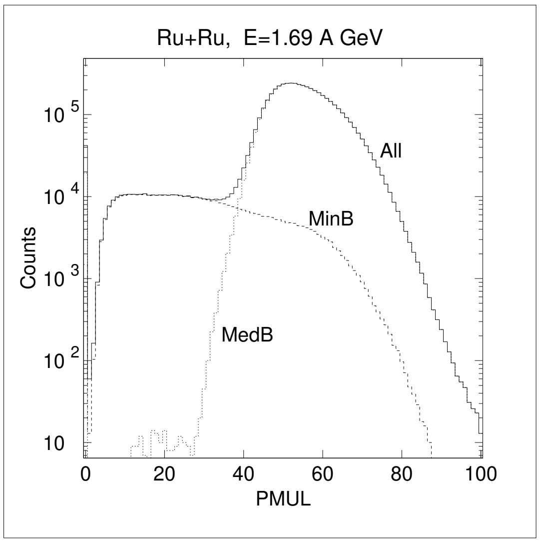

Figure 3.2: *The PMUL distributions for minimum-bias (dashed histogram) and medium-bias (dotted histogram) event samples in the Ru+Ru experiment. The sum of the two is depicted by the solid histogram.*

Minimum-bias and medium-bias event classes

Two samples of events were accumulated simultaneously during the experiment. The so-called minimum-bias event sample (MinB) was collected practically without any preselection. The second class, on the other hand, the so-called medium-bias sample (MedB), consisted of events which fulfilled the requirements of some minimum multiplicity of hits registered in the Plastic Wall. The selection was made on the hardware-trigger level. The threshold on the multiplicity was set as high as to select approximately 15% of all the events. Figure 3.2 shows the distributions of multiplicities of particles identified by the Plastic Wall (PMUL) for both considered event samples, collected in the Ru+Ru experiment. Usually some of the hits from the total hit multiplicity in the Plastic Wall can not be assigned to any of the identified particles. Therefore, the PMUL distribution for the MedB event sample shown in Figure 3.2 falls down gradually on the side of low PMUL instead of ending sharply at a certain threshold value.

It was assumed that because of the condition imposed on PMUL, the fraction of central collisions was enhanced in the MedB event sample. Since the production rate of kaons is higher in central than in peripheral collisions, the MedB event sample is of greater interest for the studies which are reported in this work. In order to allow to accumulate more central events within a limited speed of the data acquisition system, the storage rate of MinB events was scaled down by a factor of 32 (cf. Figure 3.2).

The method of selecting events according to their centrality is further discussed in the next section.

Rejection of Ru+O reactions

The rejection of the reactions of the Ru beam ions with the Oxygen nuclei in the ZrO_2 target was based on the multiplicity of detected particles. In Figure 3.3 the

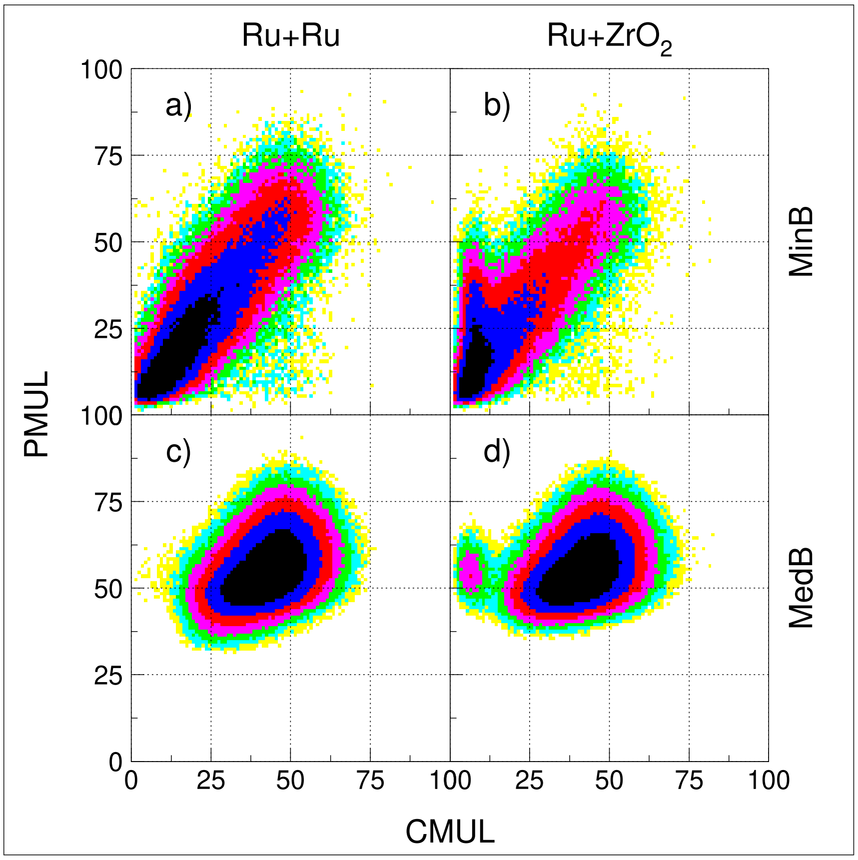

Figure 3.3: *The multiplicity of particles detected by the Plastic Wall (PMUL) versus the multiplicity of particles registered by the CDC (CMUL) in the Ru+Ru (left) and Ru+ZrO$_2$ (right) experiments. (a,b) The distributions for the minimum-bias event sample. (c,d) The distributions for the medium-bias event sample.*

multiplicity of particles registered by the Plastic Wall (PMUL) is plotted against the multiplicity of particles detected in the backward hemisphere by the CDC (CMUL). In the case of the Ru+Ru experiment (panel a), the more central the collisions are, the higher PMUL and CMUL they have. In contrast, in Figure 3.3b, which shows the multiplicities of particles in the Ru+ZrO$_2$ experiment, two separate branches can be noticed. The branch characterized by the weaker correlation between PMUL and CMUL corresponds to the reactions of the beam ions with the Oxygen nuclei in the ZrO$_2$ target. The reactions with Oxygen nuclei can have quite high PMUL, but they are forward peaked. Therefore, their CMUL (which measures the number of particles emitted in backward directions) remains low, even in the case of central collisions. The reactions with Oxygen nuclei in the target can not be, however, easily separated from the more peripheral reactions with Zr nuclei, of which both PMUL and CMUL are low.

Panels (c) and (d) in Figure 3.3 show PMUL plotted against CMUL for the medium-bias event sample in the Ru+Ru and Ru+ZrO$_2$ experiments, respectively. Because

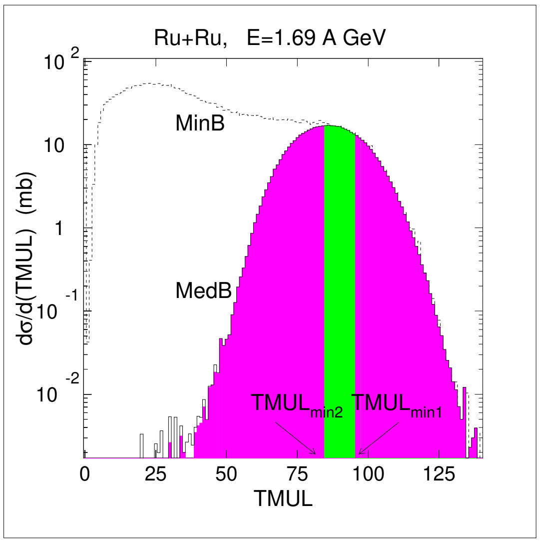

Figure 3.4: *The distributions of TMUL in the Ru+Ru experiment for minimum-bias (dashed histogram) and medium-bias (solid histogram) event samples. The histogram for the MinB event sample is normalized to the total geometrical cross section of the reaction. The division of the medium-bias sample into three event categories according to collision centrality is depicted with grey shaded areas.*

of the requirement of high PMUL, reactions with Oxygen nuclei can be eliminated from the MedB event sample by requiring CMUL to be higher than 15.

In this work, about 4.38 million and 3.39 million events from the MedB event samples were analysed in the case of the Ru+Ru and Ru+ZrO_2 experiments respectively (cf. Table 3.1). As described, the selection was made according to the conditions imposed on time and energy signals from the start detector, event-vertex coordinates, and multiplicities of detected particles.

3.2 Event centralities

It is commonly accepted that in heavy-ion collisions at intermediate energies the multiplicity of the reaction products is correlated with impact parameter of a collision [66]. In this work, the selection of events according to their centrality is based on the total multiplicity of particles detected by the CDC and by the Plastic Wall,

$$\mathrm{TMUL}=\mathrm{CMUL}+\mathrm{PMUL}\ . \tag{3.1}$$

The dashed histogram in Figure 3.4 shows the TMUL distribution for the MinB event sample weighted with the trigger efficiency. The trigger efficiency was defined by the dead-time of the data acquisition system. It was derived by comparing the number of collected events with the number of collisions expected from the total geometrical reaction cross section (Eq. 3.2). Thus, the dashed histogram in Figure 3.4 is normalized to the total geometrical cross section of the reaction

$$\sigma_{geo} = \pi \cdot (2 \cdot 1.2\ \mathrm{fm} \cdot 96^{1/3})^2 \simeq 3800\ \mathrm{mb}\ , \tag{3.2}$$

where the radius of a ^{96}Ru or ^{96}Zr nucleus is approximated by

$$R_{Ru} = R_{Zr} = 1.2 \cdot 96^{1/3}\ \mathrm{fm} \simeq 5.5\ \mathrm{fm}\ . \tag{3.3}$$

Assuming that there is a monotonic dependence of multiplicity of detected particles on impact parameter [66], the integration of the TMUL distribution from a given value TMUL$_{min1}$ to its upper end gives the value of $\Delta\sigma$ – the centralmost part of the cross section corresponding to the event sample selected with the condition TMUL>TMUL$_{min1}$. Using the geometrical sharp-cut-off model, one can estimate the maximal and the average impact parameters characterizing this event sample

$$b_{geo}^{max} = \sqrt{\Delta\sigma/\pi}\ , \tag{3.4}$$

$$< b >_{geo} = \frac{\int_0^{b_{geo}^{max}} b \cdot 2\pi b db}{\int_0^{b_{geo}^{max}} 2\pi b db} = 2/3 \cdot (b_{max})\ . \tag{3.5}$$

Using a participant-spectator model, one can subsequently calculate the number of nucleons participating in the reactions. In this model, the participant zone is the overlap volume of two spheres passing each other at a distance b. Each sphere has a radius equal to that of the nucleus $R_{Ru,Zr}$. On these assumptions, the mean number of participants characterizing the sample of events of which impact parameters are less than b_{geo}^{max} is equal to [67]

$$< A_{part} >= \frac{\int_0^{b_{geo}^{max}} (1 + (\frac{3}{\sqrt{2}} - 3)\frac{b}{R_{Ru,Zr}} + (3 - 2\frac{3}{\sqrt{2}})(\frac{b}{R_{Ru,Zr}})^2 + (\frac{3}{\sqrt{2}} - 1)(\frac{b}{R_{Ru,Zr}})^3) \cdot 2\pi b db}{\int_0^{b_{geo}^{max}} 2\pi b db}\ . \tag{3.6}$$

Similarly, one can assign the part of the cross section, $\Delta\sigma$, and the parameters $<b>_{geo}$ and $<A_{part}>$ to the sample of events of which TMUL are in any interval, for example, TMUL$_{min2}$<TMUL<TMUL$_{min1}$. Figure 3.5 shows the values of the parameters determined in this way for events of different TMUL grouped into 10-unit-wide bins.

In this work, the MedB event sample is analysed. The solid histogram in Figure 3.4 shows the TMUL distribution for the MedB event sample weighted with the MedB trigger efficiency. At the upper end, i.e., for very central collisions, where the hardware-trigger selection has no influence, the distribution matches that of the MinB event sample. The grey shaded areas illustrate the division of the MedB sample into three event subsamples which will be referred to in the following part of this work. The events are grouped according to their TMUL values. It is assumed that in this way event categories of different centralities are selected. However, due to fluctuations of TMUL, certainly events of quite different impact parameters may be mixed together in the considered subsamples.

For each subsample, the parameters $\Delta\sigma$, b_{geo}^{max}, $<b>_{geo}$, and $<A_{part}>$ were calculated via the TMUL distribution of the MedB sample shown in Figure 3.4, following the method sketched above. The values of these parameters, the TMUL ranges, and the statistics of the event subsamples are listed in Table 3.1.

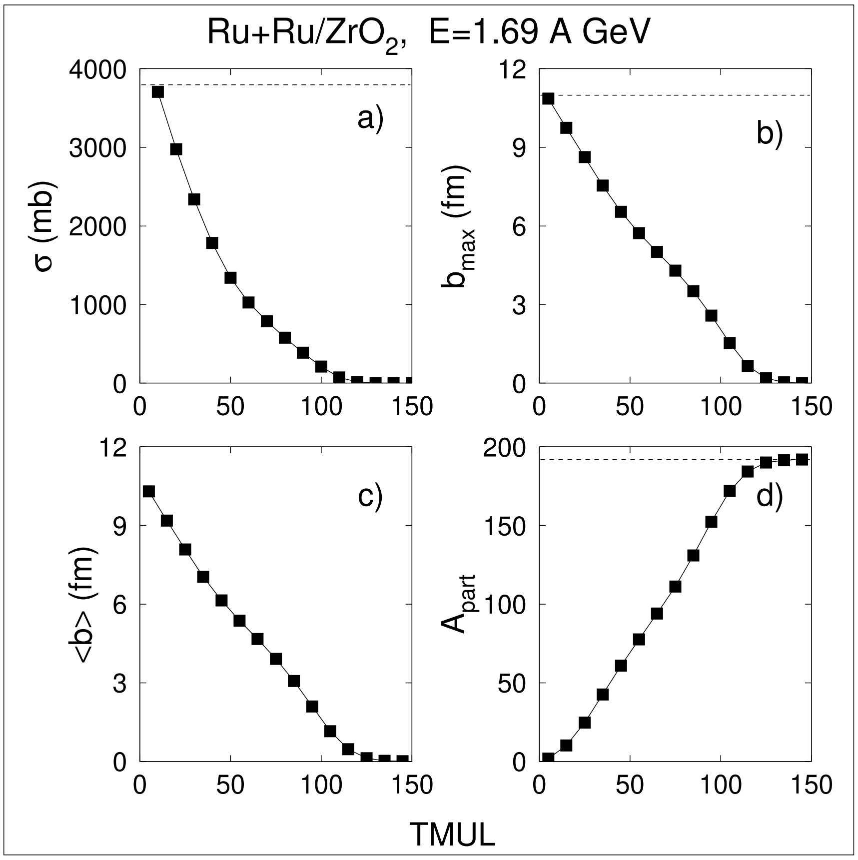

Figure 3.5: *(a) The correspondence between the cross section, $\Delta\sigma$, and the limiting TMUL; (b) the dependence of b_{geo}^{max} on TMUL; (c) $<b>_{geo}$ as a function of TMUL; (d) $<A_{part}>$ as a function of TMUL. The values are calculated for 10-unit-wide bins of the TMUL distribution. The dashed lines represent (a) the total geometrical reaction cross section, σ_{geo}=3800 mb, (b) the maximum impact parameter from the geometrical sharp-cut-off model, $b_{geo}^{max}\simeq$11 fm, and (d) the maximum number of participants, $<A_{part}>$=192.*

3.3 Reconstruction of the reaction plane

The reaction plane is defined as the one that contains the projectile trajectory and the vector of impact parameter $\boldsymbol{b}$ (cf. Figure 3.6a). The method of its determination for each individual event was developed in [68]. Since the reaction products are repelled from the central collision zone in the reaction plane (cf. Figure 3.6), a vector calculated by summing the transverse momenta ($\boldsymbol{p}_t$) of the reaction products in the projectile-rapidity region is supposed to be parallel to $\boldsymbol{b}$. Similarly, a vector calculated from the momenta of the reaction products in the target-rapidity region is antiparallel to $\boldsymbol{b}$. Usually the difference of the two is calculated

$$\boldsymbol{Q} = \sum_n \boldsymbol{p}_t^n \cdot w^n \ . \tag{3.7}$$

TMUL		50 – 85	85 – 95	95 – 140	all
# of events (no selection)	^{96}Ru+^{96}Ru	$2.3\cdot10^6$	$1.4\cdot10^6$	$1.0\cdot10^6$	$4.8\cdot10^6$
	^{96}Ru+^{96}ZrO$_2$	$1.9\cdot10^6$	$1.1\cdot10^6$	$0.7\cdot10^6$	$3.7\cdot10^6$
# of events (after selection)	^{96}Ru+^{96}Ru	$1.9\cdot10^6$	$1.4\cdot10^6$	$1.0\cdot10^6$	$4.4\cdot10^6$
	^{96}Ru+^{96}ZrO$_2$	$1.6\cdot10^6$	$1.1\cdot10^6$	$0.7\cdot10^6$	$3.4\cdot10^6$
$\Delta\sigma$		280 mb	180 mb	120 mb	580 mb
$\Delta\sigma/\sigma_{tot}$		5%	7%	3%	15%
b_{geo}^{max}		4.3 fm	3.1 fm	2.0 fm	4.3 fm
$< b >_{geo}$		3.7 fm	2.5 fm	1.3 fm	2.8 fm
$< A_{part} >$		120	140	170	135

Table 3.1: *The parameters characterizing different event categories selected according to collision centrality given by TMUL.*

The sum runs over the reaction products. The weight w^n can be set to +1 for particles of which rapidities are larger than the mid-rapidity and to -1 for particles emitted in the backward hemisphere.

In this work, the information on the $\boldsymbol{p}_t$ of charged particles is delivered by the Plastic Wall and the CDC. However, as commonly accepted [68], some of the reaction products are excluded from the summation 3.7:

- particles which are emitted within a certain region around the mid-rapidity, $|y^{(0)}|<0.3$, because the direction of their emission has little correlation with the reaction plane,
- pions identified in the CDC, because (as it is also the case for other particles produced during the collision) their correlation with the entrance channel, which defines the reaction plane, is not direct.

For each individual event, the azimuth of the vector $\boldsymbol{Q}$, which will be referred to by Φ_{rec}, differs from the azimuth of the true reaction plane, $\Phi_{r.p.}$, by

$$\Delta\Phi = \Phi_{r.p.} - \Phi_{rec}. \tag{3.8}$$

This is shown schematically in Figure 3.6b. It is important to know $\Delta\Phi$, i.e., the accuracy with which the azimuth of the reaction plane is determined. In particular, the value of $<\cos(\Delta\Phi)>$ is used for various corrections [68].

In this work, a method proposed in [69] is followed in order to estimate the value of $<\cos(\Delta\Phi)>$. Events are randomly divided into two subevents. For each of the subevents, the vector $\boldsymbol{Q}$ and the azimuth Φ_{rec} are determined. Figure 3.7a shows the distribution of

$$\Phi^{1-2} = \Phi^1_{rec} - \Phi^2_{rec} \tag{3.9}$$

for the MedB event sample in the Ru+Ru experiment. A typical gaussian shape on a constant offset can be observed. This is due to the fluctuations in the number of

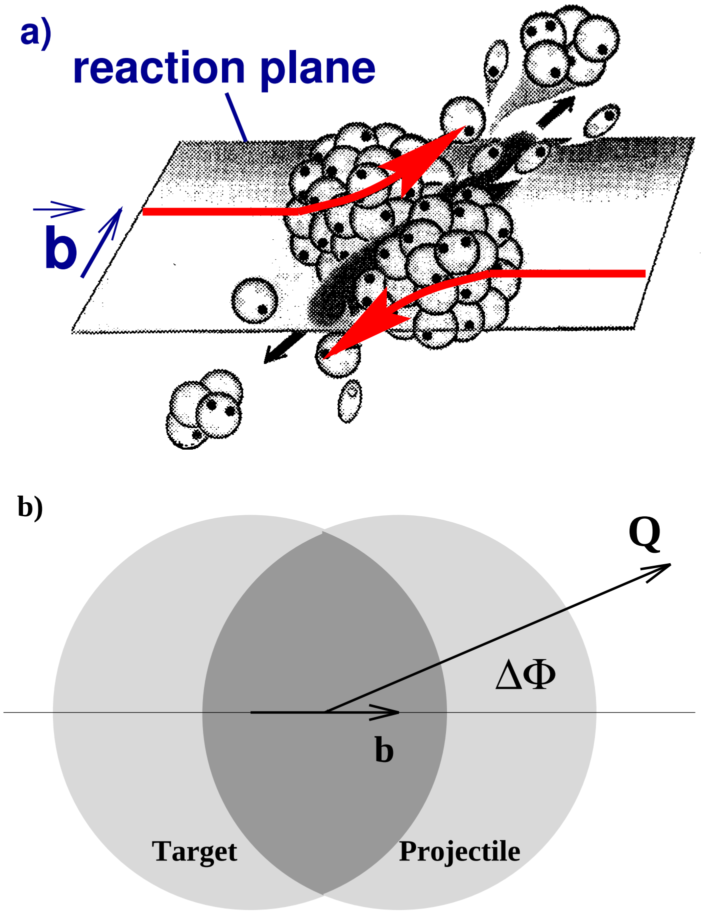

Figure 3.6: *A schematic view of a semi-central collision as seen from a side (a) and in the transverse plane (b). In panel (b), the beam axis is orthogonal to the figure.* $\boldsymbol{b}$ *is the impact parameter vector.* $\boldsymbol{Q}$ *is reconstructed from* $\boldsymbol{p}_t$ *vectors of the reaction products following Eq. 3.7.* $\Delta\Phi$ *is the difference of the azimuthal angles of* $\boldsymbol{b}$ *and* $\boldsymbol{Q}$*. The picture in panel (b) is adapted from [69].*

particles and their $\boldsymbol{p}_t$ vectors, from which Φ^1_{rec} and Φ^2_{rec} are calculated. Figure 3.7b shows the dependence of the dispersion of Φ^{1-2} distribution on collision centrality given by TMUL. For the peripheral collisions (low TMUL), $RMS(\Phi^{1-2})$ decreases with increasing TMUL. This indicates that the determination of $\Phi_{r.p.}$ improves, which is due to the increasing number of particles used for the estimation of vectors $\boldsymbol{Q}_1$ and $\boldsymbol{Q}_2$. On the other hand, for very central reactions (high TMUL), $RMS(\Phi^{1-2})$ increases again because the reaction plane itself is not well defined.

It was proven that, if the fluctuations of the $\boldsymbol{Q}$ vector are gaussian (which is true when the number of particles used to calculate $\boldsymbol{Q}$ is large), the value of $<\cos(\Delta\Phi)>$ depends on $<\cos(\Phi^{1-2})>$ as shown by the line in Figure 3.7c. Therefore, for any considered event sample, the correction factor $<\cos(\Delta\Phi)>$ can be determined if the value of $<\cos(\Phi^{1-2})>$ is known. The values of $<\cos(\Phi^{1-2})>$ and the resulting values

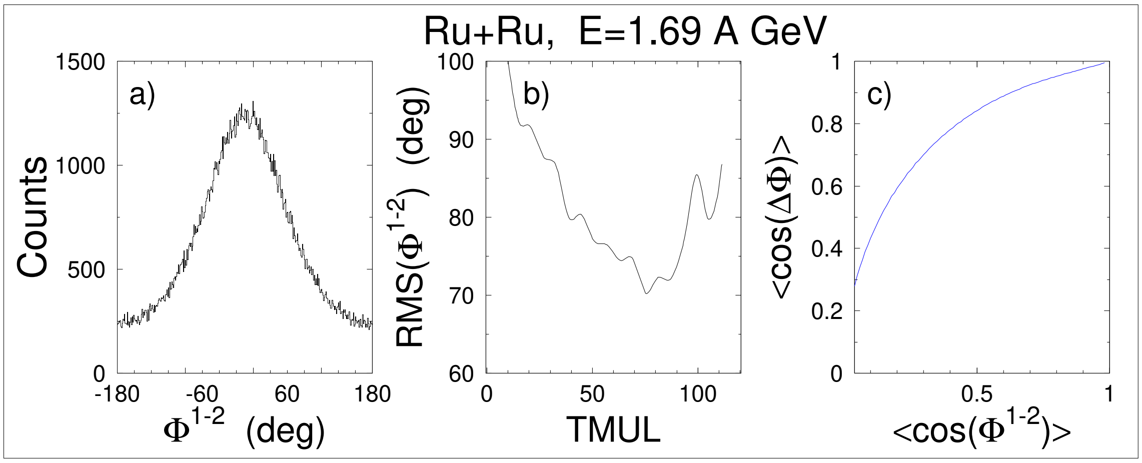

Figure 3.7: *(a) The distribution of* $\Phi^1_{rec} - \Phi^2_{rec}$ *(see text for definition) for the medium-bias event sample in the Ru+Ru experiment. (b) The dependence of the dispersion RMS(*Φ^{1-2}*) on collision centrality given by TMUL. (c) The dependence of the correction factor <cos(*$\Delta\Phi$*)> on <cos(*Φ^{1-2}*)> [69].*

TMUL	50 – 85	85 – 95	95 – 140	all
$<\cos(\Phi^{1-2})>$	0.43	0.38	0.30	0.38
$<\cos(\Delta\Phi)>$	0.80	0.77	0.70	0.77

Table 3.2: *The values of <cos(*Φ^{1-2}*)> and <cos(*$\Delta\Phi$*)> for event categories of different centralities given by TMUL.*

of the correction factors $<\cos(\Delta\Phi)>$ calculated for three event categories considered in this work are listed in Table 3.2.

Chapter 4

Distributions of pions, protons and deuterons

In this chapter, the characteristics of the most abundant products of Ru+Ru collisions at 1.69 A GeV beam kinetic energy, i.e., pions, protons and deuterons will be discussed. The analysis concentrates on the particles that are registered by the CDC. The results will be used as a reference to the measurements on kaons presented in the following part of this work.

4.1 Identification

For positively charged particles, the identification is based on the mass parameters ($Mass_{CDC}$) assigned to particle tracks. In Figure 2.4b the distribution of $Mass_{CDC}$ is shown for particles with momenta lower than 3 GeV/c. The identification conditions are set according to the minima observed in the mass spectrum:

$$\begin{array}{rl} Mass_{CDC} < 0.5\ \mathrm{GeV/c^2}, & \text{for } \pi^+ \text{mesons}, \\ 0.5\ \mathrm{GeV/c^2} < Mass_{CDC} < 1.5\ \mathrm{GeV/c^2}, & \text{for protons}, \\ 1.5\ \mathrm{GeV/c^2} < Mass_{CDC} < 2.3\ \mathrm{GeV/c^2}, & \text{for deuterons}\ . \end{array} \qquad (4.1)$$

With the above conditions particle species can be separated quite reliably. Nevertheless, the yields are not free from background contamination, which is estimated to be less than 10%, even for the highest particle momenta considered.

Since π^- mesons are practically the only negatively charged reaction products, the yield of π^- mesons should be free of any background contamination. All particles of which trajectories are bent in the opposite direction to proton trajectories are considered to be π^- mesons.

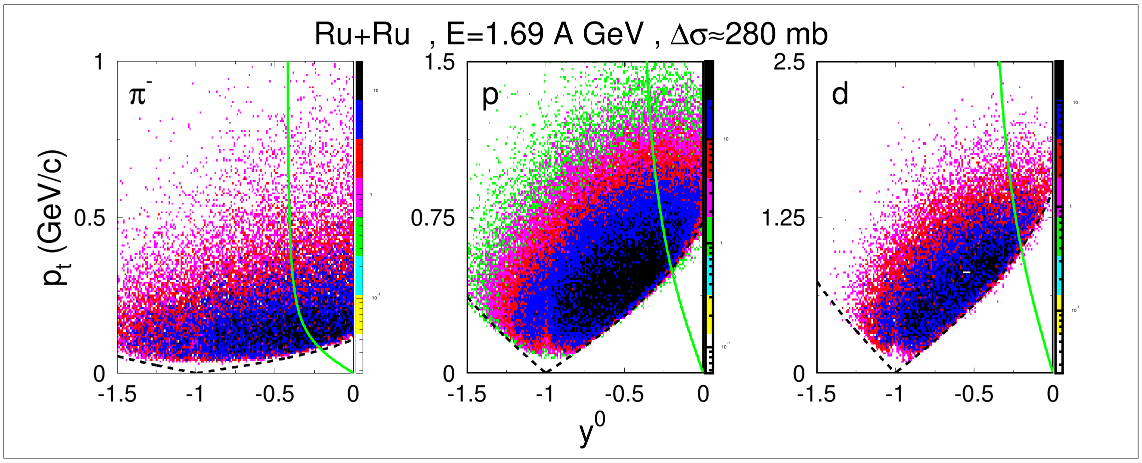

Figure 4.1: *The momentum-space distribution of* π^- *mesons, protons and deuterons in centralmost Ru+Ru collisions. The dashed lines show the geometrical acceptance of the CDC. The solid lines correspond to the emission polar angle* Θ_{cm}=*110°* *at which the kinetic-energy spectra are extracted.*

4.2 Momentum-space distribution

Figure 4.1 shows the momentum-space distributions of π^- mesons, protons and deuterons in the Ru+Ru experiment. The centralmost collisions ($\Delta\sigma \simeq 280$ mb) are selected by the hardware-trigger condition, the other requirements described in Section 3.1, and by the TMUL>95 condition. The representation of transverse momentum versus the normalized rapidity is chosen. The limits of the geometrical acceptance of the CDC are depicted with the dashed lines. The solid lines correspond to the polar angle Θ_{cm}=110°, which will be referred to in the next section.

4.3 Kinetic-energy spectra

Figure 4.2a shows the kinetic-energy spectra of π^- mesons, protons and deuterons measured in the polar-angle range Θ_{cm}=110±2°. The narrow range in the polar angle close to mid-rapidity is chosen in order to minimize the distortion due to the spectator matter, which would be present if spectra of particles emitted in more backward directions were considered[1]. For the same reason the distributions of particles produced in the centralmost collisions are examined. π^- mesons are considered instead of π^+ mesons for their identification is simpler.

The conditions which characterize the system at the moment of freeze-out are often extracted from the final-state momentum-space distributions of particles. If the system is thermally-equlibrated, the energy kinetic released in a collision is distributed between the particles in the form of a thermal motion, characterized

---

[1] For Θ_{cm}<110°, the geometrical acceptance of the CDC is very limited, and does not allow to extract the kinetic-energy spectrum of deuterons (cf. Figure 4.1).

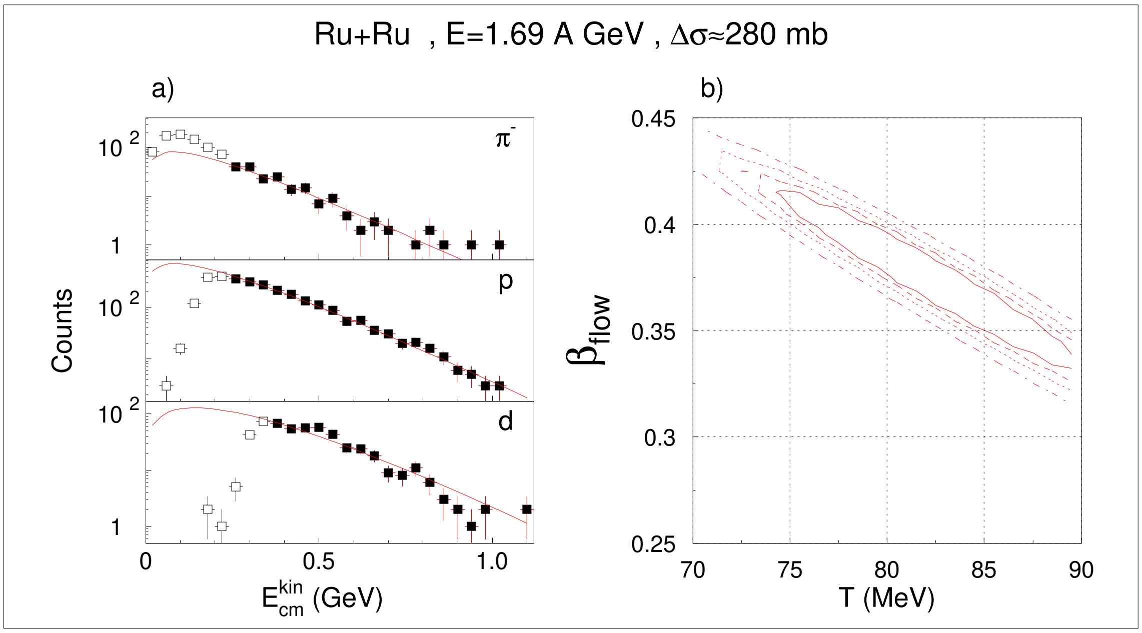

Figure 4.2: *(a) The kinetic-energy spectra of π^- mesons, protons and deuterons in centralmost Ru+Ru collisions. The spectra are extracted in the polar-angle range 110±2°. The lines show a simultaneous fit of formula A.4. (b) The χ^2 values of the fit for different parameters T and β_{flow}. The lines are drawn for the minimum value of χ^2 plus 1, 2, 3 and 5 respectively. The best values of the fit parameters can be estimated: $T \simeq 82$, $\beta_{flow} \simeq 0.37$.*

by a temperature T, and in the form of a radial expansion of the system, with the common velocity β_{flow} [2]. On this assumption, the final-state momentum-space distributions of particles are described by the formulae first proposed in [70]. These formulae are introduced and briefly discussed in appendix A.3.

The lines in Figure 4.2a show the result of the simultaneous fit of the functional form A.4 to the three considered spectra. The spectrum of heavy particles (deuterons) is fitted together with those of lighter protons and pions in order to provide better sensitivity to the parameters, especially the flow velocity. The ranges of E_{cm}^{kin} on which the fit is based are depicted with filled symbols. In the case of proton and deuteron spectra, the points at the lowest E_{cm}^{kin} are excluded from the fit because of the detection inefficiency at the limits of the geometrical acceptance of the CDC (cf. Figure 4.1). In the case of the π^- meson spectrum, the points at low E_{cm}^{kin} are not included in the fit because the spectrum clearly does not follow the formula A.4. The excess of the measured π^- yield over the fit at low E_{cm}^{kin} is usually attributed to pions from the decays of Δ resonances, which occur after freeze-out [72]. Otherwise, the measured spectra agree well with the emission pattern described by formula A.4.

Figure 4.2b shows the χ^2 values of the fit as a function of the parameters T and

---

[2] More sophisticated scenarios, including radial-flow velocity profiles can be investigated as well (see for example [71]), but they are not considered in this work.

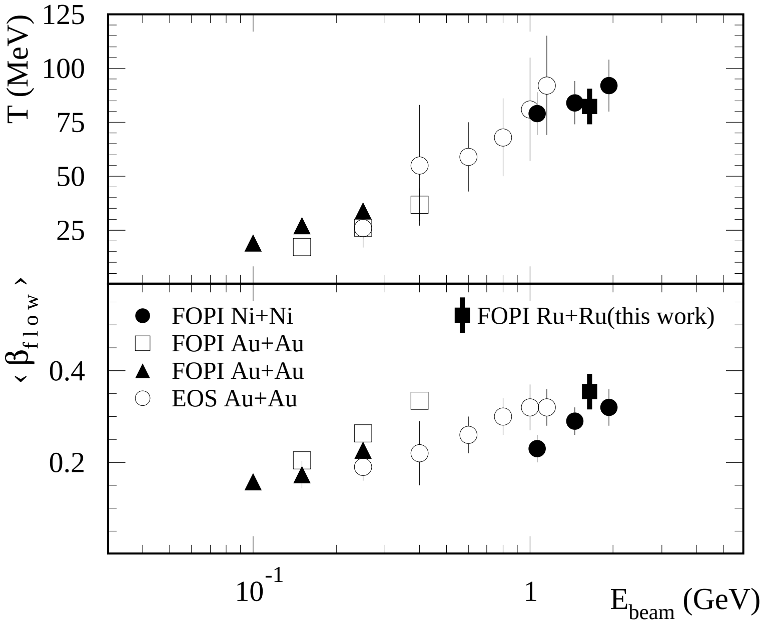

Figure 4.3: *Temperature T and radial flow velocity β_{flow} for three mass-symmetric systems at beam kinetic energies from 0.1 to 2 A GeV. The plot is adapted from [73].*

β_{flow}. Although the two parameters are strongly correlated with each other, the best values T=82±8 MeV and β_{flow}=0.37±0.4 can be estimated.

Figure 4.3 shows the comparison of this result to similar measurements for other systems at intermediate energies.

4.4 Directed side-flow pattern of protons

There are several ways to analyse and describe the coherent movement of particles and its asymmetries. In this work, the so-called directed side-flow pattern is investigated. The mean value of the in-plane component of transverse momenta normalized to particle mass ($<p_x>/m_0c$) is extracted as a function of rapidity (see the explanation below).

Figure 4.4a shows an example of a correlation matrix between particle transverse momenta and rapidities. The transverse momenta were projected onto the reaction plane and divided by particle mass. The reaction plane was reconstructed from $\boldsymbol{p}_t$ vectors of the reaction products, following the method described in Section 3.3. For a better illustration, the distribution of Z=3 particles in central Au+Au collisions at 250 A MeV beam kinetic energy is shown. The plot can be looked at as a "top-view" of the collision with respect to the reconstructed reaction plane. The solid line depicts the values of $<p_x>/m_0c$.

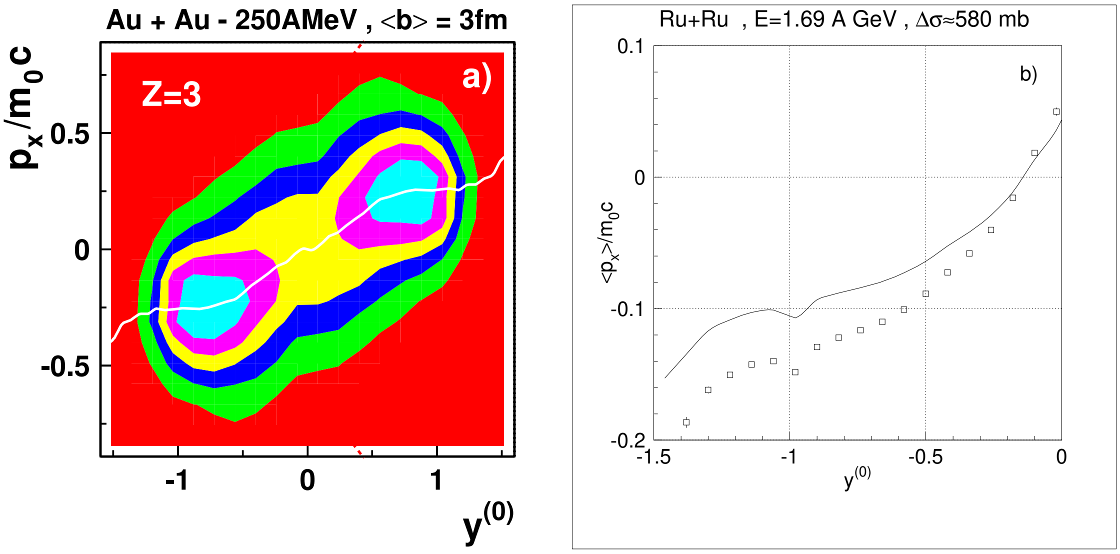

Figure 4.4: *(a) The matrix of correlations between p_x/m_0c and the normalized rapidity for Z=3 particles measured in central Au+Au collisions at 250 A MeV beam kinetic energy. The plot is adapted from [74]. (b) $<p_x>/m_0c$ for protons measured in central Ru+Ru collisions at 1.69 A GeV beam kinetic energy. The solid line shows the results without the correction due to the uncertainty of the reaction-plane reconstruction. The points depict the result with the correction applied.*

The solid line in Figure 4.4b shows the values of $<p_x>/m_0c$ as a function of normalized rapidity for protons in the Ru+Ru experiment. The central collisions were selected by the medium-bias trigger condition and other requirements described in Section 3.1. The reaction plane was reconstructed following the method described in Section 3.3. Two types of modifications have to be applied to the extracted values of $<p_x>/m_0c$.

First of all, in order to determine the azimuth of the reaction plane, Φ_{rec} (cf. Section 3.3), for each proton the vector $\boldsymbol{Q}$ is calculated separately, excluding the particle which is considered. In this way one avoids auto-correlations between the momentum of the considered particle and Φ_{rec} [68]. However, as a consequence, the system that determines the reaction plane is boosted with the transverse velocity [75]

$$\boldsymbol{v}_{boost} = \frac{\boldsymbol{p}_t}{m_{sys} - m} , \tag{4.2}$$

where m and $\boldsymbol{p}_t$ denote the mass and the transverse momentum of particle and m_{sys} is the total mass of the system, i.e., the sum of masses of colliding ions. In order to balance the missing momentum, the boost velocity should be added to particle velocities [75]. That means, the vector

$$\boldsymbol{Q} = \sum_n (\boldsymbol{p}_t^n + m_n \boldsymbol{v}_{boost}) \cdot w^n \tag{4.3}$$

should be calculated in order to determine the azimuth Φ_{rec} instead of that defined by Eq. 3.7. In the case considered here, the resulting correction turned out to be negligible due to the small value of $\boldsymbol{v}_{boost}$.

Secondly, for each event the true azimuth of the reaction plane, $\Phi_{r.p.}$, differs from the estimated one, Φ_{rec}, by a certain angle $\Delta\Phi$. Because of this, the calculated values of p_x do not correspond exactly to the transverse momenta of particles projected onto the reaction plane. However, if $\Delta\Phi$ fluctuates independently from p_x of individual particles, the measured value of $<p_x>_{meas}$ can be corrected in order to account for the uncertainty of the reaction-plane reconstruction according to the formula [68]

$$< p_x >_{corr} = \frac{< p_x >_{meas}}{< \cos(\Delta\phi) >} \ . \tag{4.4}$$

In the case considered here, the correction factor, $<\cos(\Delta\Phi)>$, equals 0.77 (cf. Table 3.1). The corrected values of $<p_x>/m_0c$ are depicted by the points in Figure 4.4b.

One can notice that at mid-rapidity the flow of protons does not vanish, as required by the symmetry of the reaction. It is the combined effect of the detector geometry and the loss of particle trajectories which can not be reconstructed in the azimuthal regions of high track density. The magnitude of the effect was estimated with the GEANT package simulating the full detector response. The corrections that were established [76] turned out to be negligible at around the target-rapidity, where the proton flow is used as a reference for the K^+ meson flow signal (cf. Chapter 7). Therefore, here, these corrections are not applied.

The so-called flow angle can be extracted from Figure 4.4b as the slope of the shown dependence at mid-rapidity. The dependence of $<p_x>/m_0c$ on transverse momentum can be studied as well. Such a detailed analysis is, however, not a part of this work.

Chapter 5

Identification of K^+ mesons

As described in Section 2.2, particle mass determination is possible with the information delivered by the CDC. However, two drawbacks of this method are noticeable.
(i) First of all, from the information delivered by the CDC, the ratio p/Q is derived. In such a case, determination of particle charge is difficult and ambiguous (cf. note in Appendix A.1). Only the sign of the charge can be easily deduced from the curvature of the particle trajectory.
(ii) Secondly, above a certain momentum, at which particles become minimum ionizing, the energy loss exhibits the relativistic rise. Therefore, the Bethe–Bloch lines cross each other, and the branches corresponding to different particle species merge (cf. Figure 2.4). Also, due to the decreasing accuracy of dE/dx measurements, the peaks in the mass distribution get broader, and the separation between different particle species becomes less reliable at high momenta. For example, pions and protons can not be distinguished for p>0.8 GeV/c. Distinction between protons and deuterons is questionable for p>1.8 GeV/c.

Figure 5.1 shows a limited range around the kaon mass, m_K=0.494 GeV/c^2, of $Mass_{CDC}$ distributions for positively charged particles in the Ru+Ru experiment. Each panel of the figure presents the distribution obtained for particles of which momenta are in a narrow range around the value indicated in the captions. The peaks visible at around $Mass_{CDC}$=0.494 GeV/c^2 are attributed to K^+ mesons. They can be distinguished up to momentum of about 0.25 GeV/c. Above this limit, due to the merging of π^+ and K^+ meson peaks, the background contamination in the K^+ meson yield, coming from the tail of the π^+ meson peak, becomes higher than 50%. With information delivered by the CDC only, it is definitely not possible to identify K^+ mesons of which momenta are about 0.3 GeV/c and higher.

In order to overcome this limitation, the information about particle velocities, deduced from the TOF measured by the Barrel, is added to the information about dE/dx and p delivered by the CDC.

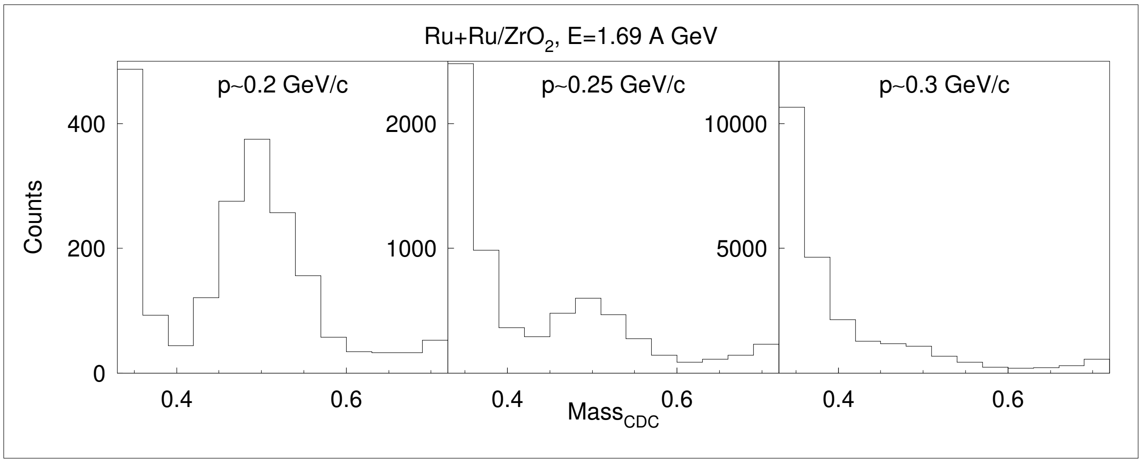

Figure 5.1: *A limited range around the kaon mass,* m_K*=0.494GeV/c*^{2}*, of the* $Mass_{CDC}$ *distributions for particles of different momenta.*

5.1 CDC-Barrel matching

The trajectories of particles identified in the CDC are extrapolated to points where they cross the radius of the Barrel (cf. the lines in Figure 2.2). Only tracks of which the curvature radii (ρ) are greater than the half of the Barrel radius (56 cm) can be considered. This corresponds to the following condition on particle transverse momenta

$$p_t = B\rho\tilde{Q} > 0.1 \text{ GeV/c} \cdot Q \ , \tag{5.1}$$

where $\tilde{Q}$ is the particle charge in Coulomb, Q=1,2 etc. is the particle charge in units of the elementary charge, and B is magnetic induction of 0.6 T.

The tracks from the CDC and the hits in the Barrel are matched. The quality of matching is determined by the quantity

$$\chi^2 = \left(\frac{\Delta Z}{\sigma_z}\right)^2 + \left(\frac{\Delta\phi}{\sigma_\phi}\right)^2 \ . \tag{5.2}$$

It measures the spatial distance between the point at which a track extrapolated from the CDC crosses the Barrel radius and the hit position at which a particle is registered in the Barrel. ΔZ and $\Delta\phi$ denote the distance along the z axis and in the azimuthal angle respectively. σ_z is taken to be 8 cm, and σ_ϕ is set to 2°. These values correspond to the accuracy with which the Z and ϕ coordinates of the hits are measured by the Barrel. Therefore, they provide proper weights with which ΔZ and $\Delta\phi$ can be combined.

The χ^2 quantity, the number of hits which contribute to a track (NH), and the distance of the track to the event vertex ($Z0, D0$ – see the Section 5.3 for the explanation) provide the means for selecting well identified particles. The relevance of these parameters will be discussed further in Section 5.3

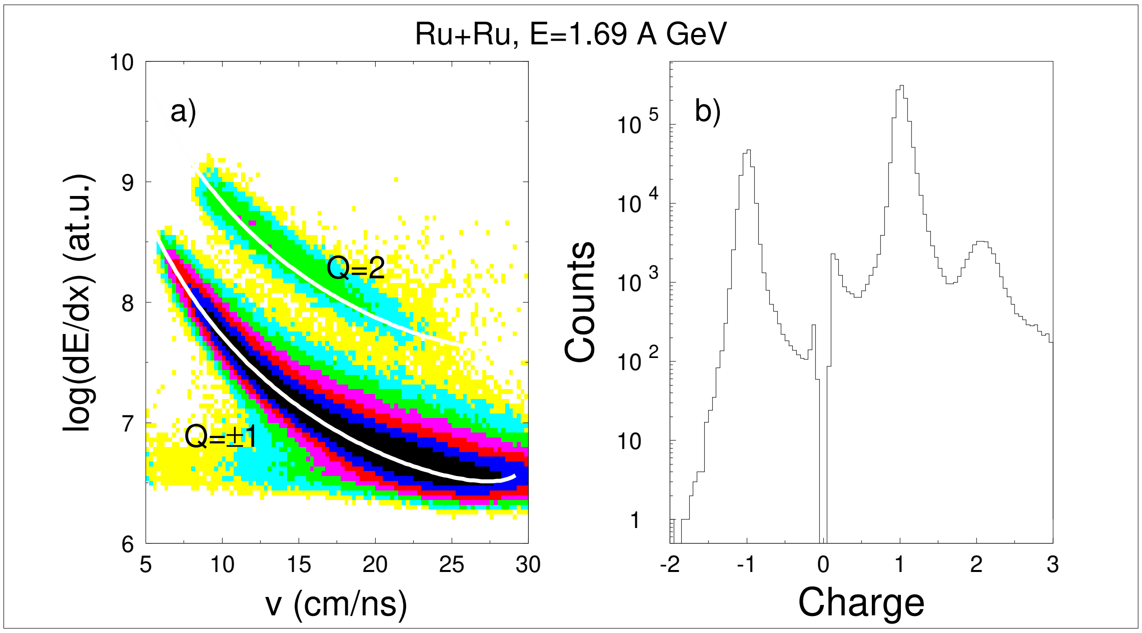

Figure 5.2: *Charge determination with CDC–Barrel combined measurements. (a) The correlation matrix between energy losses, dE/dx, and velocities, v, of particles. (b) The charge spectrum obtained by projecting the matrix from panel (a) onto the charge parameter in the Bethe–Bloch formula.*

5.2 Charge and mass determination

By combining the information on v and dE/dx, the charge of the particle can be deduced in the same way as in the case of Phase 1 detectors. Figure 5.2a shows the correlation matrix between dE/dx and v of particles. A clear separation between particles of which charges are ± 1 and $+2$ is demonstrated. The lines are drawn according to the Bethe–Bloch formula (Eq. A.1). Figure 5.2b shows the charge spectrum obtained by projecting the matrix from panel (a) onto the charge parameter in the Bethe–Bloch formula. The sign of the charge is deduced from the sign of the track curvature.

Moreover, with the information delivered by the Barrel, the redundancy is achieved in determining particle mass. As discussed in Section 5.5, this allows to extend the momentum range in which K^+ mesons can be identified. Figure 5.3a shows the correlation matrix between p/Q and v of particles detected by the CDC and Barrel. Lines corresponding to different masses are drawn according to the formula $p/Q{=}(m/Q){\cdot}\gamma v$. The structure which is visible in between the proton and deuteron branches is attributed to ^{3}He fragments of $Q{=}{+}2$. A quantity called $Mass_{Barrel}$ is obtained by projecting the matrix onto the mass parameter in the above formula. Figure 5.3b shows the corresponding mass distribution. The mass parameters are multiplied by -1 for negatively charged particles.

Figure 5.4a shows the two-dimensional identification matrix of $Mass_{CDC}$ versus

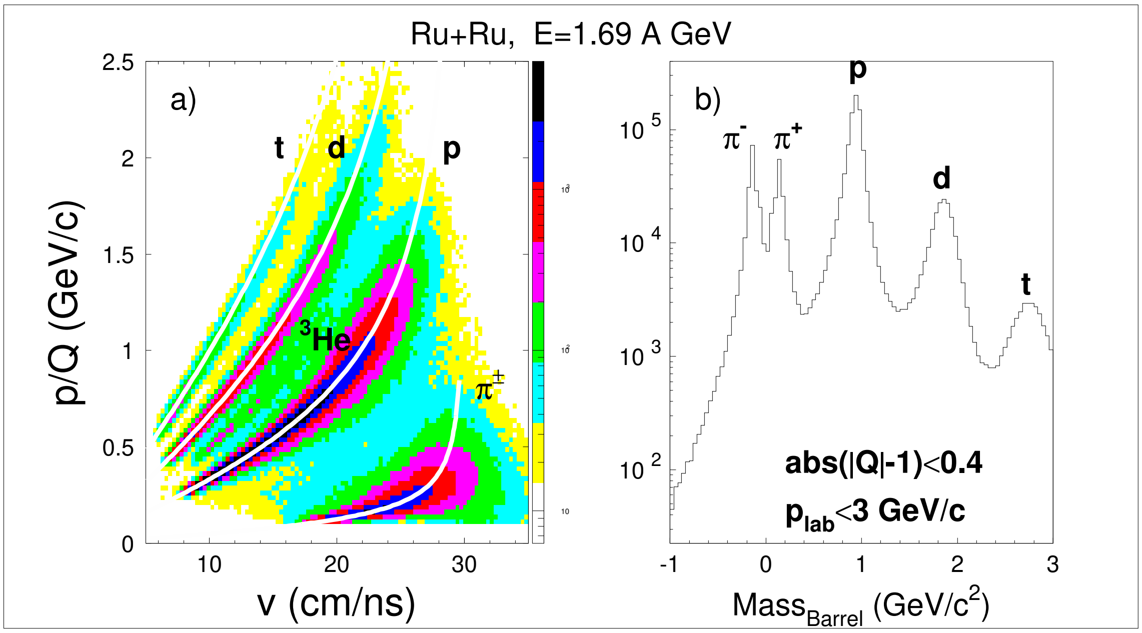

Figure 5.3: *Particle identification with* TOF *measurements by the Barrel. (a) The correlation matrix between ratios* p/Q *and velocities,* v*, of particles. (b) The mass spectrum obtained by projecting the matrix from panel (a) onto the mass parameter in the formula* $p/Q{=}(m/Q)\cdot\gamma v$*. Only tracks of which the charge parameters fulfill the condition abs(*$|Q|$*-1)<0.4 are included.*

$Mass_{Barrel}$. Only tracks of which the charge parameters fulfill the condition abs($|Q|$-1)<0.4 are included. Separation between different particle species is demonstrated. In general, particles are identified by imposing appropriate conditions on charge and mass parameters.

5.3 Identification criteria

Figure 5.4b shows a limited range around the kaon mass, $\mathrm{m_K}$=0.494 GeV/c^2, of the two-dimensional identification matrix of $Mass_{CDC}$ versus $Mass_{Barrel}$. Only positively charged particles (abs(Q-1)<0.4) with momenta lower than 0.45 GeV/c are included. A clear peak from K$^+$ mesons can be noticed. As indicated by the circle, K$^+$ mesons can be selected by imposing the following condition on the mass parameters

$$\left(\frac{Mass_{CDC}-0.494\ \mathrm{GeV/c^2}}{0.1\ \mathrm{GeV/c^2}}\right)^2+\left(\frac{Mass_{Barrel}-0.494\ \mathrm{GeV/c^2}}{0.1\ \mathrm{GeV/c^2}}\right)^2<1\ . \qquad (5.3)$$

The radius of the circle, 0.1 GeV/c^2, is chosen rather arbitrarily. On the one hand, one tends to choose large radii in order not to eliminate the tails of the K$^+$ meson peak. On the other hand, one needs to keep the radii reduced in order to avoid the

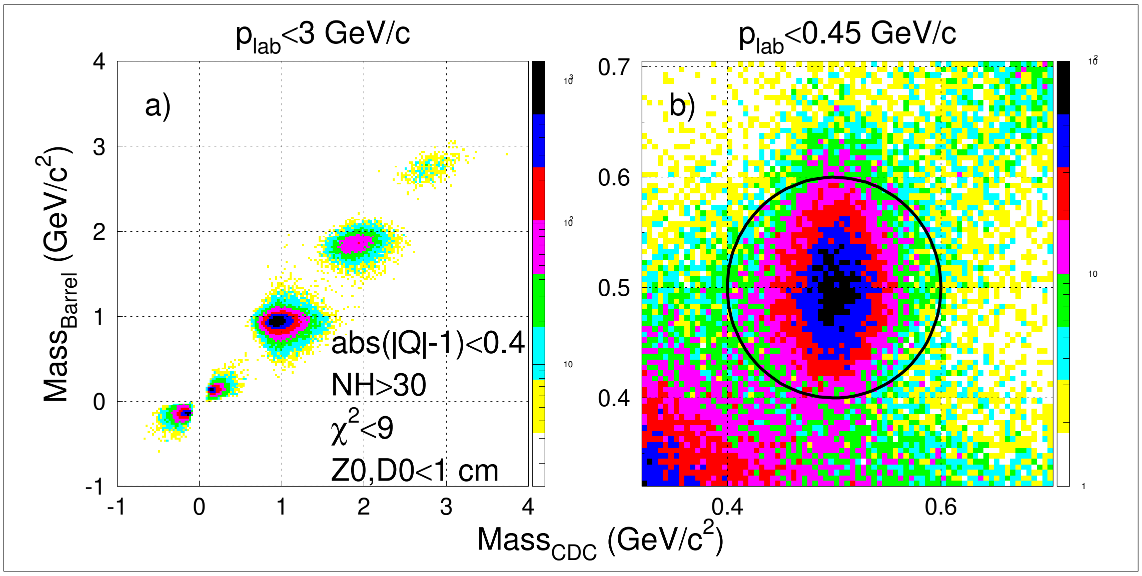

Figure 5.4: *Particle identification with CDC-Barrel combined measurements. (a) An identification scatter-plot* $Mass_{Barrel}$ *versus* $Mass_{CDC}$ *for particles with momenta lower than 3 GeV/c. (b) A limited range around the kaon mass,* m_K*=0.494GeV/*c^2*, of the mass distribution from panel (a). Only particles of momenta lower than 0.45 GeV/c are included.*

background contamination from the tails of the π^+ meson and proton peaks. This is important especially at higher momenta where the accuracy of the measurements gets worse and the peaks in the mass distribution are broader.

In order to minimize the background contamination in the extracted K$^+$ meson yield, only well identified particles are selected. Several parameters show how good the identification of a particle is and how well its four-momentum is deduced. In this work, three quantities are examined in order to judge the quality of the particle identification.

(i) NH – number of hits. The more hits a track consist of, the more accurately the parameters of this track can be evaluated, and the more precisely particle momentum can be estimated. Figure 5.5a shows the distribution of NH for particle trajectories reconstructed in the CDC. Due to the change of the operation modes of the tracking algorithm between finding short and long tracks, there is a discontinuity in the distribution at NH=30.

(ii) χ^2 – defined by Eq. 5.2. It reflects the quality of matching between tracks from the CDC and hits in the Barrel. The smaller the χ^2 value is, the higher the probability is that a track is properly matched to a hit in the Barrel, and that the mass of a particle is well estimated. Figure 5.5b shows the distribution of Δz and $\Delta\phi$ values which are referred to in Eq. 5.2. The corresponding distribution of χ^2 values is shown in Figure 5.5c.

(iii) $D0$ and $Z0$ – the distance of the track to the event vertex in the xy plane and in the z direction respectively. Due to the limited accuracy with which the position

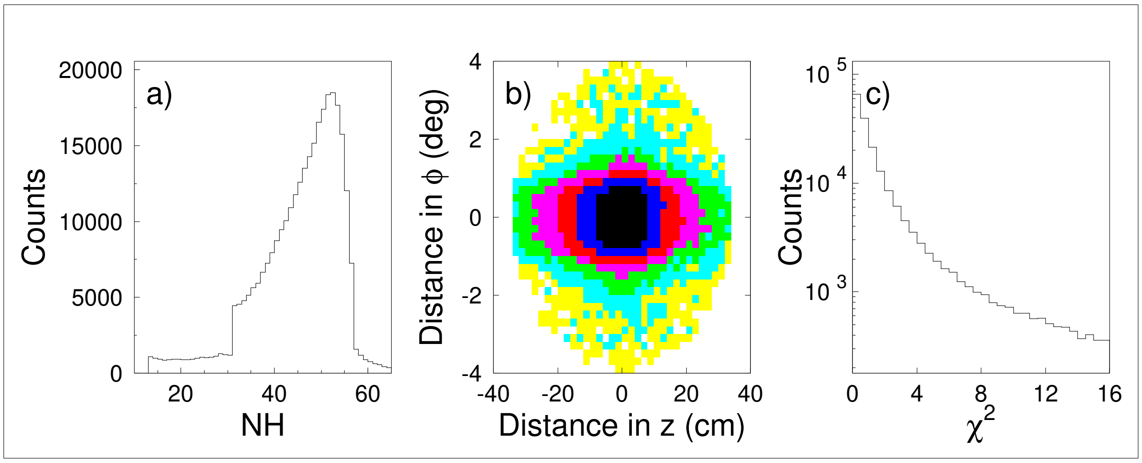

Figure 5.5: *(a) The distribution of number of hits which contribute to particle trajectory reconstructed in the CDC. (b) Spatial distance between the CDC tracks and the hits in the Barrel. (c) The distribution of* χ^2 *parameter defined by Eq. 5.2 resulting from (b).*

of hits in the CDC is deduced, helix curves which are fitted to particle trajectories do not point exactly to the reconstructed event vertex. The smaller the distance of particle track to the event vertex is, the higher the probability is that the curvature radius of the track, and hence the momentum of the particle is well determined.

In this work, only tracks of which parameters fulfill the conditions

$$NH > 30, \ \chi^2 < 9, \ Z0 < 1 \text{ cm}, \ D0 < 1 \text{ cm} \tag{5.4}$$

are attributed to well identified particles of which four-momenta are derived precisely.

In order to determine the upper momentum limit for the K^+ meson identification, two-dimensional mass spectra, such as shown in Figure 5.6, are examined. Each panel of the figure presents the distribution obtained for particles with momenta in a narrow range around the values indicated in the captions. Due to the decreasing accuracy of measurements, the higher the particle momenta are, the more the K^+ meson yields get contaminated, mainly by the tails of π^+ meson peaks. It can be seen that at higher momenta, above 0.4 GeV/c, the K^+ meson yield can be evaluated only after subtracting a substantial contribution from the background. The method of determining these corrections will be described in greater detail in Section 5.5. It will be shown that the background content in the K^+ meson yield does not exceed 30% if particles with momenta lower than 0.45 GeV/c are considered.

Table 5.1 summarizes the statistics of K^+ mesons identified in the Ru+Ru and Ru+ZrO_2 experiments. K^+ mesons are selected by the requirement 5.3, accompanied by the condition 5.4. Only particles with momenta lower than 0.45 GeV/c^2 are included. The quoted yields are not corrected in order to account for the efficiency of the particle identification procedure and for the background contamination. The

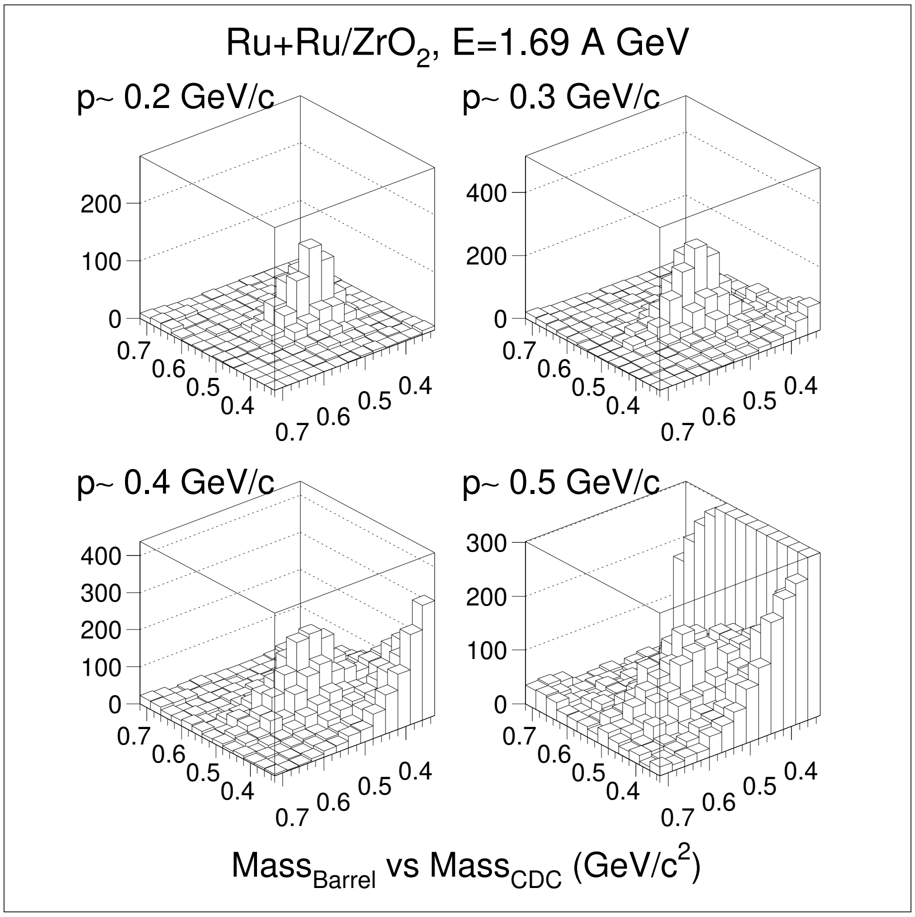

Figure 5.6: *A limited range around the kaon mass, m_K=0.494 GeV/c^2, of the mass distributions $Mass_{CDC}$ versus $Mass_{Barrel}$ for particles of different momenta. K^+ mesons can be selected quite reliably up to momenta of about 0.45 GeV/c.*

methods of determining these corrections will be described in detail in Sections 5.4 and 5.5.

Similar detection rates in both experiments can be concluded. This suggests that the difference between the targets has little influence on the production of K^+ mesons.

5.4 Efficiency of the K^+ meson identification procedure

About 95% of the hits registered in the CDC are assigned to tracks that are reconstructed. Therefore, it is assumed that the detection efficiency of charged particles in the CDC is nearly 100%. In order to determine the efficiency of the particle identification procedure for the CDC-Barrel combined measurements, the number of identified particles should be compared to the number of particles detected by

System	# of K^+ mesons (detected)	# of K^+ mesons per event
^{96}Ru+^{96}Ru	$13.1 \cdot 10^3$	$2.99 \pm 0.03(\mathrm{stat}) \cdot 10^{-3}$
^{96}Ru+^{96}ZrO$_2$	$10.2 \cdot 10^3$	$3.00 \pm 0.03(\mathrm{stat}) \cdot 10^{-3}$

Table 5.1: *Statistics of K^+ mesons in the Ru+Ru and Ru+ZrO$_2$ experiments.*

the CDC alone. Unfortunately, the identification of K^+ mesons with CDC alone is possible only for particles with momenta lower than 0.25 GeV/c. Therefore, this direct way can not be followed in order to determine the efficiency of the K^+ meson identification procedure, which will be referred to by *Eff*(K^+). For determining *Eff*(K^+) a more complicated and indirect method was invented.

In the first step, the efficiency of the identification procedure for other particle species, i.e., pions, protons and deuterons was determined. In both cases (CDC alone and CDC-Barrel combined measurement) particles were selected with the conditions 4.2. Figure 5.7 shows the resulting efficiency of the identification procedure as a function of momentum.

Several observations can be made. (i) Above a certain value, the efficiency does not depend on particle momenta. (ii) The efficiency is the same for negatively and positively charged pions. (iii) The efficiency is similar for all considered particle species. However, the higher the particle mass is, the higher the threshold momentum is at which the efficiency drops[1].

An indirect estimate of the efficiency of the K^+ meson identification procedure is based on that of protons. Both are proven to be similar, at least at momenta higher than the characteristic threshold. In the second step, protons identified with CDC-Barrel combined measurements are selected with the condition

$$\left(\frac{Mass_{CDC} - 0.938\ \mathrm{GeV/c^2}}{0.1\ \mathrm{GeV/c^2}}\right)^2 + \left(\frac{Mass_{Barrel} - 0.938\ \mathrm{GeV/c^2}}{0.1\ \mathrm{GeV/c^2}}\right)^2 < 1\ . \quad (5.5)$$

It is analogous to condition 5.3, with which K^+ mesons are identified. Only protons of which track parameters satisfy in addition the other requirements of the K^+ mesons identification procedure (condition 5.4) are considered. The number of protons selected with these requirements is divided by the number of protons detected by the CDC alone, i.e., the number of tracks of which parameters fulfill the condition

$$0.5\ \mathrm{GeV/c^2} < Mass_{CDC} < 1.5\ \mathrm{GeV/c^2}\ . \quad (5.6)$$

In Chapter 6, the final-state momentum-space distribution of K^+ mesons will be investigated in detail, and the K^+ meson yields will be extracted, on the one hand,

---

[1] The identification inefficiency occurs because low-momenta particles loose a lot of their energy on the way to the Barrel. They can not be well identified either because they never reach the Barrel or because their momenta get too much distorted.

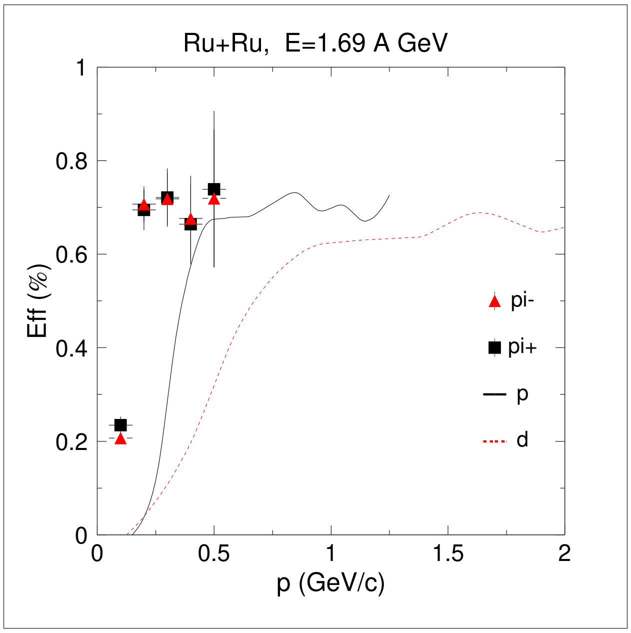

Figure 5.7: *Efficiency of the particle identification procedure for CDC-Barrel combined measurements as a function of momentum. The efficiency is determined for pions, protons and deuterons.*

as a function of normalized rapidity ($y^{(0)}$) and transverse mass $(m_t)^2$, and, on the other hand, as a function of kinetic energy (E^{kin}_{cm}) at different polar angles (Θ_{cm}) in the CM reference frame. Therefore, in Figures 5.8 and 5.9, *Eff*(K$^+$) is shown as a function of these variables. It was estimated following the procedure sketched above separately in each bin of m_t and $y^{(0)}$, as well as E^{kin}_{cm} and Θ_{cm}.

The upper-left panel of Figure 5.8 shows the dependence of the efficiency on m_t and $y^{(0)}$. In other panels of the figure, *Eff*(K$^+$) is plotted as a function of transverse mass for different slices of normalized rapidity. Similarly, in the upper-left panel of Figure 5.9, the efficiency is plotted as a function of E^{kin}_{cm} and Θ_{cm}. In subsequent panels of the figure, the dependence of *Eff*(K$^+$) on kinetic energy is shown at different polar angles.

Eff(K$^+$) decreases rapidly at low m_t or E^{kin}_{cm}, (cf. Figures 5.8 and 5.9). This is due to the detection inefficiency of protons with momenta lower than 0.4 GeV/c (cf. Figure 5.7). A similar drop should occur for still lower momentum in the case of K$^+$ mesons ($p \simeq 0.15$ GeV/c), of which the specific energy loss is smaller. Thus, it is assumed that *Eff*(K$^+$) depends linearly on m_t and on E^{kin}_{cm} even at low m_t or E^{kin}_{cm}, as indicated by the straight-line fits in Figures 5.8 and 5.9.

Eff(K$^+$) is not constant as a function of momentum or other kinematical variables, like m_t and E^{kin}_{cm}. This is because condition 5.5 selects tracks of which the mass parameters are around the nominal mass of a particle. However, the higher the momentum is, the less accurate the measurements become, and the broader the peaks in the mass distributions are. Therefore, at higher momenta, the selection with condition 5.5 becomes less efficient.

---

[2] See Appendix A.2 for the definition of m_t.

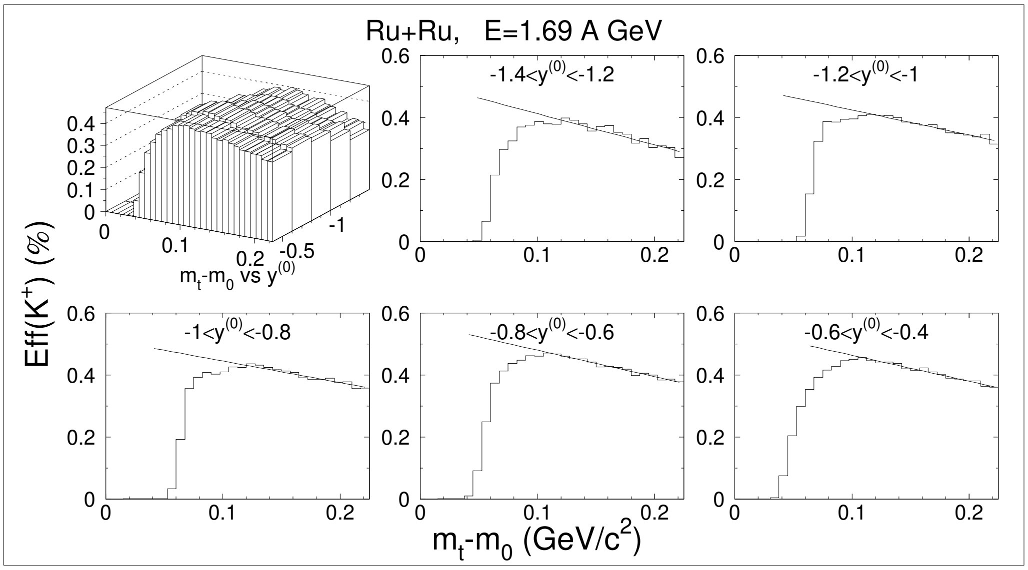

Figure 5.8: *The efficiency of the K^+ meson identification procedure for the CDC-Barrel combined measurements. In the upper-left panel, the efficiency is plotted as a function of transverse mass (m_t) and normalized rapidity ($y^{(0)}$). Other panels show the dependence of efficiency on m_t for different slices of $y^{(0)}$. The straight-line fits indicate how the efficiency is extrapolated to low-m_t regions.*

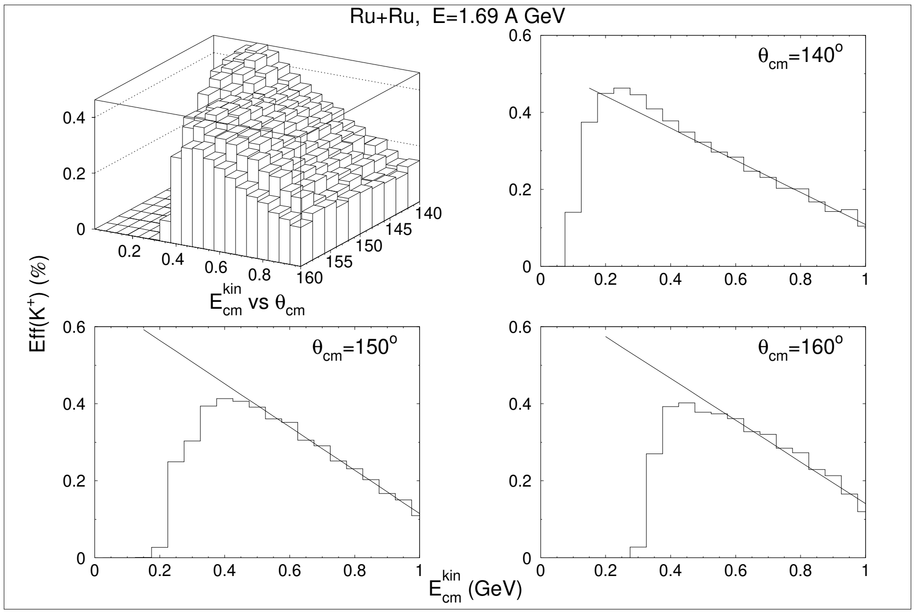

Figure 5.9: *The efficiency of the K^+ meson identification procedure for the CDC-Barrel combined measurements. In the upper-left panel, the efficiency is plotted as a function of the kinetic energy (E_{cm}^{kin}) and the polar angle (Θ_{cm}) in the CM reference frame. Other panels show the dependence of the efficiency on E_{cm}^{kin} at different polar angles. The straight-line fits indicate how the efficiency is extrapolated to low-E_{cm}^{kin} regions.*

5.5 Background content in the K$^+$ meson yields

As a consequence of the broadening of the peaks in the mass distribution, the separation between particles species becomes questionable at high momenta. Using the $Mass_{CDC}$ quantity, K$^+$ mesons can be reliably selected up to a momentum of 0.25 GeV/c. Above this limit, the background contamination in the K$^+$ meson yield, coming from the tail of π^+ meson peak, becomes higher than 50% and is difficult to handle as can be noticed in Figure 5.1.

The value of the limiting momentum can be shifted up to $p \simeq 0.45$ GeV/c if particle identification is based on two-dimensional mass distributions, such as shown in Figure 5.6. However, also in this case, at momenta higher than 0.3 GeV/c, the K$^+$ meson yield does not remain free of background contamination.

Panels (a) to (d) of Figure 5.10 show again a limited range around the kaon mass, m$_K$=0.494 GeV/c^2, of the mass distributions obtained for particles of different momenta which are indicated in the figure captions. This time, particle yields are plotted as a function of the quantity

$$(Mass_{CDC} + Mass_{Barrel})/2 \; . \tag{5.7}$$

The distributions were obtained by projecting the corresponding two-dimensional identification matrixes, $Mass_{CDC}$ versus $Mass_{Barrel}$, onto the diagonal line. Only particles within a narrow slice around the diagonal line

$$|Mass_{CDC} - Mass_{barrel}| < 0.05 \text{ GeV/c}^2 \tag{5.8}$$

were included.

The tail of the π^+ meson peak can be seen in all four panels in the upper row of figure 5.10. The higher the momentum is, the more the tail of the π^+ meson peak contaminates the K$^+$ meson yield. The contamination becomes substantial for momenta higher than 0.4 GeV/c^2.

In order to investigate the amount of contamination, the tails of the π^+ meson peaks in the considered mass distributions are fitted by a single exponential form

$$\exp\left(a - x * b\right) \; , \tag{5.9}$$

where a and b are fitted parameters, and x is the quantity defined by the formula 5.7. The fits are depicted by the lines in panels (a) to (d) of Figure 5.10. The background contamination of the K$^+$ meson yield, *Back*(K$^+$), is estimated by dividing the integral of the mass distribution from x=(0.494-0.1) GeV/c^2 to x=(0.494+0.1) GeV/c^2 by the integral of the fitted formula over the same range. Figure 5.10e shows the resulting background content in the K$^+$ meson yield as a function of momentum. As indicated by the line in the figure, the observed dependence can be well described by the polynomial form

$$Back(K^+) = a \cdot (p - 0.25)^2 \; , \tag{5.10}$$

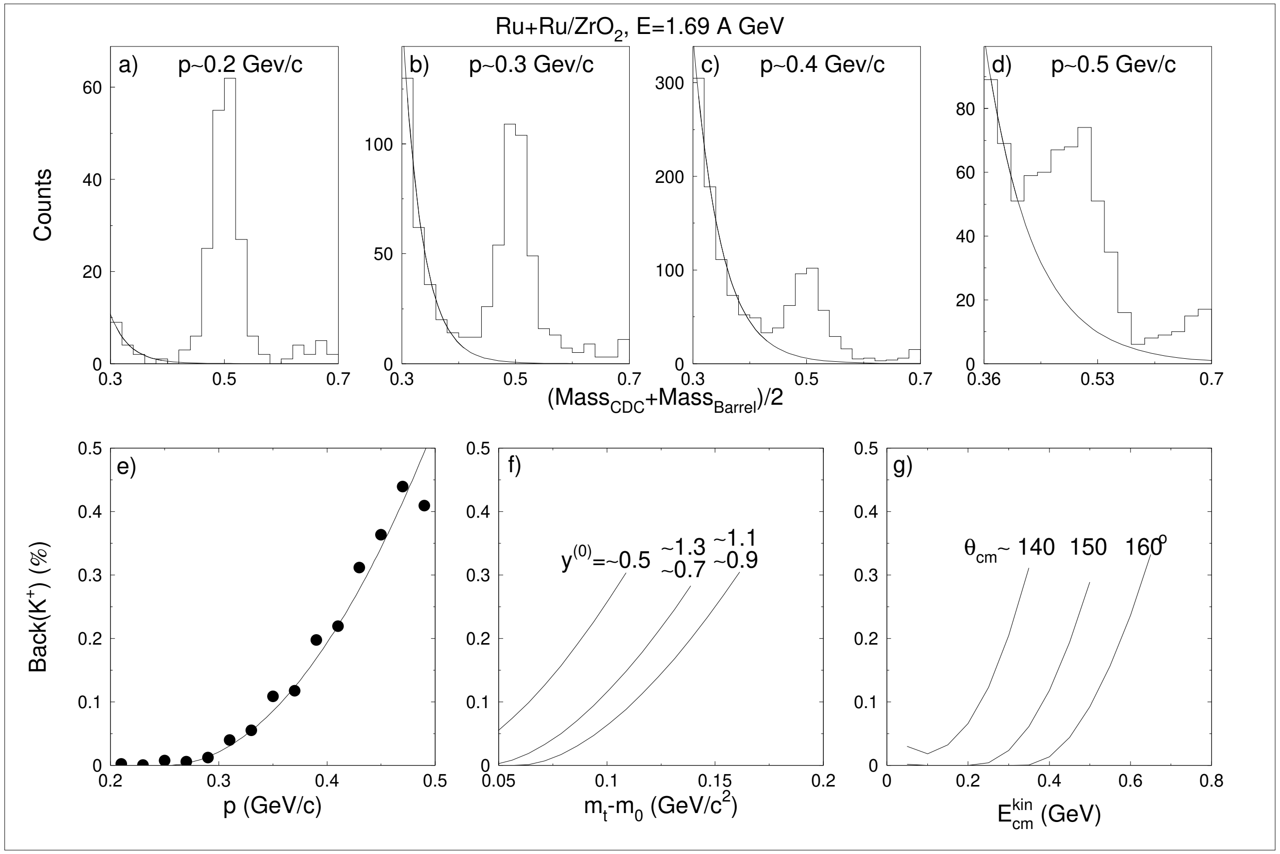

Figure 5.10: *(a) to (d) A limited range around the kaon mass, m_K=0.494 GeV/c^2, of the mass distributions for particles of different momenta. Particle yields are plotted as a function of the quantity defined by the formula 5.7. (e) The background content in the measured K^+ meson yield as a function of momentum. (f) The background content as a function of transverse mass for different rapidity slices. The dependencies are derived from parametrization 5.10 using the functional relationship p=$p(m_t, y^{(0)})$. (g) Same as (f) but the background content is plotted as a function of kinetic energy E_{cm}^{kin} at different polar angles Θ_{cm}. The dependencies are derived from parametrization 5.10 using the functional relationship p=$p(E_{cm}^{kin}, \Theta_{cm})$.*

a being the fitted parameter.

Due to the low statistics of the measured K^+ mesons, the mass distributions such as shown in Figure 5.10 can not be fitted in different bins of $y^{(0)}$ and m_t, or E^{kin}_{cm} and Θ_{cm} separately. However, *Back*(K^+) can be recalculated for each of these bins from parametrization 5.10 by using the functional relations

$$p = p(m_t, y^{(0)}) \tag{5.11}$$

and

$$p = p(E^{kin}_{cm}, \Theta_{cm}) \ . \tag{5.12}$$

Figure 5.10(f) shows the resulting dependencies of *Back*(K^+) on m_t for different rapidity slices. In Figure 5.10(g) the dependencies of *Back*(K^+) on E^{kin}_{cm} at different polar angles Θ_{cm} are presented.

5.6 Systematic uncertainty of K^+ meson yields

Three contributions to the systematic uncertainty of the measured K^+ meson yields are considered.

The first one is connected to the identification procedure. The accuracy with which the yields can be extracted may be tested by comparing the results obtained when different identification conditions are used. In addition to the requirement 5.4, two other, so to say, extreme cases were considered.
(i) More restrictive identification conditions:

$$NH > 35, \ \chi^2 < 4, \ Z0 < 0.2 \text{ cm}, \ D0 < 0.2 \text{ cm} \ , \tag{5.13}$$

which are supposed to allow for less contamination of "bad" tracks.
(ii) Weaker requirements:

$$NH > 20, \ \chi^2 < 9, \ Z0 < 3 \text{ cm}, \ D0 < 3 \text{ cm} \ , \tag{5.14}$$

which lead to higher contamination of "bad" tracks, but prevent from eliminating less reliably identified particles.

The efficiency of the identification procedure was derived separately for each set of the identification requirements 5.4, 5.13 and 5.14.

In 5.13 the condition on NH is put higher than 30 in order to test a possible systematic bias of the results due to the change of the operation modes of the tracking algorithm, which causes the discontinuity in the distribution shown in Figure 5.5a.

The second source of the systematic error originates from determining the efficiency of detection and identification procedure. The latter is estimated indirectly and based on the extrapolation from high m_t or E^{kin}_{cm} (cf. Section 5.4). It is assumed that the efficiency is known with ±10% accuracy, which takes into account (i) the uncertainty of determining the detection efficiency and (ii) the differences

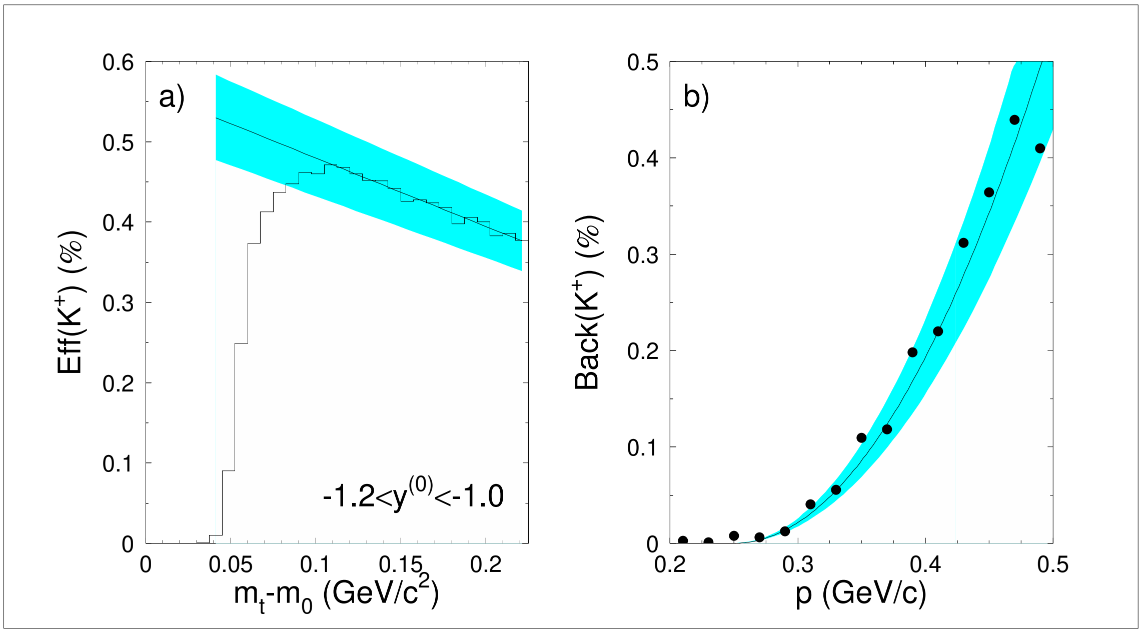

Figure 5.11: *An illustration of two contributions to the systematic uncertainty of the measured* K^+ *meson yields. (a) The efficiency of the* K^+ *meson identification procedure for a given slice of normalized rapidity as a function of* m_t. *As indicated by the grey shaded band, it is supposed to be determined with ±10% accuracy. (b) The background content in the measured* K^+ *meson yields as a function of momentum. As indicated by the grey shaded band, it is supposed to be known with ±20% accuracy.*

between identification efficiencies for different particle species (cf. Figure 5.7). The allowed ±10% variation is indicated by the grey shaded band in Figure 5.11a, which illustrates the dependence of *Eff*(K$^+$) on the transverse mass for the rapidity slice -1.2<$y^{(0)}$<-1.0.

The last considered source of the systematic error is the background content in the K$^+$ meson yields, *Back*(K$^+$). It is assumed that the background contamination from the tails of π^+ meson peaks can be estimated following the method described in Section 5.5 with ±20% accuracy. This is indicated by the grey shaded band in Figure 5.11(b), which shows the dependence of *Back*(K$^+$) on momentum.

Contributions of different origin to the total systematic uncertainty of the measured yields are discussed further in Section 6.2 in the case of the transverse-mass spectra of K$^+$ mesons.

Chapter 6

K^+ meson phase-space distribution

In this chapter, the final-state momentum-space distribution of K^+ mesons measured in the Ru+Ru and Ru+ZrO_2 experiments will be discussed. A reliable identification of K^+ mesons is possible when the information from the CDC and the Barrel is combined[1]. Therefore, the fraction of the momentum space in which K^+ mesons are measured is restricted to the geometrical acceptance of the Barrel. In addition, due to the limited accuracy of the measurements, only kaons with momenta lower than 0.45 GeV/c are identified. Both restrictions imply that the K^+ meson yield at around target rapidity can be directly extracted. In order to estimate the total K^+ meson yield, the measured distributions are extrapolated to the not measured regions of the momentum space.

The central collisions selected by the medium-bias trigger condition and other requirements described in Chapter 3 are considered. The selected event samples, consisting of about 4.38 and 3.39 million events in the Ru+Ru and Ru+ZrO_2 experiments respectively, correspond to the centralmost $\Delta\sigma \simeq 580$ mb of the total geometrical cross section (cf. Table 3.1).

6.1 Acceptance

Figure 6.1 shows the final-state momentum-space distribution of K^+ mesons measured in the Ru+Ru and Ru+ZrO_2 experiments. The representation in the form of the transverse mass (m_t) versus the normalized rapidity ($y^{(0)}$) is chosen. The dashed lines depict the geometrical acceptance of the Barrel and the upper momentum limit p=0.45 GeV/c for the K^+ meson identification.

K^+ mesons were selected with conditions 5.3 and 5.4. Altogether $13.1 \cdot 10^3$ and $10.2 \cdot 10^3$ K^+ mesons with momenta lower than 0.45 GeV/c were identified in the Ru+Ru and Ru+ZrO_2 experiments respectively. This corresponds to average detection rates

---

[1] A substantial effort is being made in order to extract the K^+ and K^- meson yields at mid-rapidity from the information delivered by the Helitron [65]. However, it is not a part of this work

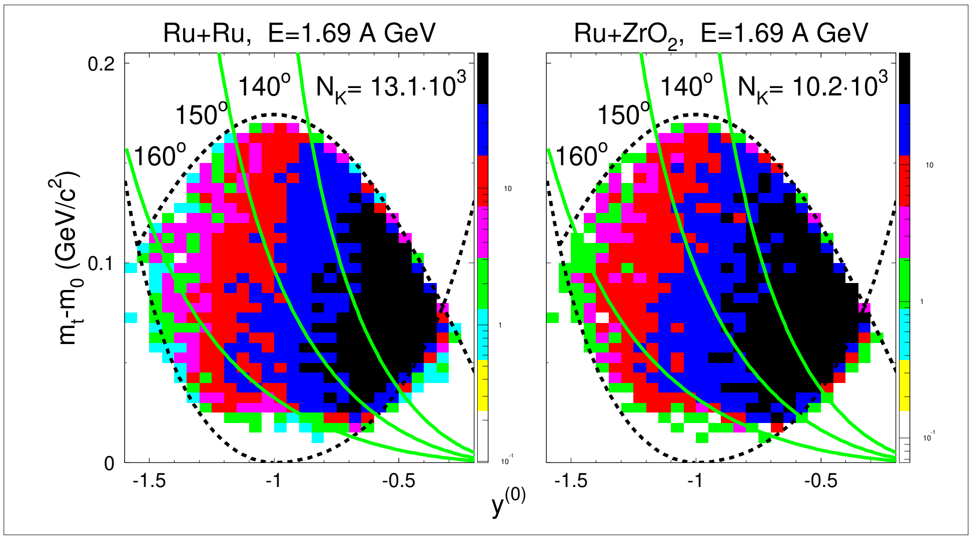

Figure 6.1: *Final-state momentum-space distribution of K^+ mesons in central Ru+Ru (a) and Ru+ZrO$_2$ (b) collisions at 1.69 A GeV beam kinetic energy. The dashed lines depict the geometrical acceptance of the Barrel and the upper momentum limit p=0.45 GeV/c for the K^+ mesons identification. The solid lines correspond to Θ_{cm}=140°, 150° and 160° polar angles. The number of K^+ mesons identified in both experiments are indicated.*

of 2.99±0.03(stat) $\cdot 10^{-3}$ and 3.00±0.03(stat) $\cdot 10^{-3}$ K$^+$ mesons per collision, identical in both experiments. Here, the limited efficiency of the particle identification procedure and the background contamination in the measured yields are not yet accounted for.

In Figure 6.2 the K$^+$ meson yields in the Ru+Ru (a) and Ru+ZrO$_2$ (b) experiments are shown as a function of transverse mass for different slices of normalized rapidity. The spectra are multiplied by subsequent powers of two, in order to allow presentation on one plot. The error bars indicate the uncertainty due to the statistical fluctuations. In some cases they are smaller than the symbol sizes. In addition to the total detection rates, the slopes of the corresponding spectra measured in both experiments (fits not shown in the figure) turned out to be the same within the statistical uncertainties. This means that the difference between the targets does not influence the production of K$^+$ mesons, at least as far as the measured fraction of the momentum space is concerned. Therefore, in the following part of this chapter, K$^+$ meson yields measured in both experiments are combined in order to reduce the statistical errors of the extracted results.

6.2 Transverse-mass spectra

Figure 6.3a shows again the K$^+$ meson yields as a function of m_t for different slices of normalized rapidity. In order to allow presentation on one plot, the spectra are

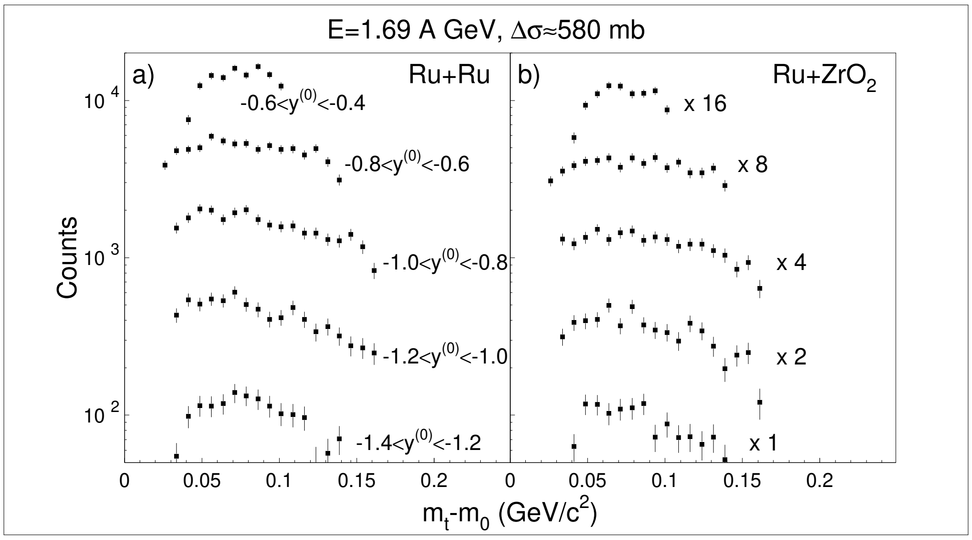

Figure 6.2: *K^+ meson yields in central Ru+Ru (a) and Ru+ZrO_2 (b) collisions. The yields are plotted as a function of transverse mass. The spectra measured in different rapidity slices are multiplied by subsequent powers of two, indicated in panel (a).*

multiplied by subsequent powers of two. This time, the statistics of both experiments are combined. The grey shaded bands represent the variation of the results when the identification conditions are changed from 5.13 to 5.14. This is interpreted as an estimate of the systematic errors. Depending on the rapidity region, differences in the order of 10 to 50% can be observed between K^+ meson yields extracted with different identification conditions.

The subsequent panels of Figure 6.3 show the evolution of the systematic errors when various corrections are applied to the directly measured K^+ meson yields. As shown in Figure 6.3b, the errors get substantially reduced (to less than 25%) when the efficiency corrections are applied. The corrections are determined separately for each set of the identification conditions (5.13 and 5.14), following the method described in Section 5.4. In addition to the reduction of the systematic uncertainties and to an overall scaling of the measured yields, a systematic change of the slopes of the spectra can be observed. Figure 6.3c illustrates how the systematic errors increase when the ±10% variation of the efficiency is allowed as discussed in Section 5.6. Figure 6.3d shows the K^+ meson yields after subtracting the background contamination from π^+ mesons. The amount of the contamination in the yield measured at given $y^{(0)}$ and m_t was derived from the parametrization 5.10 using the functional relationship $p{=}p(m_t, y^{(0)})$. The corresponding dependencies are shown in Figure 5.10f. The corrections allow for the ±20% variation of the background content as discussed in Section 5.6. Accidentally, after the latter corrections, the slopes of the spectra change systematically, and correspond more or less to the slopes of the spectra shown in Figure 6.3a, obtained without applying any corrections.

The points in panel (d) of Figure 6.3 depict the K^+ meson yields extracted with

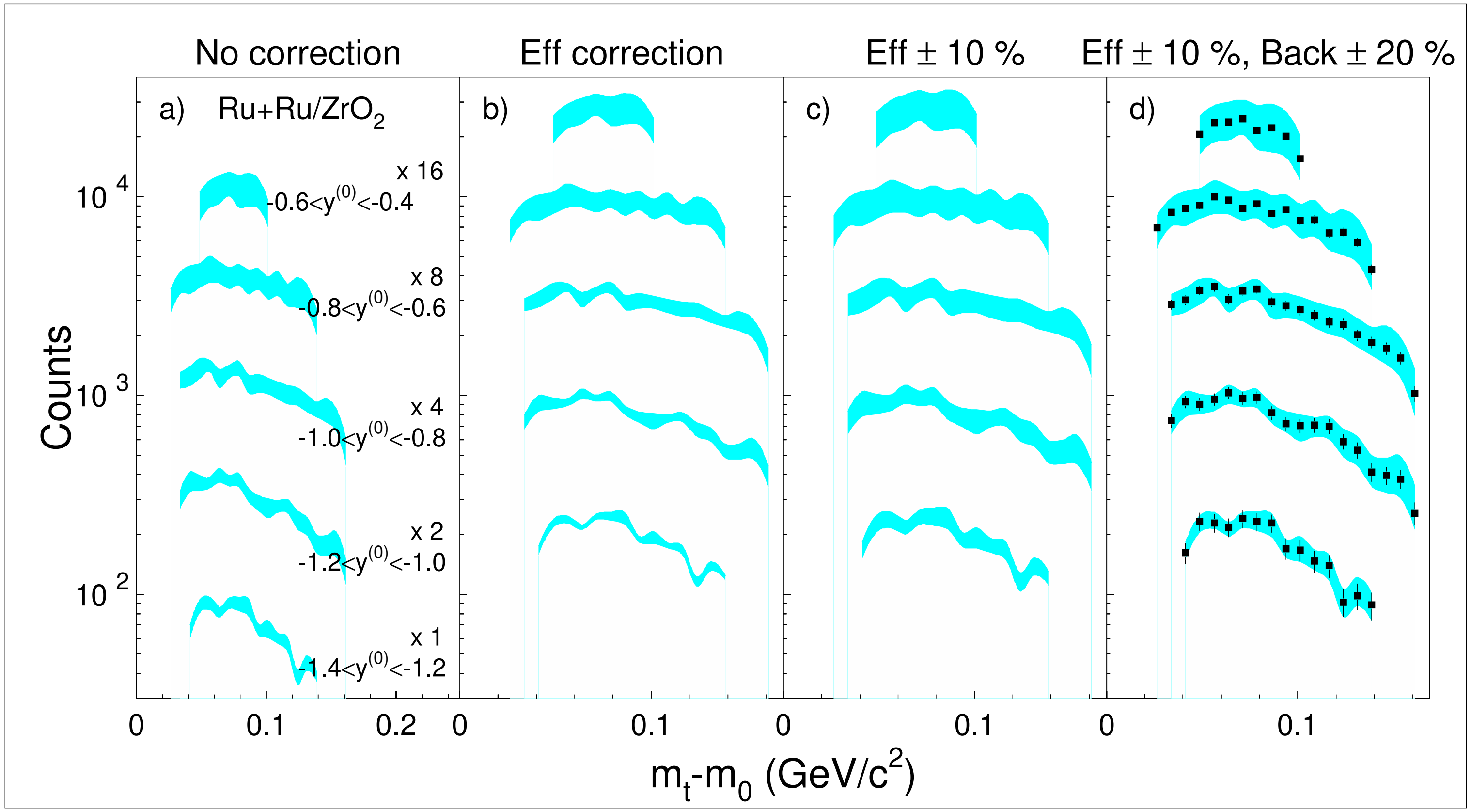

Figure 6.3: *K^+ meson yields in central Ru+Ru and Ru+ZrO$_2$ collisions (the statistics of both experiments are combined). The yields are plotted as a function of transverse mass. The spectra measured in different rapidity slices are multiplied by subsequent powers of two, indicated in panel (a). The grey shaded bands on the subsequent panels illustrate how the systematic uncertainty of the results changes when different corrections are applied.*

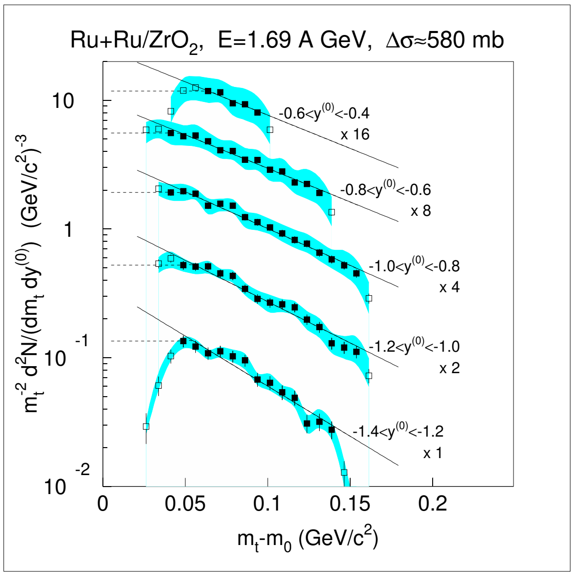

Figure 6.4: *Transverse mass spectra of K^+ mesons in central Ru+Ru and Ru+ZrO$_2$ collisions (the statistics of both experiments are combined). The spectra measured in different slices of normalized rapidity are multiplied by subsequent powers of two. The solid lines show the fits of the form 6.2. The dashed lines depict an alternative way of extrapolating the measured spectra into the low-m_t region where the K^+ meson yields are not measured.*

the initially considered identification conditions 5.4. The error bars represent the statistical uncertainty of the results.

In Figure 6.4 the so-called transverse-mass spectra of K$^+$ mesons are shown. The measured yields are normalized to the number of considered events, 7.8·10^6 (cf. Table 3.1), and to the bin widths in $y^{(0)}$ and m_t. Since only particles which are detected by the Barrel are included, the yields are corrected in order to account for particle decay on the way from the target position to the point of the detection. The corrections depend only on m_t since

$$\exp\left(\frac{TOF}{\gamma \cdot \tau}\right) = \exp\left(\frac{s/(\beta c)}{p/m_0(\beta c) \cdot \tau}\right) = \exp\left(\frac{s_\perp \cdot m_0 c^2}{p_t \cdot c\tau}\right) . \tag{6.1}$$

Here, τ=1.237·10^{-8}s is K$^+$ meson mean life time, m_0=0.494 GeV/c^2 is K$^+$ meson mass, p and p_t=$\sqrt{m_t^2 c^2 - m_0^2 c^2}$ are the total and the transverse momenta, s and $s_\perp(m_t)$ are the flight path and its projection onto the xy plane respectively.

The spectra shown in Figure 6.4 are also multiplied by a factor $1/m_t^2$. In such a representation, a distribution of particles emitted isotropically from a thermally-equilibrated source correspond to straight lines in a logarithmic scale. The lines in Figure 6.4 depict the fits of such Boltzmann-like functional forms

$$\frac{1}{m_{\rm t}^2}\,\frac{{\rm d}^2{\rm N}}{{\rm d}m_{\rm t}{\rm d}y^{(0)}} = A\; exp\left[\frac{-m_{\rm t}}{T_B}\right] \tag{6.2}$$

to the measured spectra. A – the normalization and T_B – the inverse slope are the fit parameters. For each spectrum, the formula 6.2 is fitted in a limited range of m_t depicted with filled symbols. The excess of the fitted function over the measured K$^+$ meson yield at low m_t is partially due to the detection inefficiency of low momentum kaons, which loose too much of their energy on the way to the Barrel, and, thus,

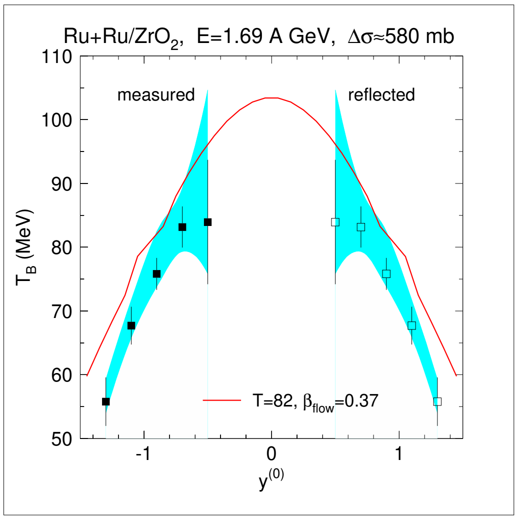

Figure 6.5: *The inverse slope parameters, T_B, of K^+ mesons transverse mass spectra. plotted as a function of $y^{(0)}$. The points are reflected with respect to mid-rapidity. The line represents the values of T_B for a distribution of K^+ mesons emitted isotropically from a thermally-equilibrated source of temperature T=82 MeV, which expands radially with velocity β_{flow}=0.37. See Section 6.6 for further discussion.*

can not be well identified[2]. However, it is as well possible that the K$^+$ meson yields really drop at low m_t, for example, as indicated by the dashed lines in Figure 6.4. This has to be taken into account when the measured spectra are extrapolated to the not measured region of low m_t, and when K$^+$ meson yields as a function of rapidity are studied (see Section 6.4 for further discussion).

6.3 Apparent temperatures

In Figure 6.5 the values of the inverse slope parameters of the fits 6.2, i.e., the so-called apparent temperatures T_B, are plotted as a function of normalized rapidity. The error bars represent the statistical uncertainties. The grey shaded bands depict the systematic errors.

Since the considered reactions are mass-symmetric, the momentum-space distribution of K$^+$ mesons is symmetric with respect to mid-rapidity. Therefore, the symbols on the target-rapidity side are reflected onto the projectile-rapidity side. The values of T_B increase towards mid-rapidity, which is the expected behaviour in the case of an isotropic emission from a thermally-equilibrated source.

6.4 Rapidity-density distribution

In order to extract the rapidity-density distribution of K$^+$ mesons the m_t spectra are extrapolated to regions of high and, more importantly, low m_t. The extrapolation is based on the assumption that for each rapidity slice the K$^+$ meson yields depend on m_t as described by the functional form 6.2. This would be the case if, for example, the momentum-space distribution of K$^+$ meson were compatible with an

---

[2] The effect was discussed in Section 5.4 when the method of determining the efficiency of the identification procedure was described.

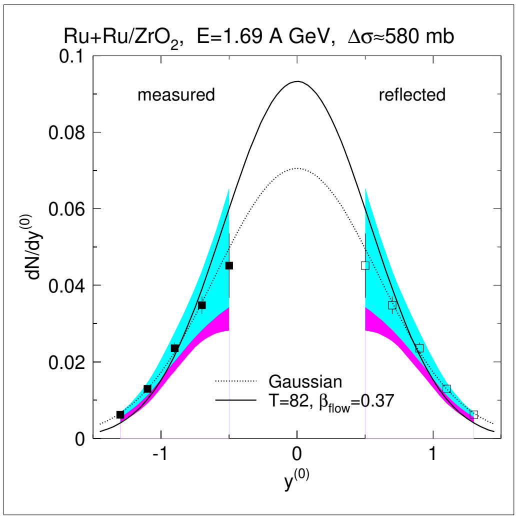

Figure 6.6: *Rapidity-density distribution of K^+ mesons in central Ru+Ru and Ru+ZrO$_2$ collisions (the statistics of both experiments are combined). The measured yields are reflected with respect to the mid-rapidity. The dotted line shows the fit of the gaussian function, with which the spectrum is extrapolated to the mid-rapidity region. The solid line depicts the distribution of K^+ mesons emitted isotropically from a thermally-equilibrated source of temperature T=82 MeV, which expands radially with velocity β_{flow}=0.37. The normalization of the thermal spectrum is fitted to the experimental distribution.*

isotropic-emission pattern from a thermally-equilibrated source. Such an assumption is supported by the results presented in Chapter 4, which suggest that the system is thermally equilibrated.

The functions 6.2 fitted to the m_t spectra in different rapidity slices are integrated from m_t=0 to m_t=∞. The integrals estimate the K$^+$ meson yields at given $y^{(0)}$. In Figure 6.6 the resulting rapidity-density distribution, $dN/dy^{(0)}$, is shown. Since the distribution is symmetric with respect to mid-rapidity, the points on the target-rapidity side are reflected onto the projectile-rapidity side. The statistical uncertainties are represented by the error bars. Two contributions to the systematic uncertainty, depicted by the two grey shaded bands, are considered. The light-grey shaded band illustrates, as before, the variation of the results when the identification conditions are changed from 5.13 to 5.14, and the appropriate corrections are applied as described in Section 6.2. The dark-grey shaded band corresponds to the uncertainty of K$^+$ meson yields at low m_t. It was estimated by assuming that the K$^+$ meson yield changes at low m_t as indicated by the dashed lines in Figure 6.4 rather than rises exponentially. The integrals of these dependencies from m_t=0 to m_t=∞ turned out to be up to 15% smaller than those of the exponential functions 6.2 fitted to the measured portion of the m_t spectra. On the other hand, it was thought that the m_t spectra are unlikely to grow at low m_t faster than exponential functions.

In order to estimate the total K$^+$ mesons production probability (P_{AA}), the rapidity density distribution is fitted with Gaussian as depicted by the dotted line in Figure 6.6. In this way, the measured yields are extrapolated to the mid-rapidity region which is not measured. The fitted form is integrated from $y^{(0)}$=-∞ to $y^{(0)}$=+∞. The uncertainty of the K$^+$ meson yield at mid-rapidity increases further the systematic error of P_{AA}. In Section 6.6 it will be argued that the integral of the Gaussian fitted to the measured portion of the $dN/dy^{(0)}$ distribution can underestimated P_{AA}

by about 10%.

Taking this into account, the estimate of the total K^+ meson production probability in central Ru+Ru/ZrO$_2$ collisions ($\Delta\sigma\simeq$580 mb) at 1.69 A GeV beam kinetic energy is

$$P_{AA} = 0.15 \pm 0.02(\mathrm{stat})^{+0.02}_{-0.03}(\mathrm{syst}) \ . \tag{6.3}$$

6.5 Centrality dependence of the K^+ mesons production probability

In order to study the dependence of the K^+ meson production on collision centrality, the medium-bias sample of events considered in the previous sections was subdivided into three subsamples of different centralities. As described in Section 3.2, the selection of events was based on the total multiplicity of detected particles TMUL. The selection conditions and the values of the parameters which characterize different event categories ($\Delta\sigma$, $< b >_{geo}$, $< A_{part} >$) are listed in Table 3.1.

Figure 6.7 shows the $dN/dy^{(0)}$ distributions of K^+ mesons extracted for three considered event subsamples. As before, the yields of K^+ mesons measured in both experiments are added in order to reduce the statistical uncertainties. Within the accuracy of the measurements, the slopes of the corresponding m_t spectra and the widths of the $dN/dy^{(0)}$ distributions shown in Figure 6.7 turned out to be similar for all three event categories. This means that the final-state momentum-space distribution of K^+ meson does not change substantially with collision centrality. However, one has to keep in mind that (i) due to the hardware-trigger selection, all three considered event categories belong to the centralmost part of the reaction cross section ($\Delta\sigma\simeq$580 mb) and (ii) due to the fluctuations of the multiplicities of the detected particles, selecting event subsamples according to TMUL in fact allows for mixing in one subsample events of quite different impact parameters. Centrality dependence of any observable can be easily smeared out by this mixing.

Each of the distributions shown in Figure 6.7 is fitted with a Gaussian. By integrating the fitted functions from $y^{(0)}$=-∞ to $y^{(0)}$=+∞, the K^+ meson production probabilities are estimated. Figure 6.8a shows the resulting dependence of P_{AA} on event centrality. The mean number of nucleons participating in the reactions $<A_{part}>$ was determined for each considered event category following the method described in Section 3.2. The corresponding values of $<A_{part}>$ are collected in Table 3.1. The grey shaded bands in Figure 6.8 depict two contributions to the systematic error. The inner band represents the variation of the results with respect to the change of the identification conditions. The outer band shows in addition the uncertainty of P_{AA} due to the extrapolation of the measured yields to not measured regions of the momentum space (low-m_t and mid-rapidity regions).

P_{AA} grows the more central the collisions are. This is partially a trivial effect, because with increasing centrality the number of nucleons participating in a collision increases, and, hence, more K^+ mesons are produced per collision. In order to elim-

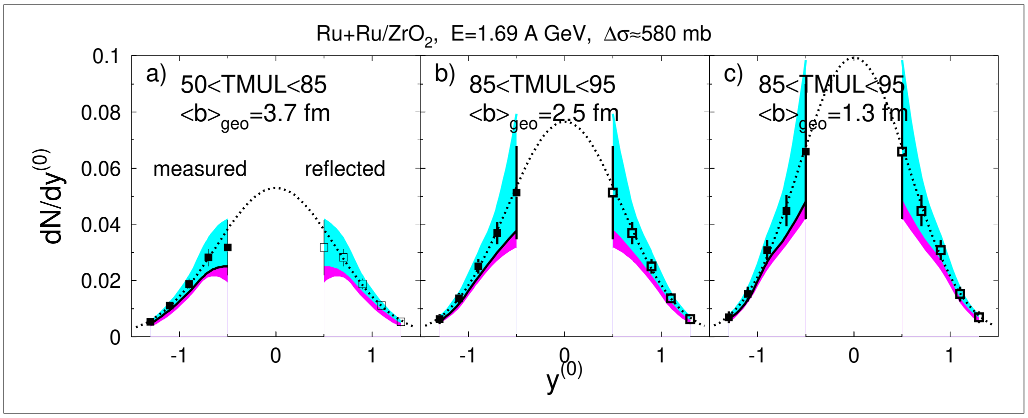

Figure 6.7: *Rapidity-density distributions of K^+ mesons measured in collisions of different centralities. The statistics of both Ru+Ru and Ru+ZrO$_2$ experiments are combined. The dotted lines show the fits of gaussian functions with which the distributions are extrapolated to the mid-rapidity region.*

inate the effect of the volume of the participant zone, one considers the production rate of K$^+$ mesons per participating nucleon, defined as

$$P_{NN} = P_{AA} / < A_{part} > \quad . \tag{6.4}$$

In Figure 6.8b the dependence of P_{NN} on $<A_{part}>$ is shown. It can be noticed that P_{NN} increases with collision centrality although the dynamical range of $<A_{part}>$ which is sampled in the experiment is fairly narrow. Similar, but more pronounced effects, were observed for other systems in the experiments of the KaoS collaboration. For example, Figure 6.9 shows the dependence of P_{NN} on $<A_{part}>$ for the Ni+Ni system at 1.8 A GeV beam kinetic energy [45]. The dependence was well described by the fit of the form

$$P_{NN}(A_{part}) = C \cdot (A_{part})^{\alpha} \ , \tag{6.5}$$

with α=0.65. Other data sets, for example, that of the Ni+Ni system at much lower beam kinetic energy of 1.0 A GeV and that of the heavier, Au+Au system at 1.0 A GeV bombarding energy, were fitted with similar values of α, in the range from 0.7 to 0.8 [45, 77]. This suggests that α does not depend strongly neither on the system mass nor on the beam energy.

If K$^+$ mesons were produced mainly in elementary, nucleon-nucleon interaction, one would expect P_{AA} rising linearly with the volume of the participant zone, i.e., with $<A_{part}>$. In contrast, it can be noticed that there are more K$^+$ mesons produced in central than in peripheral collisions, even after eliminating the effect from the volume of the participant zone. A pronounced increase of P_{NN} with $<A_{part}>$ suggests that in heavy-ion collisions multi-step processes, for example, via an intermediate production of pions, contribute substantially to the total production rate of K$^+$ mesons. This effect was predicted by transport models. The lines in Figure 6.10 illustrate how individual elementary processes contribute to the total production

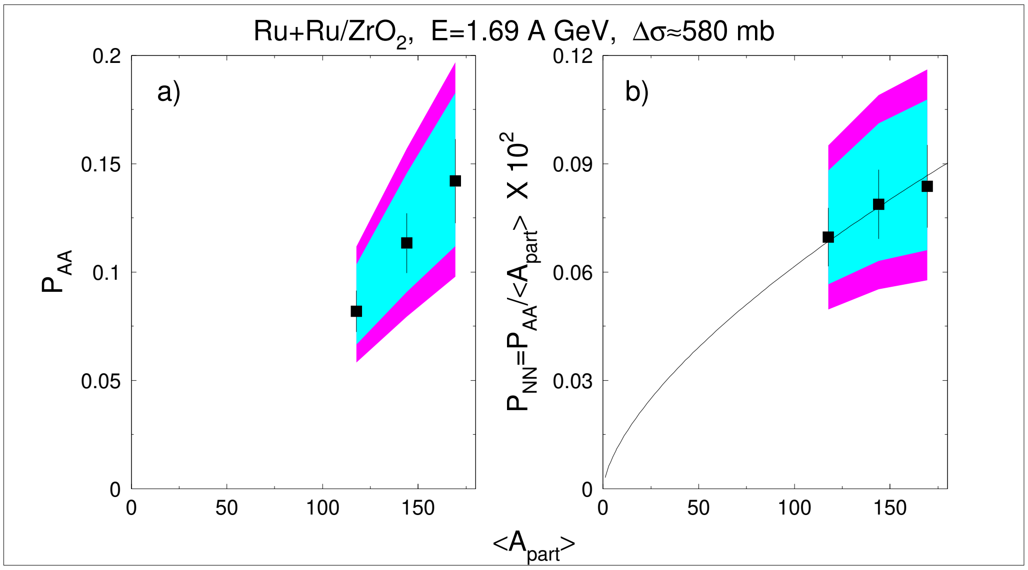

Figure 6.8: *(a) K^+ meson production probability, P_{AA}, as a function of the mean number of participating nucleons, $<A_{part}>$. The statistics of both Ru+Ru and Ru+ZrO$_2$ experiments are combined. (b) Same as (a) but P_{AA} over $<A_{part}>$ is plotted. The line depicts the fit of the formula 6.5 with α fixed to 0.65 and C=3.1·10^{-5} being the fitted parameter.*

cross section of K$^+$ mesons in Au+Au collisions at 1.0 A GeV beam kinetic energy. The predictions of the RBUU model of the Giessen group [9] are compared to the experimental data of the KaoS collaboration [10, 77].

In this work, the observed dependence of P_{AA} on $<A_{part}>$ is parametrized by

$$P_{AA}(A_{part}) = 3.1 \cdot 10^{-5} \cdot (A_{part})^{1.65} , \qquad (6.6)$$

where the exponent α is fixed to 1.65, and C=3.1·10^{-5} is the fitted parameter. The fit is depicted by the line in Figure 6.8b. The average K$^+$ meson production probability is estimated as the integral of this dependence over all impact parameters

$$< P_{AA} >= \frac{\int_0^{b_{geo}^{max}} P_{AA}(A_{part}(b)) \cdot 2\pi b db}{\int_0^{b_{geo}^{max}} 2\pi b db} \simeq 2.9 \cdot 10^{-2} . \qquad (6.7)$$

In the above relation, b_{geo}^{max}=11 fm is the maximum geometrical impact parameter (cf. Eq. 3.3), and the dependence of A_{part} on b is approximated by the term which is integrated in Eq. 3.6. In order to facilitate the comparison with results obtained for systems of different sizes, $<P_{AA}>$ is divided by the the mean number of participating nucleons for an inclusive measurement. The integration in Eq. 3.6 gives $<A_{part}>_{incl} \simeq A_{proj}/2=48$. This leads to

$$< P_{AA} > / < A_{part} > \simeq 6 \cdot 10^{-4} . \qquad (6.8)$$

The systematic uncertainty of this estimate is large, mainly due to the integration 6.7, with large uncertainties of parameters C and α. Nevertheless, in Figure 6.11

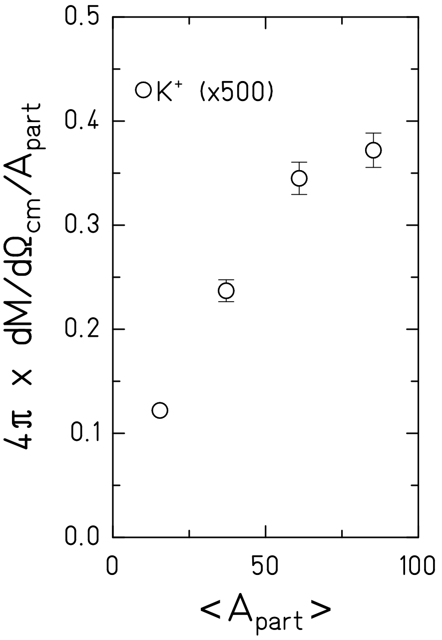

Figure 6.9: *$<A_{part}>$ dependence of the K^+ meson production probability per unit solid angle in the CM reference frame and per participating nucleon for the Ni+Ni system at 1.8 A GeV beam kinetic energy. The plot is adapted from [45].*

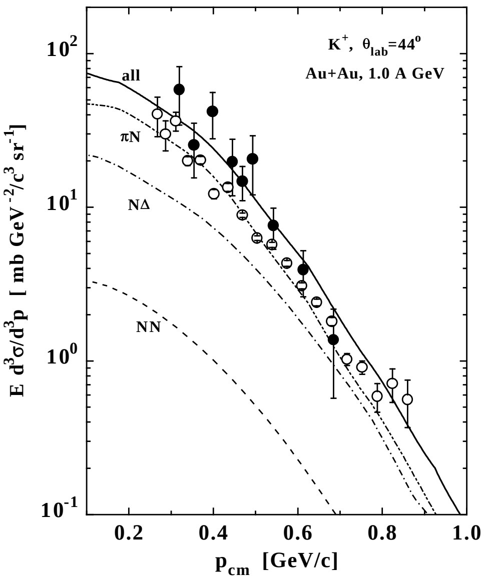

Figure 6.10: *K^+ meson production cross section in Au+Au reactions at 1.0 A GeV beam kinetic energy [10, 77]. The lines show contributions to the total production rate of individual elementary processes as predicted by the RBUU model. The plot is adapted from [9].*

the extracted value is compared to the results obtained for other systems in this energy regime [79]. The plot will be discussed further in Chapter 6.8.

6.6 Thermal equilibrium

The solid line in Figure 6.5 shows the values of the inverse slope parameters, T_B, for a distribution of K$^+$ mesons emitted isotropically from a radially-expanding, thermally-equilibrated source (cf. Appendix A.3). The parameters of the distribution, T=82 MeV and β_{flow}=0.37, are chosen as those that fit well the spectra of π^+ mesons, protons and deuterons, and, hence, describe the conditions at the freeze-out (cf. Section 4.3). The slopes of the measured m_t spectra of K$^+$ mesons are systematically lower by about 8 MeV than those of the thermal distribution. Such a small difference (in comparison to the uncertainties of the experimental results) suggests that the thermal equilibrium between K$^+$ mesons and the surrounding matter is at least approached. This is surprising because K$^+$ mesons are supposed to leave the reaction zone almost undisturbed. A small cross section of the K$^+$N elastic scattering in the order of σ=10 mb (for relative momenta lower than 0.7 GeV/c) [14]

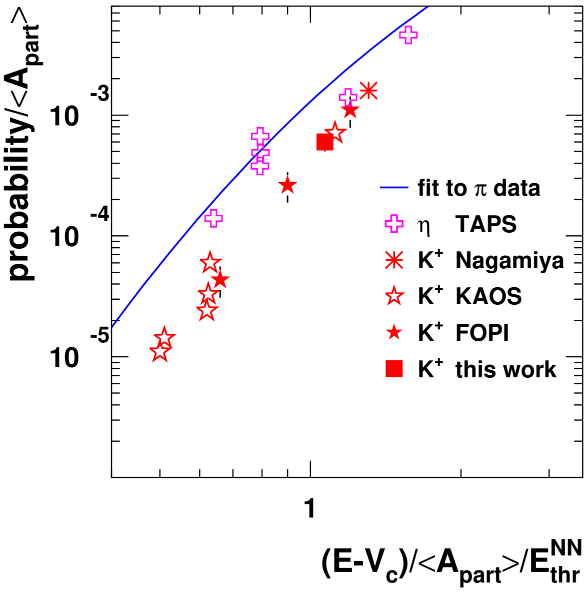

Figure 6.11: *Production probability* $<P_{AA}>/<A_{part}>$ *of strange as well as non-strange mesons in heavy-ion collisions at intermediate energies. The line shows the fit to the pion data. In order to eliminate the effect from the volume of the available momentum space, the beam energy above the Coulomb barrier is divided by the threshold energy of the production in elementary, nucleon-nucleon collisions. This representation of the data was first proposed in [78]. The plot is adapted form [79].*

corresponds to a relatively long mean free path of $\lambda \simeq 7$ fm at the normal nuclear matter density. The cross section of the charge-exchange process $K^+n \to K^0p$ is still smaller [15]. The question of thermal equilibrium between the K^+ mesons and the surrounding matter will be discussed further in the next section.

The observed dependence of T_B on rapidity could be as well reproduced with other sets of parameters T and β_{flow}. For example, neglecting the radial flow (β_{flow} set to 0), a temperature of about 100 MeV would be needed in order to fit the experimental results[3].

The solid line in Figure 6.6 shows the $dN/dy^{(0)}$ distribution of K^+ mesons emitted isotropically from the thermal source discussed above (T=82 MeV, β_{flow}=0.37), with the overall normalization fitted to the experimental distribution. Because of the excess at mid-rapidity, the integrated yield of the thermal spectrum is about 10% higher than the integral of the Gaussian fitted to the experimental distribution (dotted line). Therefore, in Sections 6.4 and 6.5 a contribution of the same order was added to the systematic errors of the total K^+ meson production probability. On the other hand, it can be noticed that the measured K^+ meson $dN/dy^{(0)}$ distribution is wider than the thermal spectrum. This suggests that the final-state momentum-space distribution of K^+ mesons may not be isotropic.

6.7 Kinetic-energy spectra

Figure 6.12 shows the K^+ meson yields as a function of kinetic energy in the CM reference frame (E_{cm}^{kin}). The yields measured in central Ru+Ru and Ru+ZrO$_2$ collisions

---

[3] When β_{flow}=0, the temperature, T, of the thermal distribution can be easily read out as the value of T_B at mid-rapidity.

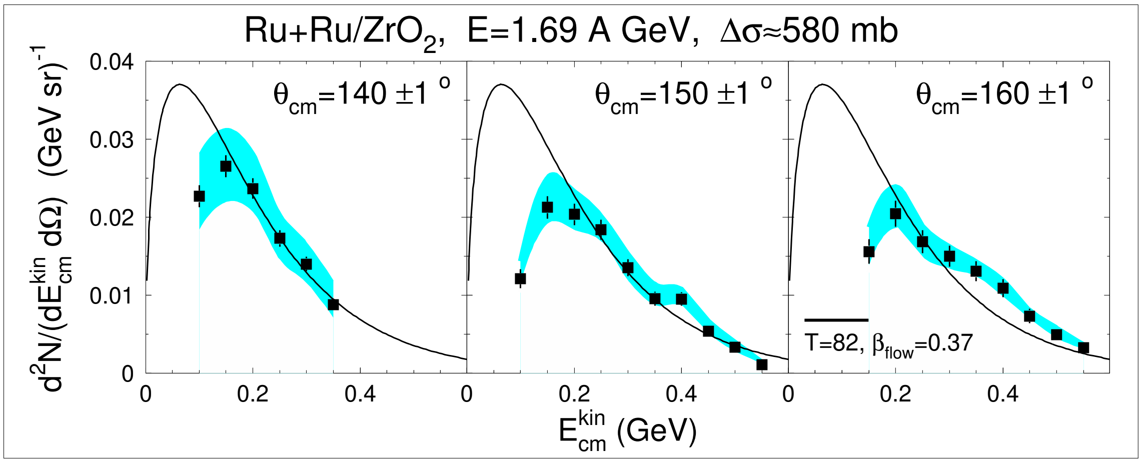

Figure 6.12: *K^+ meson kinetic energy spectra in the CM reference frame measured at different polar angles Θ_{cm} in central Ru+Ru and Ru+ZrO_2 collisions (the statistics of both experiments are combined). The lines represent the spectra described by formula A.4 with the parameters T=82 MeV and β_{flow}=0.37.*

are added. The kinetic-energy spectra are extracted in narrow bins of ±1° centered at Θ_{cm}=140°, 150° and 160° polar angles. The spectra are corrected in order to account for the decays of K$^+$ mesons, the efficiency of the identification procedure, and the background contamination of the directly extracted yields. The methods are similar to those discussed in Section 6.2. The corrections which account for the efficiency are determined directly as shown in Figure 5.9. The corrections which account for the background contamination are derived from parametrization 5.10 using the functional relationship $p=p(E^{kin}_{cm}, \Theta_{cm})$. The corresponding dependencies are shown in Figure 5.10g.

The distributions shown in Figure 6.12 are normalized to the solid angle $\Delta\Omega = 2\pi\cdot\Delta(\cos(\Theta_{cm}))$ within which the yields were measured ($2\cdot\pi$ in the azimuthal (ϕ) and 2° in the polar (Θ_{cm}) angles respectively).

The lines in Figure 6.12 show the kinetic-energy spectra of K$^+$ mesons emitted isotropically from a radially-expanding, thermally-equilibrated source. The lines are drawn according to formula A.4 with the parameters T=82 MeV and β_{flow}=0.37. The overall normalization of the thermal distributions is fitted to the spectrum extracted at Θ_{cm}=140°.

One observes a rather good correspondence between the measured K$^+$ meson yields and the thermal distributions at all considered Θ_{cm} angles, which suggests that the thermal equilibrium between K$^+$ mesons and the surrounding matter is approached.

On the other hand, a little excess of the measured yield over the thermal spectrum at the most backward direction (cf. Figure 6.12c) can be noticed. This is again an indication of an anisotropy of the K$^+$ meson final-state momentum-space distribution. A similar observation of a forward-backward peaked K$^+$ meson distribution was reported in [23] for the Au+Au system at 1.0 A GeV beam kinetic energy.

6.8 Chemical equilibrium

In Figure 6.11 the average K^+ meson production probabilities $<P_{AA}>/<A_{part}>$ measured for different systems are compared to the production probabilities of non-strange η mesons and pions [79] (the measurements on pions are represented by the fit to the available data – solid line). The beam energies above the Coulomb barrier are divided by the threshold energies of the production in elementary, nucleon-nucleon collisions. In this way the differences due to the available momentum space between the production of kaons and lighter non-strange mesons is eliminated.

If the system approached the chemical equilibrium, the production probabilities presented in Figure 6.11 should be similar for all meson species. In contrast, one observes that the production rate of strange mesons is much lower. This suggests that, although the thermal equilibrium between K^+ mesons and the surrounding matter may be achieved, the system does not approach the chemical equilibrium. The conclusions presented in [80] are in line with the above observation. Transport models predict that in heavy ion collisions the thermal equilibrium is reached about 7 fm/c after the beginning of the reaction. In contrast, the chemical equilibration time for strangeness in the order of 40 fm/c is much longer than the reaction time.

6.9 Comparison to predictions of the transport model RBUU

In Figure 6.13 the K^+ meson observables from the Ru+Ru and Ru+ZrO_2 experiments are compared to the predictions of the RBUU transport model of the Giessen group [81]. Some details about the model are given in Appendix A.4. The model calculations were performed for the Ru+Ru system at 1.69 A GeV beam kinetic energy. All studied observables are shown in Figure 6.13 : transverse mass spectra (a), inverse slope parameters (b), rapidity densities (c), production probabilities (d), and kinetic energy spectra (e-g),

The results of the calculations are filtered with the condition which describes the detector acceptance[4]

$$130^o < \Theta_{lab} < 40^o, \; p_t > 0.1 \text{ GeV/c}, \; p < 0.45 \text{ GeV/c} . \tag{6.9}$$

In order to roughly match the experimental centrality selection ($\Delta\sigma \simeq 580$ mb), only RBUU events of impact parameters b<4 fm are considered (cf. Table 3.1).

Predictions of two versions of the transport model are shown. The solid lines represent the results of the model with bare K^+ meson mass. The dashed lines depict the results of the version with in-medium modifications of K^+N potential (cf.

---

[4] A more realistic filter based on the GEANT simulation package has recently become available. It has not been however developed enough to allow reliable comparison between the model results and the measurements presented in this work.

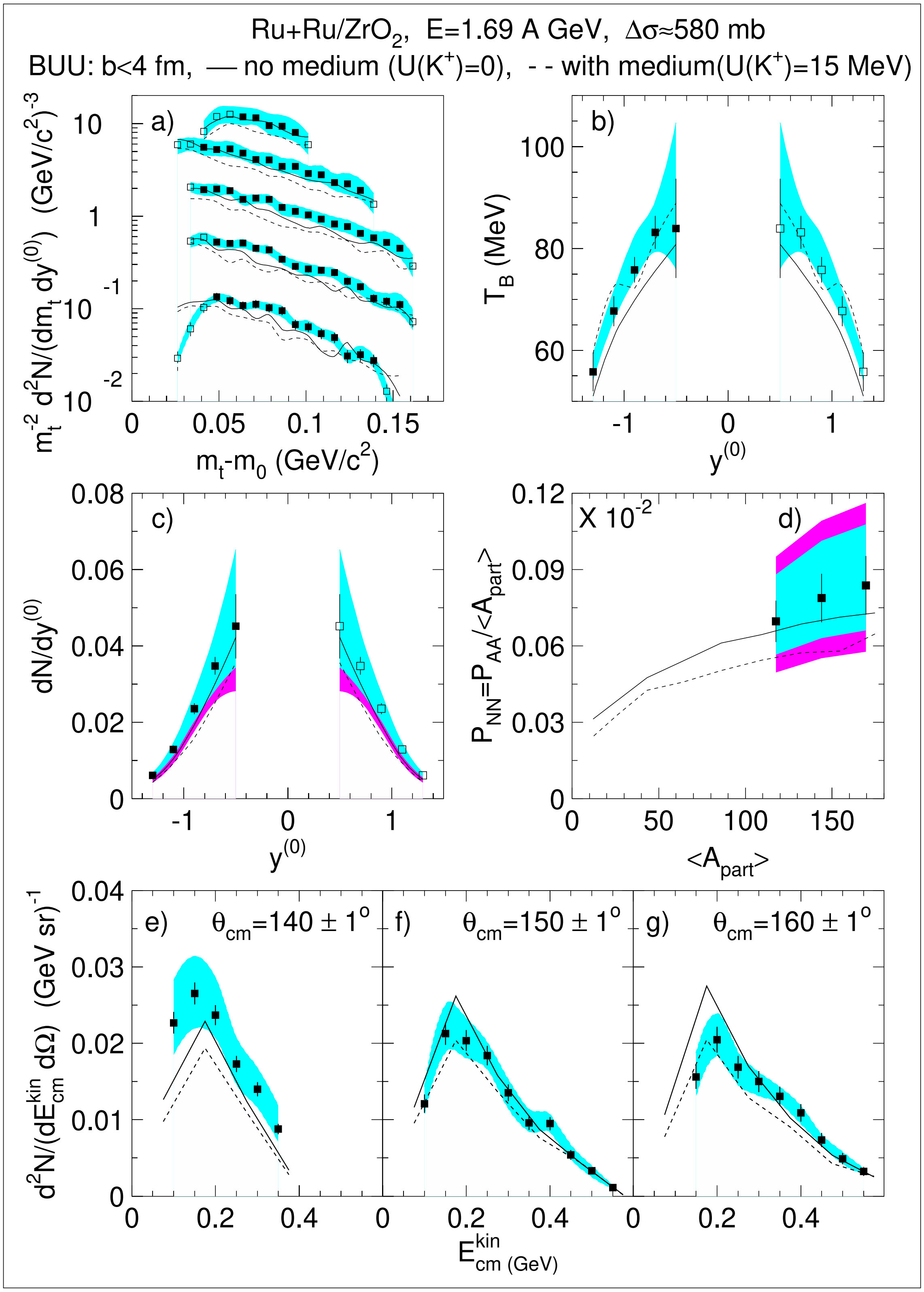

Figure 6.13: *Comparison between the data and the predictions of the RBUU transport model on the production of K^+ mesons in central Ru+Ru and Ru+ZrO_2 collisions (statistics of both experiments are combined). Results of two versions of the model are shown. Solid lines represent the version with bare K^+ meson mass. Dashed lines are for the model with in-medium modifications of kaons.*

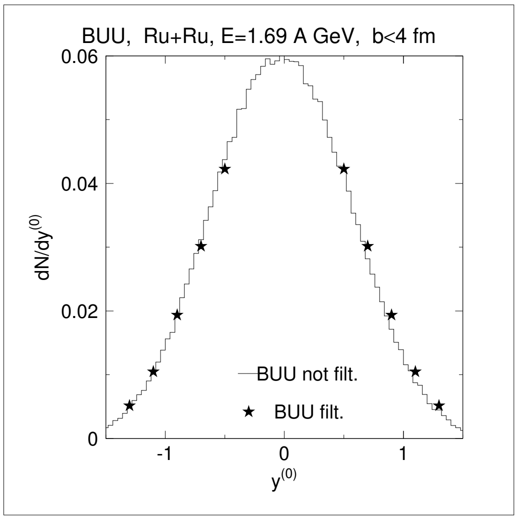

Figure 6.14: *The effect of the geometrical bias on rapidity-density distributions. The K^+ meson $dN/dy^{(0)}$ distribution predicted by the RBUU model (histogram) is compared to the distribution obtained by integrating the exponential fits to the m_t spectra in the regions corresponding to the detector acceptance (points). The results are for the version of the model with bare K^+ meson mass.*

Appendix A.4). The change of the effective K^+ meson mass (m^*_{K+}) is parametrized in a way that leads to a 15 MeV increase of m^*_{K+} at the normal nuclear matter density.

Large systematic errors on the extracted K^+ meson yields make a definite distinction between the two model predictions difficult. On the one hand, the details of the momentum-space distribution, like for instance the slopes of the m_t spectra (cf. Figure 6.13b), are reproduced better by the model with in-medium modifications of kaons. However, on the other hand, good correspondence between the measured K^+ meson yields and the model predictions is found if a bare K^+ meson mass is assumed. A discrepancy of 20% at the most can be observed, which, in most of the cases, is inside the systematic uncertainty of the experimental results. When the in-medium modifications of kaons are included, the model underestimates the K^+ meson yields by a greater amount. Even more pronounced discrepancy between the experimental data and the predictions of the model with in-medium effects on kaons was observed for the lighter, Ni+Ni system [9].

It was argued in Chapter 6.4 that the extrapolation and integration of the m_t spectra over the not measured, low-m_t region can systematically influence the resulting $dN/dy^{(0)}$ distributions. The amount of the distortion was tested on the results of the RBUU model[5]. The histogram in Figure 6.14 shows the $dN/dy^{(0)}$ distribution of K^+ mesons as predicted directly by the model. The points represent the distribution obtained when the model results were filtered with the condition 6.9, and then extrapolated to the not measured regions of the momentum space. In the experimentally accessible range of rapidities, both $dN/dy^{(0)}$ distributions are compatible. Thus, it can be concluded that, at least as far as the results of the RBUU model are concerned, the method of extracting the $dN/dy^{(0)}$ distribution from the measured portion of the m_t spectra does not introduce a systematic distortion.

---

[5] Here, the results of the model with bare K^+ meson mass are presented. However, same effects were observed for the other version of the model.

Chapter 7

Directed side-flow pattern of K^+ mesons

In this chapter, the directed side-flow pattern of K^+mesons in the Ru+Ru and Ru+ZrO_2 experiments will be discussed. As for protons (cf. Section 4.4), the mean value of the in-plane component of the transverse momenta ($<p_x>/m_0c$) will be extracted as a function of rapidity. The dependence of $<p_x>$ on the transverse momentum will be shown as well.

Only central collisions selected by the medium-bias trigger condition and other requirements described in Chapter 3 are considered. The reaction plane is reconstructed for each event following the method described in Section 3.3.

7.1 Flow pattern

Figure 7.1 shows the directed side-flow pattern of K^+ mesons in the Ru+Ru and Ru+ZrO_2 experiments. The error bars represent to the statistical uncertainties. The systematic errors are depicted by the grey shaded bands. They correspond to the variation of the results with respect to the change of the identification conditions from 5.14 to 5.13. The biggest effect was observed when the condition on number of hits (NH) was varied. In general, the values of $<p_x>/m_0c$ shift up when the tracks of which NH were small were included.

The results shown in Figure 7.1 are corrected in order to account for the uncertainty of the reaction-plane reconstruction according to formula 4.4. The value of the correction factor, $<\cos(\Delta\Phi)>=0.77$, is taken from Table 3.2. The corrections due to the decay of K^+ mesons on the way to the Barrel are also applied, although they turned out to be negligible. The limited identification efficiency and the background contamination in the directly measured yields are not accounted for. These effects are of less importance here since only the first moments of the yield-distributions are extracted and not the absolute yields.

The flow pattern of K^+ mesons is compared to that of protons, (open symbols in

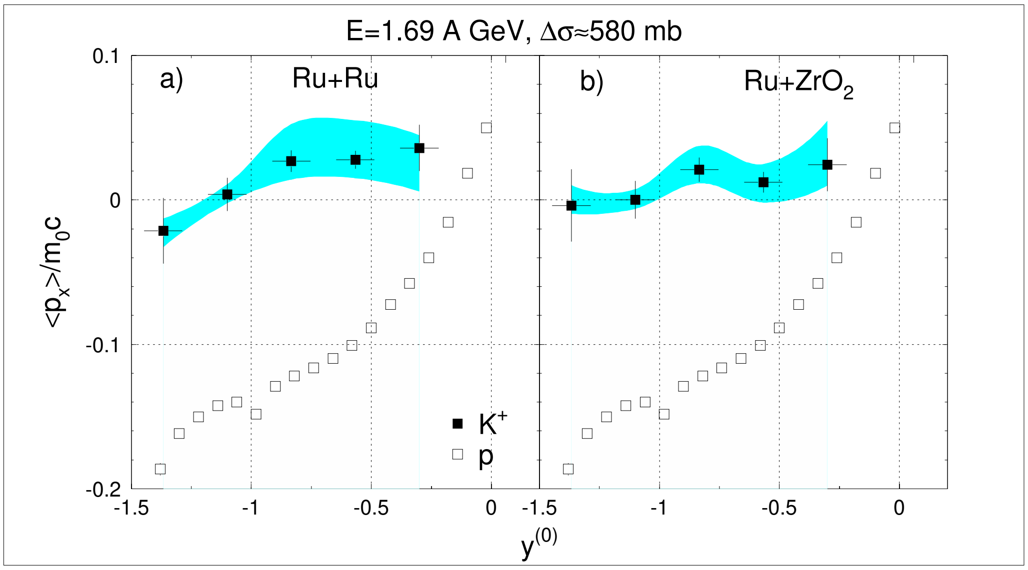

Figure 7.1: *Directed side-flow pattern of K^+ mesons (full symbols) and protons (open symbols) in central Ru+Ru (a) and Ru+ZrO_2 (b) collisions at 1.69 A GeV beam kinetic energy.*

Figure 7.1). K^+ mesons do not flow in the direction of baryons. Within the quoted errors, the magnitude of the flow signal is the same in both experiments.

7.2 Centrality dependence of the K^+ meson flow

Figure 7.2 shows the flow patterns of K^+ mesons in centralmost collisions (selected with the TMUL>95 condition) and in less central collisions (TMUL<85). The results are corrected in order to account for the uncertainty of the reaction-plane reconstruction according to formula 4.4. The values of the appropriate correction factors, $<\cos(\Delta\Phi)>=0.7$ and $<\cos(\Delta\Phi)>=0.8$ for the centralmost and the less central collisions respectively, are taken from Table 3.2. The statistics of both Ru+Ru and Ru+ZrO_2 experiments are combined in order to reduce statistical uncertainties. This is acceptable because, as shown in the previous section, there seems to be no significant difference between the flow patterns of K^+ mesons measured in both experiments.

It can be observed that in the centralmost collisions the K^+ meson flow signal is compatible with zero. On the other hand, in the less central collisions, the values of $<p_x>/m_0c$ are positive in the target-rapidity region. This indicates that K^+ mesons exhibit a so-called anti-flow signal, i.e., the direction of their flow is opposite to that of protons.

In [47], the flow patterns of K^+ mesons and Λ hyperons were analysed for the Ni+Ni system at 1.93 A GeV. It was shown that, in contrast to K^+ mesons, Λ hyperons follow the proton flow. This is surprising since Λ hyperons and K^+ mesons are

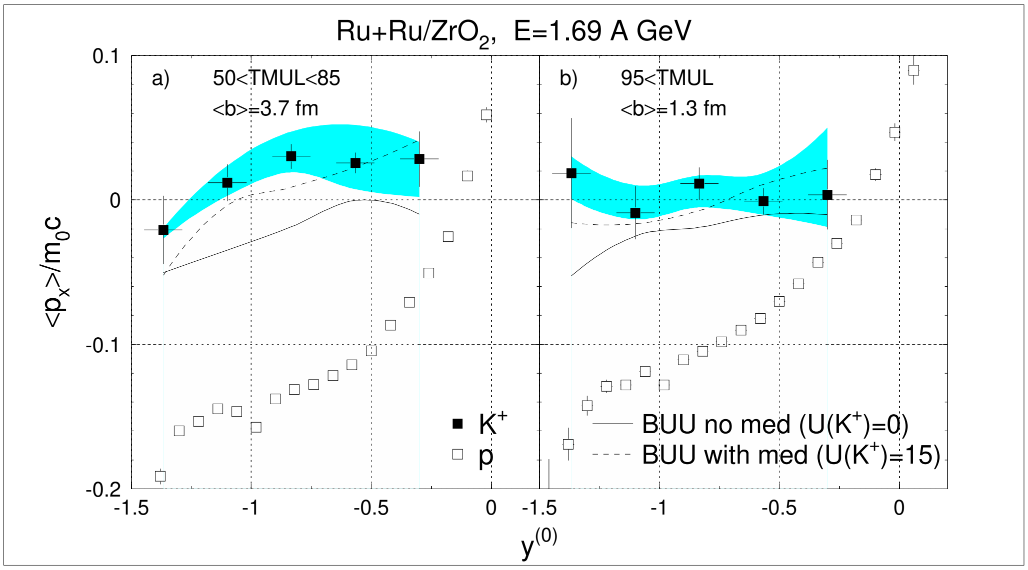

Figure 7.2: *Directed side-flow pattern of K^+ mesons (full symbols) and protons (open symbols) in centralmost (b) and less central (a) Ru+Ru and Ru+ZrO$_2$ collisions. The statistics of both experiments are combined in the case of the K^+ meson flow. The lines represent the predictions of the RBUU transport model with bare K^+ meson mass (solid lines) and with in-medium modifications of kaons (dashed lines) [81]. The RBUU events are selected with respect to centrality and filtered with condition 6.9, which describes the detector acceptance.*

produced together in the elementary processes NN→$K^+\Lambda$N. The observed difference between the flow patterns of both strange-particle species suggests that, during the propagation, K^+ mesons feel additional repulsion from the regions of high baryonic density. This extra repulsion is not due to the Coulomb potential. In [82], the flow patterns of K^+ and K^0_s mesons were compared for the Ni+Ni system at 1.93 A GeV and for the Ru+Ru/ZrO$_2$ system at 1.69 A GeV beam kinetic energy. It was shown that, within the accuracy of the measurements, the flow patterns of both neutral and charged kaons are the same. This means that, although K^0_s mesons are neutral, they are repelled by the baryonic matter as much as K^+ mesons are. Predictions based on transport model calculations also find that the observed K^+ meson flow signal can not be explained as an effect of the Coulomb repulsion [83].

7.3 Comparison to predictions of the RBUU transport model

The lines in Figure 7.2 show the K^+ meson flow pattern predicted by the RBUU transport model [81] for centralmost (b<2 fm) and less central (3<b<4 fm) Ru+Ru collisions at 1.69 A GeV beam kinetic energy. The impact parameter ranges are chosen in order to achieve the best match to the experimental centrality selection (cf. Table 3.1). The results of the model calculations are filtered with the conditions 6.9, which describes the detector acceptance.

Results of the two versions of the model are shown. The solid lines represent the version with bare K^+ meson mass. The dashed lines show the results of the model with the in-medium modifications of kaons. As said before, the change of the effective mass ($m^*_{K^+}$) is parametrized in a way that leads to a 15 MeV increase of $m^*_{K^+}$ at ρ_0.

It can be noticed that the model with bare K^+ meson mass overpredicts the kaon flow. It predicts as much flow in the centralmost as in the less central collisions. When the in-medium modifications of kaons are included, the model predicts less flow. Clearly, the repulsive effective K^+N potential additionally deflects K^+ mesons away from regions of high baryonic density, and changes the direction of their flow. Also the anti-flow signal observed in the less central collisions is reproduced, although the magnitude of the signal may be underpredicted. However, the differences between the predictions of the two versions of the model and, hence, the sensitivity of the considered observable to in-medium modifications of kaons is comparable to the uncertainties of the experimental results.

7.4 Dependence of the K^+ meson flow on transverse momentum

A more detailed analysis of the relation between $<p_x>/p_t$ and the transverse momenta of K^+ mesons was reported in [76]. Figure 7.3 shows the values of $<p_x>/p_t$ as a function of p_t for K^+ mesons measured in a limited range of normalized rapidity $-1.2<y^{(0)}<-0.65$. This particular range in $y^{(0)}$ was chosen because it assures the largest geometrical acceptance in the transverse direction (cf. Figure 6.1). This has the advantage that the extracted signal is not biased by the detector acceptance. Two event classes of distinguished centralities were selected, however, with slightly different conditions from those considered before. Central collisions were selected with a 52<PMUL condition, whereas the semi-central collisions with the condition 40<PMUL<50. The statistics of both Ru+Ru and Ru+ZrO_2 experiments were combined.

The results shown in Figure 7.3 are corrected in order to account for the uncertainty of the reaction-plane reconstruction, for the decay of K^+ mesons on the way to the Barrel, and for the loss of particles in the high track-density regions. The latter effect was revealed with the help of the Monte Carlo simulations, in which the full detector response was modelled with the GEANT simulation package. The appropriate corrections were estimated to be in the order of -0.04 [76].

It can be noticed that the values of $<p_x>/p_t$ increase with decreasing p_t in the case of both considered event categories. This pronounced dependence, when integrated over the measured p_t range, leads, on the one hand, to the vanishing (zero) flow signal in the central collisions shown in Figure 7.2b, and, on the other hand, gives

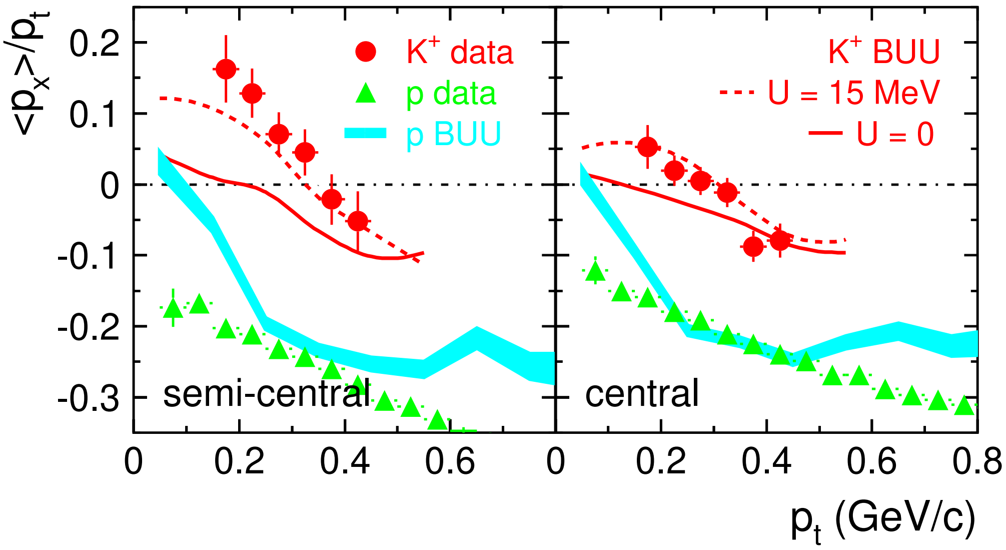

Figure 7.3: *The dependence of* $<p_x>/p_t$ *on the transverse momentum for* K^+ *mesons and protons measured within a limited range of the normalized rapidity* $-1.2<y^{(0)}<-0.65$. *The statistics of central (right) and semi-central (left) collisions of the Ru+Ru and Ru+*ZrO_2 *experiments are combined. The predictions of the RBUU transport model with bare kaon mass (solid lines) and with in-medium modifications of kaons (dashed lines) are compared to the data. The experimental results on proton flow are depicted by triangles. The predictions of the RBUU model on proton flow are shown with grey shaded bands, which illustrate the statistical uncertainty of the predictions. The plot is adapted from [76].*

the anti-flow signal in the less central collisions as illustrated in Figure 7.2a. It is clear that mostly low-p_t kaons contribute to the average values of $<p_x>/m_0c$ shown in Figure 7.2.

The lines in Figure 7.3 represent the predictions of the RBUU transport model. As before, results of the two versions of the model are shown : with bare kaon mass and with in-medium modifications of K^+N potential, leading to a 15 MeV increase of the effective kaon mass at ρ_0. The centralmost events are selected with the condition b<4 fm, the semi-central events are selected by requiring 3<b<5 fm. This corresponds roughly to the experimental centrality selection. The dependence of the K^+ meson flow pattern on the transverse momentum reveals more pronounced differences between the two model predictions. The distinction between the predictions is good especially at low p_t, because low-p_t kaons stay longer in the dense medium. The modifications of the K^+N potential, which introduce additional repulsion, are clearly needed in order to reproduce the experimental results, especially the anti-flow signal at low p_t observed in semi-central collisions.

Chapter 8

K^- meson phase-space distribution

In-medium effects are thought to act in opposite ways on K^+ and K^- mesons. They are also expected to be much more pronounced for K^- mesons. In this chapter, the results on K^- mesons in the Ru+Ru and Ru+ZrO_2 experiments will be reported. The final-state momentum-space distributions of K^+ and K^- mesons will be compared.

As before, only the central collisions selected by the medium-bias trigger condition and other requirements described in Chapter 3 are considered. The selected event samples correspond to the centralmost $\Delta\sigma \simeq 580$ mb of the total geometrical cross section (cf. Table 3.1).

8.1 K^- meson identification

The method of K^- meson identification is similar to that of K^+ mesons. The information on particle momentum and specific energy loss, delivered by the CDC, is combined with the information about the velocity, deduced from the measurements of TOF by the Barrel.

Figure 8.1a shows a limited range around the kaon mass, m_K=0.494 GeV/c^2, of the two-dimensional mass distribution $Mass_{CDC}$ versus $Mass_{Barrel}$. Only negatively charged particles of momenta lower than 0.32 GeV/c are included. Particle yields measured in both Ru+Ru and Ru+ZrO_2 experiments are combined. A peak from K^- mesons is visible at around mass of 0.5 GeV/c^2.

In Figure 8.1b the same distribution is shown, but the scatter-plot representation is chosen. The centroid of the K^- meson peak its shifted from its nominal position at $Mass_{CDC}$=$Mass_{Barrel}$=0.494 GeV/c^2. The origin of the shift as well as its implications for the results on K^- mesons will be discussed further in the following part of this section. In panels (c) and (d) of Figure 8.1 the shift of the centroid of the K^- meson peak is demonstrated for each of the derived quanti-

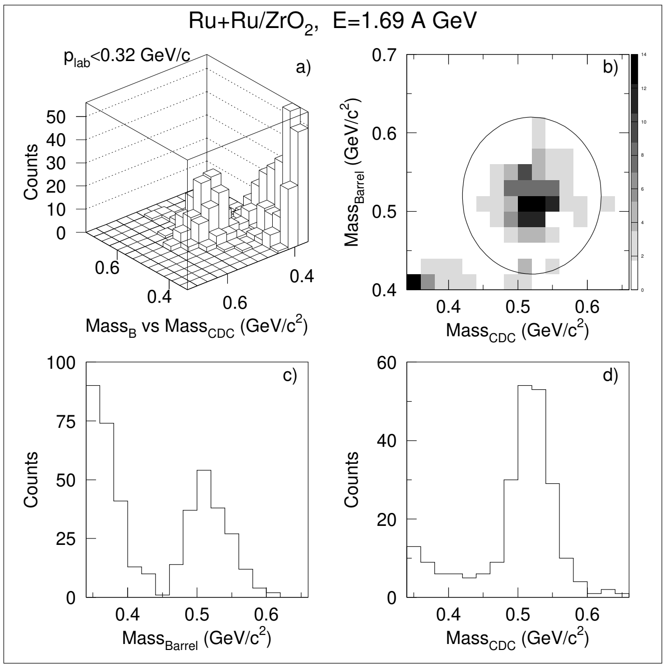

Figure 8.1: *(a) A limited range around the kaon mass,* m_K*=0.494 GeV/c*^{2}*, of the mass distribution for negatively charged particles with momenta lower than 0.3 GeV/c. Particle yields measured in central Ru+Ru and Ru+ZrO*$_2$ *collisions are added. (b) Same as (a) but a scatter-plot representation is chosen in order to demonstrate the shift of the centroid of the K*$^-$ *meson peak. (c,d) Projections of the matrix from panel (b) onto the two mass axes,* $Mass_{Barrel}$ *and* $Mass_{CDC}$.

ties, $Mass_{CDC}$ and $Mass_{Barrel}$, separately. It can be noticed that the peak is displaced by about the same amount in $Mass_{CDC}$ and $Mass_{Barrel}$. It is centered at roughly $Mass_{CDC}$=0.515 GeV/c^2 and $Mass_{Barrel}$=0.515 GeV/c^2, which corresponds to about 4% relative shift with respect to the kaon mass.

Because of the shift of the K$^-$ peak, the identification condition which is imposed on the mass parameters, $Mass_{CDC}$ and $Mass_{Barrel}$, has to be modified. As indicated by the the circle in Figure 8.1b, K$^-$ mesons can be selected with the condition

$$\left(\frac{Mass_{CDC} - 0.515\ \mathrm{GeV/c^2}}{0.1\ \mathrm{GeV/c^2}}\right)^2 + \left(\frac{Mass_{Barrel} - 0.515\ \mathrm{GeV/c^2}}{0.1\ \mathrm{GeV/c^2}}\right)^2 < 1\ , \qquad (8.1)$$

instead of requirement 5.3, used for K$^+$ meson identification. Such a change of the identification condition can systematically modify the extracted results. Although this modification turned out to be small, it will always be accounted for in the systematic errors quoted in the following part of this chapter.

It is not quite clear why the centroid of the K$^-$ meson peak is systematically shifted from its nominal position in the mass distribution. One possible explanation is that the measured momenta of particles were systematically too high. This would be very unfortunate because it would systematically distort the extracted momentum-space distribution of K$^-$ mesons. The effect can be, however, accounted for by subtracting 4% from the measured K$^-$ meson momenta. The result of such a modification will also always be included in the systematic errors of the results presented in the following part of this chapter.

The last considered contribution to the systematic errors originates, as in the case of K$^+$ mesons, from the change of the identification conditions from 5.13 to 5.14.

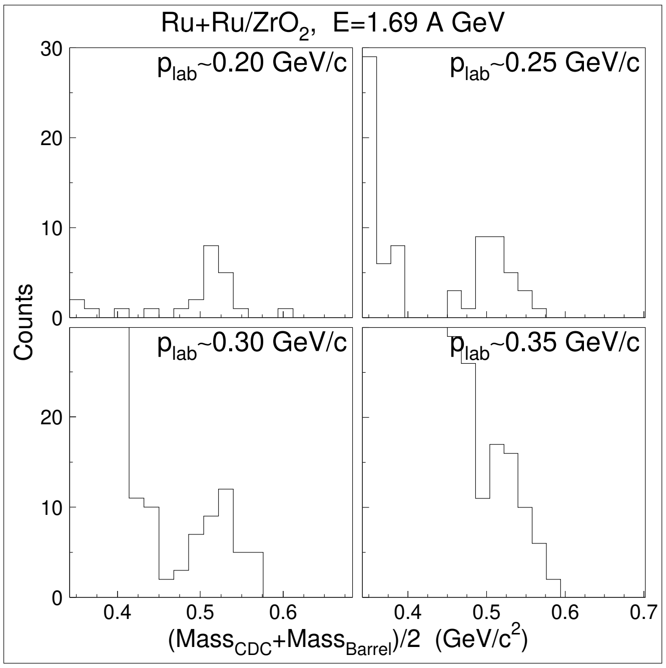

Figure 8.2: *A limited range around the kaon mass of the mass distributions for negatively charged particles with different momenta. Particle yields are shown as a function of the quantity ($Mass_{Barrel}$+$Mass_{CDC}$)/2.*

Also similarly to the K$^+$ meson case, pions are the main source of background contamination in the K$^-$ meson yield. The main difference, which makes the identification of K$^-$ mesons more difficult, is that the ratio of the K$^-$ meson yield to the π^- meson yield is two orders of magnitude smaller than that of their positively charged counterparts. Consequently, the background contamination in the K$^-$ meson yield, coming from the π^- mesons, increases very rapidly with momentum.

Subsequent panels of Figure 8.2 show a limited range around the kaon mass of the mass distributions obtained for negatively charged particles with different momenta (indicated in figure captions). Particle yields are shown as a function of the quantity $(Mass_{CDC}+Mass_{Barrel})/2$. Only particles for which the difference $|Mass_{CDC}\text{-}Mass_{Barrel}|$ is smaller than 0.05 GeV/c^2 are included. Thus, the plotted spectra are equivalent to the slices around the diagonal line of the corresponding two-dimensional mass distributions, $Mass_{CDC}$ versus $Mass_{Barrel}$[1]. This complicated representation is necessary to demonstrate the existence of K$^-$ meson peaks in the mass distributions of particles with different momenta. Because of very low statistics, the peaks from K$^-$ mesons are not very well pronounced when two-dimensional mass distributions are plotted.

It can be noticed that the K$^-$ meson peaks remain practically background-free up to momentum of about 0.3 GeV/c. On the other hand, the background contamination is already very big (>50%) at momentum around 0.35 GeV/c. Detailed studies on the mass distributions such as those shown in Figure 8.2 revealed that the K$^-$ meson yield can be extracted without considering the background contamination if particles of momenta lower than 0.32 GeV/c are considered. Above this limit, the

---

[1] Similar distributions were considered in Section 5.5 when the method of determining the background content in the K$^+$ meson yields was discussed.

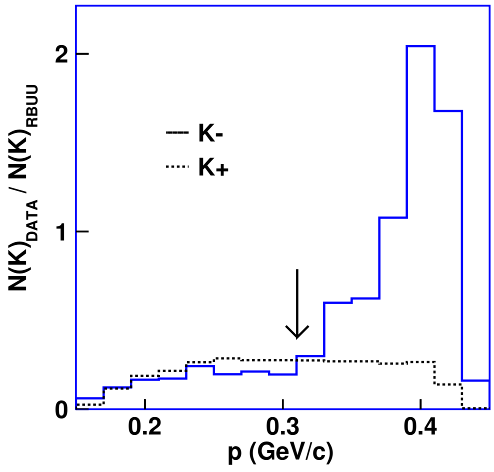

Figure 8.3: *The K^+ and K^- meson yields as a function of momentum. The yields are normalized to the predictions of the RBUU transport model. The scale on the ordinate is arbitrary. The arrow indicates the upper momentum limit p=0.32 GeV/c for the K^- meson identification.*

background content in the K^- meson yield, coming from the tail of π^- meson peak, becomes larger than 10%, and grows very rapidly with increasing momentum. Due to limited statistics, it is practically impossible to account for this contamination in the K^- meson yields at momenta higher than 0.32 GeV/c.

Another observation suggests that p=0.32 GeV/c is the upper momentum limit for the K^- meson identification. In Figure 8.3 the number of selected K^+ and K^- mesons is shown as a function of momentum. The yields are divided by the predictions of the RBUU transport model (the absolute normalization is arbitrary). It can be seen that, for momenta higher than 0.32 GeV/c, the number of selected K^- meson candidates exceeds drastically the model predictions, which is not the case for the K^- meson yield below this momentum limit and for the K^+ meson yields below and above this limit.

Unfortunately, applying more restrictive identification conditions, for instance the requirement 5.13 instead of 5.4, does not allow to extend the momentum range in which the K^- mesons can be identified. The peak from K^- mesons disappears in the mass distribution as soon as particle momenta exceed 0.32 GeV/c. Nevertheless, as in the case of K^+ mesons, the identification conditions are varied from 5.13 to 5.14 in order to estimate the systematic errors of the extracted results.

Altogether 142^{+7}_{-22}(syst) and 111^{+17}_{-10}(syst) K^- mesons were selected in the Ru+Ru and in the Ru+ZrO_2 experiments respectively. Taking into account the number of considered events (cf. Table 3.1), the quoted yields correspond to the average detection rates of $3.23 \pm 0.3(\text{stat})^{+0.16}_{-0.5}(\text{syst}) \cdot 10^{-5}$ and $3.2 \pm 0.3(\text{stat})^{+0.4}_{-0.4}(\text{syst}) \cdot 10^{-5}$ K^- mesons per central collision[2]. As in the case of K^+ meson, it can be concluded that (i) the difference between the targets does not affect the production of K^- mesons, and (ii) the K^- meson yields measured in both experiments can be combined in order to improve the statistical significance of the extracted results.

Within the fraction of the momentum space in which K^- mesons were identified

---

[2] Corrections due to the efficiency of the detection and the identification procedure are not applied here.

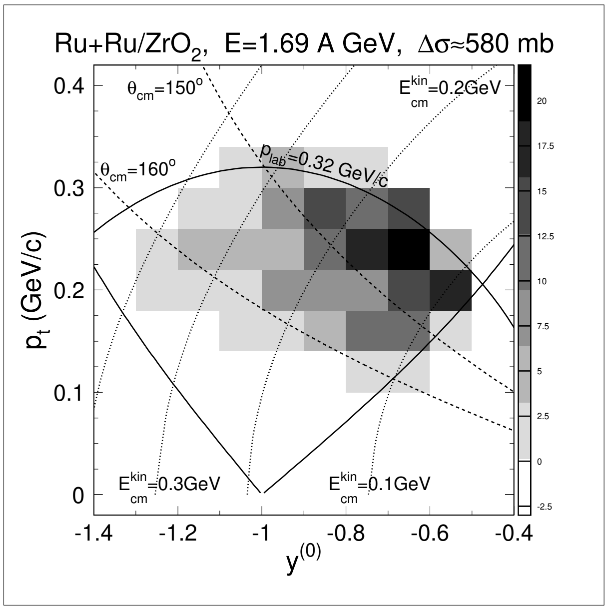

Figure 8.4: *The final-state momentum-space distribution of K^- mesons in central Ru+Ru and Ru+ZrO$_2$ collisions (the statistics of both experiments are combined). K^- meson yield is shown as a function of transverse momentum and rapidity. Solid lines represent the geometrical acceptance of the Barrel and the upper momentum limit p=0.32 GeV/c for the K^-meson identification. Dashed lines correspond to polar angles Θ_{cm}=150° and 160°. Dotted lines correspond to kinetic energies in the CM reference frame E^{kin}_{cm}=100,200,300 and 400 GeV.*

(p<0.32 GeV/c), altogether $7.0^{+0.4}_{-0.9}$(syst)$\cdot 10^3$ and $5.5^{+0.8}_{-0.7}$(syst)$\cdot 10^3$ K$^+$ mesons were selected in the Ru+Ru and Ru+ZrO$_2$ experiments respectively. These numbers are collected in Table 8.1.

System	# of K$^+$ mesons (p<0.32GeV/c)	# of K$^-$ mesons (p<0.32GeV/c)	# of K$^-$ mesons per event
^{96}Ru+^{96}Ru	$7.0^{+5}_{-9}\cdot 10^3$	142^{+7}_{-22}	$3.23^{+16}_{-50}\cdot 10^{-5}$
^{96}Ru+^{96}ZrO$_2$	$5.5^{+4}_{-7}\cdot 10^3$	111^{+17}_{-10}	$3.26^{+40}_{-40}\cdot 10^{-5}$

Table 8.1: *Statistics of $K^+$and K^-mesons in the Ru+Ru and Ru+ZrO$_2$experiments.*

Figure 8.4 shows the final-state momentum-space distribution of K$^-$ mesons measured in both experiments. The solid lines depict the geometrical acceptance of the detector and the upper momentum limit p=0.32 GeV/c for the K$^-$meson identification. The dashed lines are drawn for different polar angles, Θ_{cm}, which will be referred to in the next section. The dotted lines correspond to different kinetic energies, E^{kin}_{cm}, in the CM reference frame.

8.2 K$^-$ to K$^+$ meson yield ratio

The limited statistics of identified K$^-$ mesons (together around 250 in both Ru+Ru and Ru+ZrO$_2$ experiments) do not allow to perform a detailed analysis of their final-state momentum-space distribution. In principle, a kinetic-energy spectrum in a wide Θ_{cm} range could be extracted. The accuracy would be limited primarily by the uncertainty of the identification efficiency.

Therefore, in this work a more practical way of studying the K^- meson phase-space distribution is chosen. The K^- to K^+ meson yield ratio is studied. This offers several advantages. (i) The yield ratio can be extracted in the experimentally accessible fraction of the momentum-space, and the result can be interpreted without need of extrapolation to the not measured phase-space regions. (ii) The efficiency corrections, which contribute substantially to systematic errors, are to a large extent eliminated when the yield ratio is studied. In Section 5.4 it was shown that the efficiency of the identification procedure is the same for positively and negatively charged particles[3]. (iii) In-medium effects act in opposite ways on K^+ and K^- mesons, hence, the yield ratio should reveal them more clearly.

In Figure 8.5a the ratio of K^- to K^+ meson yields measured in the polar-angle range $150° < \Theta_{cm} < 160°$ is shown as a function of the kinetic energy. This particular range in the polar angle is chosen in order to assure that the result is not biased by the detector acceptance, and in order to provide the largest acceptance in E^{kin}_{cm} (cf. Figure 8.4). The yields of K^+ and K^- mesons are corrected in order to account for the decays of particles on the way to the Barrel, although this correction turns out to be negligible. The error bars correspond to the statistical uncertainties. The grey shaded band depicts the variation of the result due to the change of the identification conditions. Also included are the contributions to the systematic errors from (i) the possible 4% shift of the measured momenta of K^-mesons, and (ii) from the change of the identification condition 8.1, imposed on the mass parameters. The two latter sources of the systematic errors were discussed in detail in Section 8.1.

As shown in Figure 8.5a, the K^- to K^+ meson yields ratio is in the order of 1 to 3% in the considered range of kinetic energies. The ratio decreases with increasing E^{kin}_{cm}. On average K^- mesons have lower kinetic energies than K^+ mesons. It can be concluded that the kinetic-energy spectrum of K^- mesons is softer than that of K^+ mesons.

In Figure 8.5b the yield ratio is plotted as a function of the normalized rapidity. All identified K^- and K^+ mesons of momenta lower than 0.32 GeV/c are included. The result is biased by the detector acceptance, which changes in the considered rapidity range. The effect of the bias will be discussed further in Section 8.3. The result has, on the other hand, the biggest statistical significance since all the identified kaons are considered. It can be noticed that the yield ratio rises towards mid-rapidity. This suggest again that the K^- meson final-state momentum-space distribution is more compact than that of K^+ mesons.

At SIS energies, different K^+ and K^- meson final-state momentum-space distributions were observed also in the case of a lighter, Ni+Ni system at 1.93 A GeV [62, 84] and the C+C system at 1.8 A GeV beam kinetic energy [85]. The overall K^- to K^+ meson yield ratio was found to be in the order of 1 to 5%, and vary in

---

[3] It was observed that the efficiencies of the identification procedures for positively and negatively charged pions differ by about 10% when tracks of low hit multiplicity ($20 < NH < 30$) are included. The difference does not depend on momentum and is taken into account when the systematic errors are quoted in the following part of this chapter.

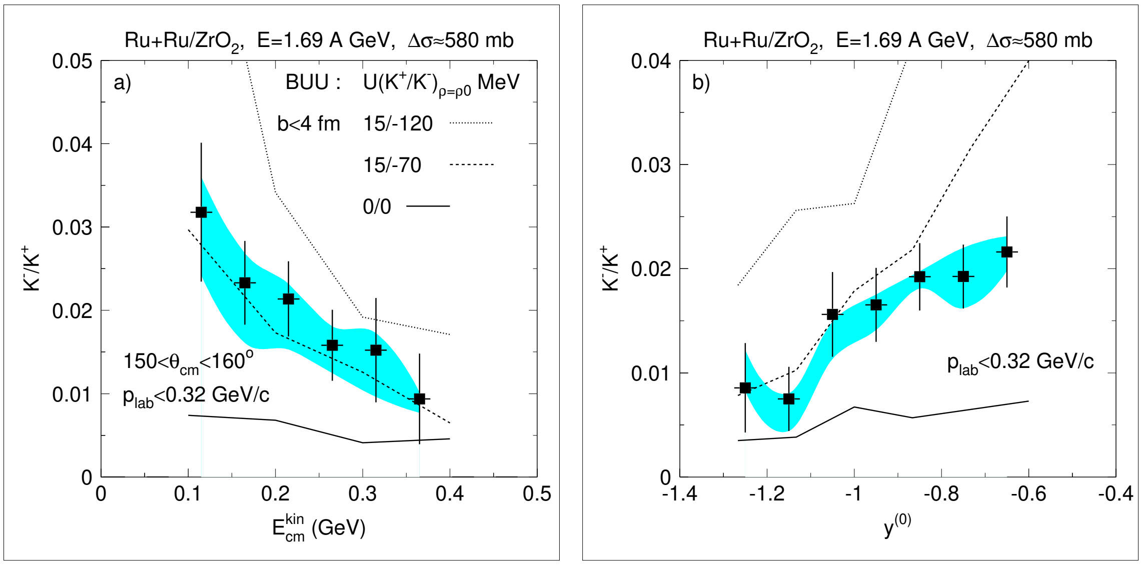

Figure 8.5: *The K^- to K^+ meson yield ratio in central Ru+Ru and Ru+ZrO$_2$ collisions (the statistics of both experiments are combined). Only particles of momenta lower than 0.32 GeV/c are included. The lines show the predictions of different versions of the RBUU transport model (see the next section for further discussion). (a) The ratio is plotted as a function of E^{kin}_{cm} for K^+ and K^- mesons measured in the polar-angle range $150^\circ < \Theta_{cm} < 160^\circ$. (b) The ratio is shown as a function of $y^{(0)}$ for all K^+ and K^- mesons measured in the experimentally accessible fraction of the momentum space illustrated in Figure 8.4.*

the measured fraction of the momentum space, which is well in line with the results reported in this work.

Similar observations were made at AGS energies. The K^- to K^+ meson yield ratio was measured for the Au+Au system at 11.6 A GeV beam kinetic energy, and was found to grow close to mid-rapidity [86]. Discrepancies between those data and the predictions of the RQMD transport model were interpreted as a signal of multi-body hadronic collisions. It will certainly be interesting to see whether this phenomenon can be separated from in-medium effects on kaons discussed in this work.

8.3 Comparison to predictions of the RBUU transport model

The lines in Figure 8.5 show the K^- to K^+ meson yield ratio predicted by the RBUU model [81] for the Ru+Ru system at 1.69 A GeV beam kinetic energy. In order to match the experimental centrality selection (cf. Table 3.1), only events of $b<4$ fm are included. In order to facilitate the comparison to the experimental data, the results of the simulation are filtered with a condition describing the detector acceptance. In the E^{kin}_{cm} range in which the comparison is made, the E^{kin}_{cm}-dependence of the ratio is not biased by the geometrical acceptance. The distortion of the $y^{(0)}$-dependence of the ratio due to the geometrical bias will be discussed in the following part of this section.

Results of three different versions of the model are shown in Figure 8.5. The full lines represent the version with bare kaon masses. Within the statistical uncertainties of the model predictions, the ratio is constant in the measured fraction of the momentum-space. This is in contradiction to the trends found in the experiment. Also the overall K^- meson yield relative to that of K^+ mesons is greatly underpredicted. Other lines in Figure 8.5 depict the predictions of the RBUU model with different strength of the in-medium effective KN potentials, as described in detail in Appendix A.4. The dotted lines represent the version with strong in-medium effects on K^- mesons. The parametrization of the effective K^- meson mass ($m^*_{K^-}$) is such that it leads to a 120 MeV reduction of $m^*_{K^-}$ at the normal nuclear matter density. The dashed lines depict the prediction of the model with less attraction for K^- mesons. The parametrization which is used leads to a 70 MeV reduction of $m^*_{K^-}$ at ρ_0. In both latter cases, the change of the effective K^+ meson mass is parametrized in a way that results in a 15 MeV increase of $m^*_{K^+}$ at ρ_0.

One observes that, when in-medium modifications of kaons are taken into account, the overall yield ratio increases. This is due, on the one hand, to a moderate increase of the threshold energy for the production of K^+ mesons and, on the other hand, to a large decrease of the threshold energy for the K^- meson production. The overall yield ratio changes accordingly to the magnitude of the modifications of $m^*_{K^-}$ which are introduced. The larger the reduction of the effective K^- meson mass is, the more the yield ratio grows with respect to the model predictions with bare kaon masses.

Moreover, when the in-medium effects on kaons are considered, K^+ mesons are repelled from the central, dense zone of the collision, by the gradient of the repulsive effective potential. Contrary, K^- mesons are decelerated during the propagation by the attractive in-medium potential, of which the gradient points towards the central collision-zone. In this way, the momentum-space distribution of K^+ mesons gets broader and that of K^- mesons narrower. Therefore, the RBUU model with in-medium effects on kaons predicts that the K^- to K^+ meson yield ratio rises at low kinetic energies and towards mid-rapidity. The effect is in quantitative agreement with the trends observed in the experiment. Similar conclusions were drawn by other theoretical groups [87].

With certain caution one may even conclude about the strength of the in-medium modifications of kaons. It is clear that the version of the RBUU model with stronger K^- meson attraction overpredicts the observed effect, whereas when a moderate change of K^- meson effective mass is considered, the correspondence between the model predictions and the experimental results is very good. Of course, similar effects would be observed when one allowed for stronger in-medium modifications of the K^+ meson effective mass. Here, however, less freedom is available. First of all, a large change of $m^*_{K^+}$ is not expected from the theoretical point of view (cf. Figure A.1). Secondly, measurements on K^+ mesons reported in the previous chapters of this work do not support such large in-medium effects on K^+ mesons. The analysis of the directed side-flow pattern of K^+ mesons suggested a moderate (about 15 MeV) increase of $m^*_{K^+}$ at the normal nuclear matter density. The final-state momentum-space distribution and the production rates of K^+ mesons were found to be compatible with the model predictions with bare K^+ meson mass.

The $y^{(0)}$-dependence of the yield ratio shown in Figure 8.5 is biased by the detector acceptance, which is not uniform over the considered rapidity range (cf. Figure 8.4 or 6.1, and notice that at around target-rapidity the acceptance is largest in the transverse direction). The distortion due to the geometrical bias is expected to be the larger, the more the yield ratio grows with decreasing transverse momentum. The amount of the distortion was tested on the results of the transport model. This is illustrated in Figure 8.6 in the case of the version with moderate in-medium effects on kaons. The dashed line represents the model predictions filtered with a condition which describes the detector acceptance. It is exactly the line which is plotted in Figure 8.5. The solid line shows the model results not biased by the geometrical acceptance[4]. It can be noticed that the detector acceptance influences systematically the $y^{(0)}$-dependence of the ratio. The yield ratio rises more steeply towards mid-rapidity when the model predictions are subject to the geometrical bias.

It is expected that a similar effect is present in the case of the experimental results. The ratio increases more steeply towards mid-rapidity when extracted from the measured fraction of the momentum space (the data shown in Figure 8.5), than it actually would follow from the not biased K^+ and K^- meson distributions. However, taking into account the magnitude of the distortion on the model predictions, it is unlikely that the $y^{(0)}$-dependence of the ratio observed in the experiment is only due to the acceptance bias. Apart from that, a clear E^{kin}_{cm}-dependence of the ratio was observed.

8.4 Influence of the final-state interactions

It was shown in Section 8.2 that the K^- to K^+ meson yield ratio varies across the measured fraction of the momentum space. In Section 8.3, the experimental observations were compared to the predictions of the RBUU transport model. The comparison revealed that the results can be well understood if the in-medium modifications of kaon effective masses are assumed. Before any conclusion about in-medium effects on kaons can be drawn, other, simpler explanations of the experimental results should be considered.

First of all, one may try to explain the variation of the yield ratio across the momentum space by the following kinematical consideration. From all elementary, NN processes which lead to the production of K^+ mesons in a first-chance collision,

---

[4] Accidentally, the model predictions fit the data even better when the acceptance filter is not applied.

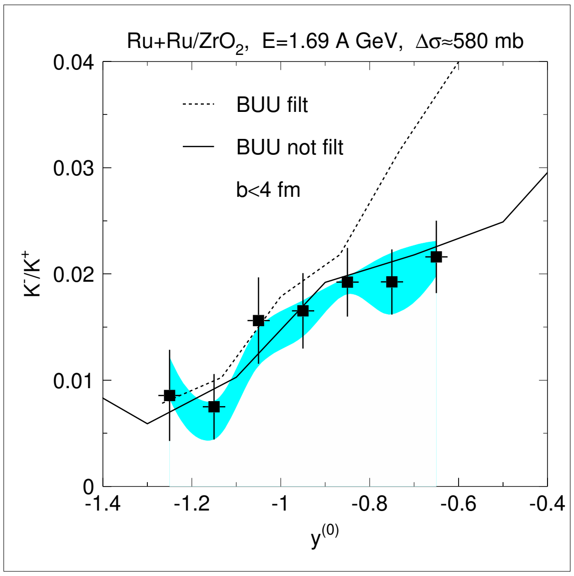

Figure 8.6: *The effect of the geometrical bias on the $y^{(0)}$-dependence of the K^- to K^+ mesons yield ratio. The lines depict the predictions of the RBUU transport model with moderate in-medium effects on kaons. The solid line shows the result not filtered with a condition which describes the detector acceptance. The dashed line represents the result with the acceptance filter applied. The measured yield ratio is depicted by symbols.*

the reaction

$$\mathrm{NN} \to \mathrm{N\Lambda K^+} \tag{8.2}$$

has the lowest threshold energy of $E_{thr}{=}-m_N{+}m_\Lambda{+}m_K{\simeq}671$ MeV/c^2. An analogous process for the production of K$^-$ mesons is

$$\mathrm{NN} \to \mathrm{NNK^+K^-} \ . \tag{8.3}$$

Its threshold energy of $E_{thr}{=}2{\cdot}m_K{\simeq}988$ MeV/c^2 is considerably higher than that of the process 8.2. Assuming that the above processes contribute substantially to the total K$^+$ and K$^-$ meson production rates, one may argue that by definition the momentum space available for K$^-$ mesons is narrower than that of K$^+$ mesons. Consequently, the measured K$^-$ meson final-state momentum-space distribution should be narrower than that of K$^+$ mesons.

An indirect argument, based on model predictions, can be given against the above explanation. The solid lines in Figure 8.5 show the yield ratio predicted by the RBUU model without in-medium effects on kaons. Certainly, when the production of K$^+$ and K$^-$ mesons is simulated in the model, particles populate the momentum space according to the energy available above the production threshold energies. Despite this, the yield ratio predicted by the model does not vary substantially across the momentum space. It is because of the two following reasons.

- According to model predictions, the dominant K$^+$ and K$^-$ meson production channels go via many-step processes, and involve baryon resonances, hyperons and pions (cf. Appendix A.4). The threshold energies of these processes are much lower than those of the processes 8.2 and 8.3.

- During the propagation, K$^+$ and K$^-$ mesons are furthermore scattered while the system approaches the thermal equilibrium, which tends to equalize their final-state momentum-space distributions.

One may also try to explain the E_{cm}^{kin}- and $y^{(0)}$-dependences of the yield ratio by the influence of electromagnetic interactions. The problem has to be investigated because K^+ mesons are repelled by the net positive charge of the colliding ions, while K^- mesons are decelerated in the electric field of the positive charge. Consequently, the final-state momentum-space distribution of K^- mesons could be narrower than that of K^+ mesons. In the RBUU model, the electromagnetic interactions are taken into account only in a limited time span, from the beginning of the collision up to freeze-out time. The influence of these interactions turned out to be not sufficient to explain the experimental results when bare kaon masses were assumed. However, in central heavy-ion collision, a system of a very large net positive electric charge is formed. The Coulomb field of this charge may influence the propagation of particles at distances which are larger than a typical freeze-out radius. Therefore, it remains to be checked whether or not the final-state momentum-space distributions of kaons can be substantially modified due to the electromagnetic interactions after the freeze-out.

In [88] and [89], the influence of the electromagnetic field on particle spectra was studied in detail by means of analytical formulas as well as numerical simulations. It was shown, for example, that the yield ratio of π^- to π^+ mesons in Au+Au collisions at 1 A GeV bombarding energy increases more than by a factor of two at low kinetic energies due to the final-state electromagnetic interactions.

The analytical formulas can be used in a static case, i.e., when a static electric field is generated by a charge which is at rest. A uniformly dense sphere is the most simple assumption about the charge distribution. In such a simplified case, it is straightforward to modify the initial energy spectra of particles and account for Coulomb repulsion/attraction by adding potential energy V_C (in MeV) to initial particle energies

$$V_C = \begin{cases} \pm 1.44 \cdot Z_{tot}/r & \text{for } r > R_f \\ \pm 1.44 \cdot Z_{tot}(3R_f^2 - r^2)/(2R_f^3) & \text{for } r < R_f \;. \end{cases} \tag{8.4}$$

Here, Z_{tot} (in units of the elementary charge) and R_f (in fm) are the total charge and the radius of the charged sphere respectively, whereas r (in fm) is the initial distance of a particle to the center of the sphere. The sign is positive for positively charged particles and the opposite for negative particles[5].

A more realistic description can, for example, include expansion of the system with a velocity β_{flow}. In such a case, the influence of the electromagnetic field on charged particle spectra can be investigated only by numerical simulations. In this work several assumptions are made in order to perform such simulations.

- Initially, the net positive charge is distributed uniformly in a sphere of a radius R_f, which afterwards expands radially with velocity β_{flow}[6].

---

[5] Only particles of charge $Q=\pm 1$ are considered.

[6] At SIS energies the system is thought to expand radially. At AGS energies, on the other hand, an elongated shape and a longitudinal expansion of the system would be a more realistic assumption [27].

- Initially, the charged particles (K^+ and K^- mesons) are distributed uniformly in the same sphere.

- The initial momentum-space distributions of K^+ and K^- mesons are also the same. Mesons are emitted isotropically from a thermally-equilibrated source of temperature T, which expands radially with flow velocity β^K_{fl}, i.e., the distributions of K^+ and K^- mesons are described by formula A.4. The initial velocity of a particle is a relativistic sum of the velocity of the thermal motion and the velocity of the collective radial expansion at the initial position.

- Only the electric part of the electromagnetic interaction (the Coulomb force) is considered. The influence of the magnetic field is neglected as it scales with particle velocities. Also the retardation effects are neglected, as they are thought to play a minor role at SIS energies [89].

The simulations were performed according to the second-order, Runge-Kutta method [90]. The propagation of particles was followed in 0.1 fm/c time steps to a distance of 200 fm/c. At this distance the Coulomb potential is in the order of $V_C \simeq 1$ MeV as compared to $V_C \simeq 20$ MeV at $r \simeq 8$ fm. The correctness of the simulations was established and checked by various means. It was tested that the simulations give the same results as the analytical formulas, appropriate for a static case, when β_{flow} was set to 0. Secondly, the values of the parameters were set to those quoted in [88], and the results were found to correspond very well to those given therein. This is demonstrated in Figure 8.7, which shows the kinetic-energy spectra of K^+ and K^- mesons after propagation in the Coulomb field of the system described above, with parameters: Z=158, R_f=8 fm, T=130 MeV and β_{flow}=0.6 or 0.

The histogram in Figure 8.8a shows the initial kinetic energy spectra of 100.000 K^+ and K^- mesons, which were used as the input to the simulations performed in order to test the influence of the Coulomb field on the K^- to K^+ meson yield ratio studied in this work. Within the numerical noise, the initial spectra are compatible with the thermal distribution according to formula A.4, with parameters T=82 MeV and β^K_{fl}=0.37. The parameters were chosen as those fitting reasonably well the freeze-out conditions extracted from the kinetic-energy spectra of pions, protons and deuterons (cf. Chapter 4).

The solid histograms in panels (b) and (c) of Figure 8.8 show the kinetic-energy spectra of mesons after propagation in the electric field of the system described above, with parameters: Z_{tot}=88, R_f=8 fm, β_{flow}=0.37. In addition, the dotted lines depict the results obtained for a static case, with β_{flow}=0. It can be noticed that the results for the static case differ considerably from those of dynamical modelling only at kinetic energies lower than 100 MeV, which in any case were not accessible in the experiment.

The parameters of the simulations were changed within a reasonable range in order to test the influence of the initial conditions on the resulting yield ratios. No significant differences were observed when the temperature, T, was varied from 80 to 130

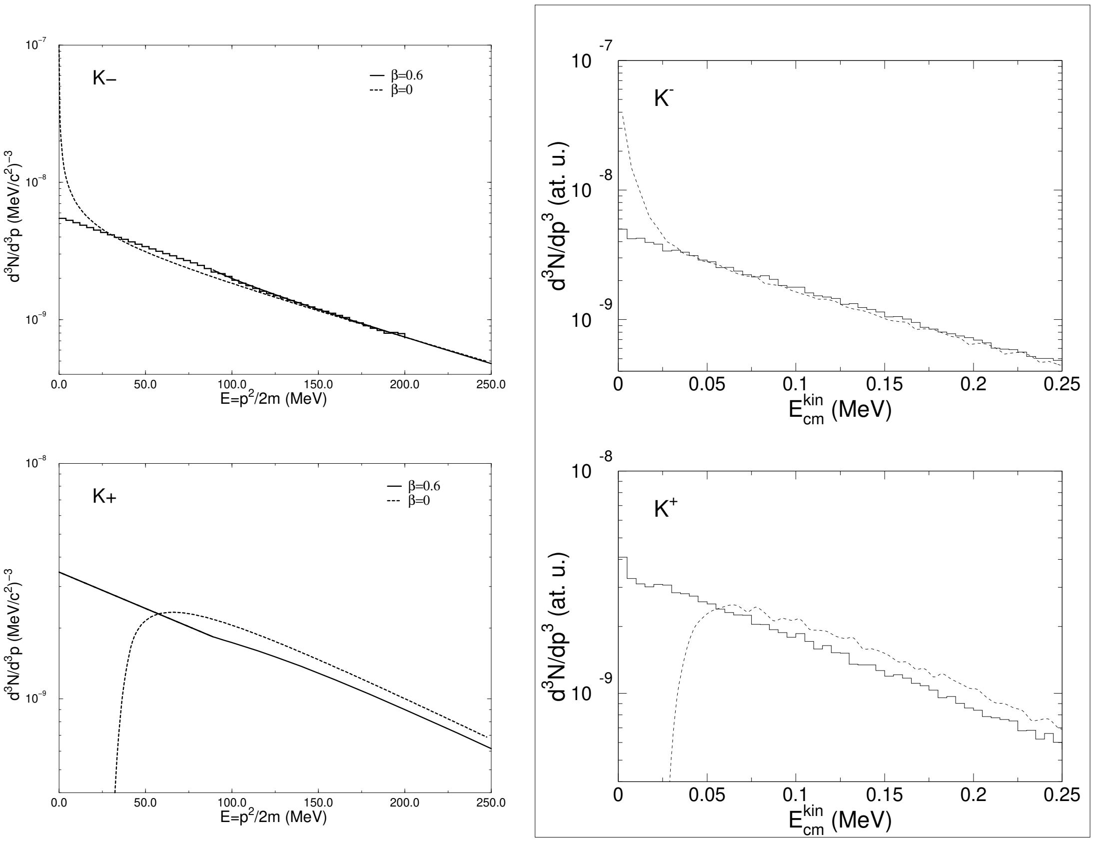

Figure 8.7: *Simulated kinetic-energy spectra of K^- (up) and K^+ (down) mesons after propagation in the Coulomb field. See the text for the description of the initial conditions and the parameters of the simulations. The dashed lines show the results for a static case, with β_{flow}=0. Left – results quoted in [88]. Right – results of this work.*

MeV. Also the change of the flow velocities, β_{flow} and β^K_{fl}, from 0 to 0.4 turned out to have no observable effect on the yield ratio. The results changed moderately when Z_{tot} and R_f were varied. Two extreme cases were considered. (i) Strong Coulomb potential, with parameters Z_{tot}=88 (the total charge of colliding ions) and R_f=6.5 fm, corresponding to the freeze-out density of $2{\cdot}\rho_0$. (ii) Weak Coulomb force, with Z_{tot}=60 and R_f=12 fm, corresponding to the freeze-out density of $1/2{\cdot}\rho_0$.

The horizontal dark-grey shaded band in Figure 8.9 represents the the K^- to K^+ meson yield ratio which results from the simulations. The overall normalization was chosen arbitrarily in order to facilitate the comparison to the experimental data. It can be noticed that the yield ratio increases not more than 20% at the lowest kinetic energies accessible in the experiment. The biggest effect is of course observed in the case of parameters Z_{tot}=88 and R_f=6.5 which lead to the strong Coulomb potential. It can be concluded that, according to the results of the simulations, the differences between the measured K^+ and K^- meson momentum-space distributions can not be explained as an effect of the final-state electromagnetic interactions.

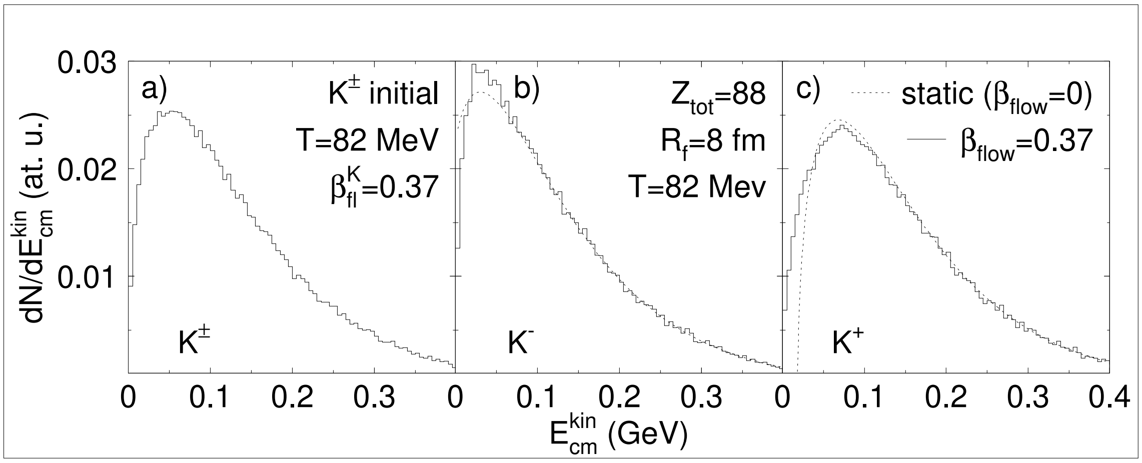

Figure 8.8: *Kinetic-energy spectra of K^- and K^+ mesons from the simulations performed in order to investigate the influence of the Coulomb field on the meson yield ratio in the Ru+Ru/ZrO$_2$ experiment. See the text for the description of the initial conditions and the parameters of the simulations. The initial meson spectra are shown in panel (a). The spectra of K^- and K^+ mesons after the propagation in the Coulomb field are depicted by the solid histograms in panels (b) and (c) respectively. The dotted lines are drawn according to the analytical formula 8.4, adequate for a static case when the radial expansion of the system is neglected (β_{flow} set to 0).*

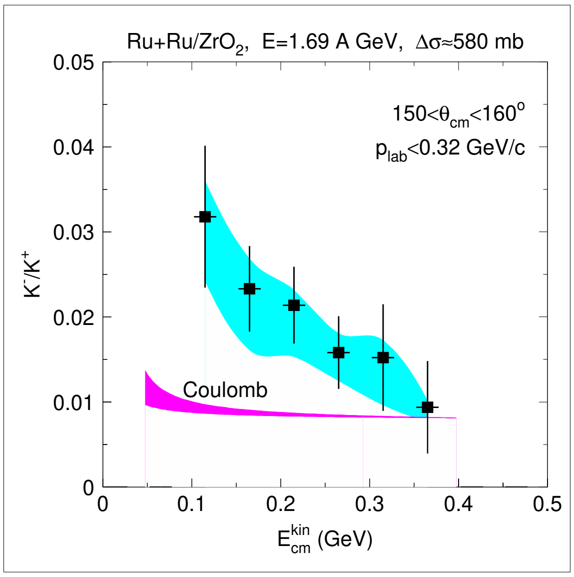

Figure 8.9: *The K^- to K^+ meson yield ratio in central Ru+Ru and Ru+ZrO$_2$ collisions in the polar-angle range 150°<Θ_{cm}<160°. The points depict the experimental data. The horizontal dark-grey shaded band represents the results of the numerical simulation performed in order to estimate the influence of the Coulomb field on the meson yield ratio. See the text for the description of the initial conditions and the parameters of the simulations.*

Chapter 9

Summary

Recently there has been considerable effort, both experimentally and theoretically, to investigate the production of kaons in heavy-ion collisions at bombarding energies around 1-2 GeV per nucleon. At these beam energies, kaons are most likely produced in the early stage and in the central region of the collision, where densities of up to 3 times the normal nuclear matter density and temperatures in the order of 100 MeV can be reached The production rate can be influenced not only by the surrounding medium (e.g., its density) or the properties of the nucleons and their resonances, but also by possible in-medium modifications of the kaon properties themselves.

A variety of theoretical approaches predict consistently that the effective mass of kaons grows slightly with increasing baryon density, while the mass of antikaons is expected to drop substantially. This phenomenon could lead to the formation of a kaon condensate in a dense hadronic environment, which in turn would effect the nuclear equation of state, and have consequences for the physics of neutron stars. The modifications of the properties of kaons in a hadronic medium might originate from the partial restoration of the chiral symmetry of QCD.

Experimentally, the question of in-medium modifications of kaons was addressed at low baryonic densities with studies on kaonic atoms and kaon-nucleus scattering. At higher densities, the in-medium effects can be investigated only by means of heavy ion collisions. Here, the enhanced K^- meson production and the directed side-flow pattern of K^+mesons were interpreted as a signature for changes of kaon effective masses and KN interactions.

The main goal of this work was to present the experimental data on the production of K^+ and K^- mesons in ^{96}Ru+^{96}Ru and ^{96}Ru+^{96}ZrO$_2$ collisions at 1.69 A GeV beam kinetic energy. The experiments were performed in 1996, with the FOPI detector system, installed on the beam of SIS at GSI/Darmstadt. The question of in-medium modifications of meson properties was addressed by comparing the experimental results to the predictions of the RBUU transport model.

The momentum-space distribution of K^+ mesons was reconstructed from its measured fraction around the target-rapidity. The reconstructed distribution was shown to be not fully compatible with an isotropic emission pattern. Nonetheless, the results suggested that thermal equilibrium between K^+ mesons and the surrounding matter is approached. The K^+ meson production rate per participating nucleon was found to grow with collision centrality. The total K^+ meson production probability was estimated. The result did not support a hypothesis about the chemical equilibrium of the strangeness. Due to limited accuracy of these measurements, it was not possible to draw definite conclusions about the in-medium effects on kaons by comparing the data to the predictions of the RBUU transport model.

The directed side-flow pattern of K^+ mesons was studied in collisions of different centralities. In less central collisions, K^+ mesons were found to flow in the direction opposite to protons. In addition, the dependence of the K^+ meson flow on the transverse momentum was shown. Both integrated and differential signals exhibited potentially high sensitivity to the in-medium effects on kaons. The experimental observations were reproduced by the RBUU transport model only if the in-medium modifications of kaons were considered.

More pronounced in-medium effects are expected for K^- mesons. The experimental results on K^- mesons were presented only relative to the measurements on K^+ mesons. The K^- to K^+ meson yield ratio was studied. The yield ratio turned out to be in the order of 1 to 3%, and vary in the measured fraction of the momentum space. The K^- meson momentum-space distribution was found to be more compact than that of K^+ mesons. The results could not be explained as an effect of the final-state Coulomb interactions. The observation was reproduced by the RBUU transport model only if the in-medium modifications of kaons were taken into account.

It can be concluded that the experimental evidence presented in this work clearly favours the presence of in-medium effects on kaons. The results can be best understood by assuming the in-medium modifications of kaon effective masses and/or KN interactions. The presented conclusions are model dependent, and based on the comparison of the data to the predictions of a particular transport model. However, predictions of other theoretical groups are in general in line with the results of the model considered in this work.

In the nearest future, the FOPI detector system will be upgraded. The data acquisition rate will be speed-up by a factor of ten, which will allow to reduce substantially the statistical uncertainties of the extracted results. Time-of-flight measurements, necessary for the identification of K^+ and K^- mesons, will be improved as well. Thanks to the installation of the Pestov Counters instead of a forward part of the Plastic Scintillator Barrel, the measured fraction of the momentum space will be extended to higher momenta and towards mid-rapidity.

With the new FOPI detector system, more accurate measurements on K^+ and K^- mesons, as well as on more exotic Φ mesons will be performed. This will hopefully allow to elucidate further the question of the in-medium modifications of hadron properties.

Appendix A

A.1 Bethe-Bloch formula

Charged particles passing through the matter at relativistic velocities loose the energy primarily by ionization of the medium. The average rate of the energy loss is given by the Bethe-Bloch formula [11]

$$-\frac{dE}{dx} = 2\pi N_A r_e^2 m_e c^2 \rho \frac{Z}{A} \frac{z^2}{\beta^2} \left[ln \frac{2 m_e c^2 \gamma^2 \beta^2 W_{max}}{I^2} - 2\beta^2 - \delta \right] , \qquad (A.1)$$

where:

- $N_A = 6.022 \times 10^{23} \mathrm{mol}^{-1}$ is the Avogadro's number,
- $r_e \approx 2.818$ fm – classical electron radius,
- $m_e c^2 \approx 0.511$ MeV – electron mass,
- ρ – density of the medium,
- Z – atomic number of medium,
- A – atomic mass of medium,
- z – particle charge,
- $I \approx 10$ eV – mean excitation energy,
- $\beta = v/c$ – particle velocity,
- $\gamma = 1/\sqrt{1-\beta^2}$,
- W_{max} – maximum kinetic energy that can be transferred to a free electron in a single collision,
- δ – correction factor due to the density of the medium.

The first term in brackets in Eq. A.1 varies slowly with particle velocity or momentum. It plays a dominant role at low velocities. The other terms can be treated as corrections, which are necessary at higher velocities.

In the leading order, dE/dx is inversely proportional to the velocity squared, and directly proportional to particle charge squared. Therefore, if particle velocity and dE/dx is measured, as in the case of Plastic Wall or CDC-Barrel combined measurements, particles charge can be easily determined from the relation

$$-\frac{dE}{dx} \propto \frac{z^2}{\beta^2} \, . \tag{A.2}$$

In the case of CDC measurements, quite differently, the information about the dE/dx and the ratio (p/z) is provided. Since

$$-\frac{dE}{dx} \propto \frac{z^2}{\beta^2} = z^2 + \frac{(mc)^2}{(p/z)^2} \, , \tag{A.3}$$

in this situation, the mass of a particle can be determined if the particle charge is assumed to equal 1, 2 or more units. And vice versa, particle charge can be deduced only if particle mass is known. This is of course more complicated, and implies that particle charge determination from the CDC measurements is difficult.

A.2 Kinematical variables

In heavy-ion physics at intermediate energies the following kinematical variables are commonly used to describe the momentum space.

In the transverse direction :

- p_t – transverse momentum,
- $m_t c = \sqrt{(p_t c)^2 + (m_0 c^2)^2}$ – transverse mass,
- $<p_x>/m_0 c$ – the mean value of the in-plane component of the transverse momenta (i.e., the mean value of the projection of the transverse momenta onto the reaction plane) normalized to particle mass.

In the longitudinal direction :

- $y = 1/2 \cdot \ln(\frac{E+p_z}{E-p_z})$ – rapidity,
- $y^{(0)} = y/y^{CM}$-1 – normalized rapidity, i.e., rapidity normalized to the rapidity of the center-of-the-momentum reference frame (y^{CM}); for a mass symmetric system -1, 1, and 0 correspond to target-, projectile-, and the center-of-the-momentum-rapidity respectively; the center-of-the-momentum-rapidity is usually called mid-rapidity.

In the case of the mass symmetric system and the beam at kinetic energy of 1.69 GeV per nucleon, y^{CM} equals 0.845.

A.3 Radially-expanding, thermally-equilibrated source

In the following,

- A is the overall normalization,
- T denotes the temperature of the source,
- β_{flow} is the common velocity of the radial expansion,
- $\gamma = \left(\sqrt{1-\beta_{flow}^2}\right)^{-1}$,
- $\alpha = \gamma\beta_{flow}(pc)/T$,
- p, E, E^{kin}, $y^{(0)}$, p_t and m_t are the momentum, the total and the kinetic energies, the normalized rapidity, the transverse momentum and the transverse mass of a particle respectively,
- y^{CM} is the rapidity of the center-of-the-momentum reference frame.

Within this notation, the distribution of particles emitted isotropically from a thermally-equilibrated source of temperature T, which expands radially with the flow velocity β_{flow} is given by the formula [70, 91]

$$\frac{d^2N}{dE^{kin}d\Omega} = A(pc)Ee^{-\gamma E/T}[(\gamma + \frac{T}{E})\frac{\sinh(\alpha)}{\alpha} - \frac{T}{E}\cosh(\alpha)]\ [st^{-1}\cdot GeV^{-1}]\ . \tag{A.4}$$

Since [11]

$$\frac{dN}{4\pi(pc)dE} = E\frac{d^3N}{d(pc)^3} = \frac{d^2N}{\pi d(p_tc)^2dy}\ , \tag{A.5}$$

the formula can be rewritten as

$$\frac{d^2N}{d(p_tc)dy^{(0)}} = A(m_tc^2)^2\frac{\cosh(y^{(0)}y^{CM})}{y^{CM}}e^{-\gamma E/T}[(\gamma+\frac{T}{E})\frac{\sinh(\alpha)}{\alpha} - \frac{T}{E}\cosh(\alpha)]\ [c/GeV]\ . \tag{A.6}$$

There is no analytical formula describing the rapidity-density distribution of particles, $dN/dy^{(0)}$. The expression A.6 has to be integrated numerically from p_t=0 to p_t=∞ in order to derive the appropriate spectrum.

A.4 RBUU transport model

The most commonly used, microscopic models which aim at the description of heavy-ion reaction dynamics can be subdivided into two classes, according to the technical realization of the modelling but regardless of the basic assumptions and the input information, which may be similar for models of both types.

One of them, the Quantum Molecular Dynamics (QMD) [2, 3] and many of its flavours [92], model heavy-ion collisions by following the n-body phase-space distribution. Each particle is represented by an individual gaussian wave-packet $\phi_i(\boldsymbol{r}_i, \boldsymbol{p}_i, t)$. The propagation of the wave-packets is governed by the Hamilton's equations,

$$\dot{\boldsymbol{p}}_i(t) = -\nabla_{\boldsymbol{r}_i} H \ , \qquad \dot{\boldsymbol{r}}_i(t) = \nabla_{\boldsymbol{p}_i} H \ . \tag{A.7}$$

The potential part of the Hamiltonian depends on the model assumptions. Usually it consists of the Coulomb part, the finite range Yukava-potential, and that of the Skyrme-like contact force $U{=}\alpha(\rho/\rho_0){+}\beta(\rho/\rho_0)^\gamma$. The Yukava-potential assures the existence of the nuclear surface (prevents nucleons from being spontaneously emitted from the nuclei in the ground state). The parameters of the Skyrme force (α, β, γ) are adjusted in order to describe the ground state of the nuclear matter and the desired equation of state. The local density, ρ, at a given moment is calculated from the actual distribution of particles, taking into account proper weights due to the Gaussian widths. In this way, particles propagate in a self-consistent mean field. Any in-medium effects can be easily added to the above scheme by modifying the potential part of the Hamiltonian in accordance to local conditions.

In addition, particles collide with each other when the minimal distance between the centroids of the Gaussians (d_0) fulfills the requirement

$$d_0 < \sqrt{\sigma/\pi} \ . \tag{A.8}$$

The considered reaction channels, the cross sections (σ), and their dependence on the local density and relative particle momenta depend on the version of the code.

In this work, the experimental results are compared to the predictions of the Relativistic Boltzmann-Uehling-Uhlenbeck (RBUU) model of the Giessen group [81], which belongs to a second class of microscopic models. Like other realizations of BUU-type models [4, 5], as well as Vlasov-Uehling-Uhlenbeck (VUU) [93], or Landau-Vlasov (LV) [94] models, the RBUU model considered in this work follows the evolution of the one-body phase-space density $f(\boldsymbol{r}, \boldsymbol{p}, t)$ according to the equation

$$\begin{aligned}\frac{\partial f}{\partial t} &+ \boldsymbol{v}\cdot\nabla_{\boldsymbol{r}} f - \nabla_{\boldsymbol{r}} U \cdot \nabla_{\boldsymbol{p}} f = \sum_{coll} \int \mathrm{d}^3p'_1 \mathrm{d}^3p'_2 \mathrm{d}^3p_2 \frac{\mathrm{d}\sigma}{\mathrm{d}\omega} \\ &\times \ (f f_2 (1-f'_1)(1-f'_2) - f'_1 f'_2 (1-f)(1-f_2)) \times \delta^4(p + p_2 - p'_1 - p'_2) \end{aligned} \tag{A.9}$$

The l.h.s of the above equation set to zero would be a Vlasov equation, describing the evolution of the single-particle density distribution in a self-consistently generated mean-field potential U. The sum on the r.h.s of Eq. A.9 runs over all considered reaction channels. Each term under the sum depends on the reaction cross section, σ, for a process in which the considered particle collides with particle (2) both going into the final state (1′,2′). The collision terms include the Pauli-blocking part $f f_2(1-f'_1)(1-f'_2) - f'_1 f'_2(1-f)(1-f_2)$ and the part which assures the momentum conservation $\delta^4(p + p_2 - p'_1 - p'_2)$. For processes with three or more particles in the final state, the collision terms are modified accordingly.

Eq. A.9 is solved numerically by following the propagation of $(A_{proj} + A_{targ})$ test particles in a parallel n-event method. Usually n is chosen between 150 and 500 in order to avoid too much statistical fluctuations. The propagation is governed by the Hamilton's equation of motion, like in the case of QMD-type models. Also the mean-field potential, U, is introduced in a similar way. The main difference from QMD-type models lies in calculating the local conditions in order to derive U. In BUU-type simulation they are taken as the average from all the parallel events.

The one-body phase-space density is then given by

$$f(\boldsymbol{r},\boldsymbol{p},t) = \frac{1}{n} \sum_{i=1}^{n\times(A_{proj}+A_{targ})} \delta(\boldsymbol{r} - \boldsymbol{r}_i)\delta(\boldsymbol{p} - \boldsymbol{p}_i) \ . \tag{A.10}$$

Only particles from the same event can make binary collisions. Their occurrence is checked in the same way as in the case of QMD-type models (cf. Eq. A.8).

In the RBUU model considered in this work, the most important K^+ and K^- meson production channels are :

$$\begin{gathered} \mathrm{NN} \to \mathrm{NK}^+\mathrm{Y} \ , \quad \Delta\mathrm{N} \to \mathrm{NK}^+\mathrm{Y} \ , \quad \Delta\Delta \to \mathrm{NK}^+\mathrm{Y} \ , \\ \pi\mathrm{N} \to \mathrm{K}^+\mathrm{Y} \ , \\ \mathrm{NN} \to \mathrm{NNK}^+\mathrm{K}^- \ , \quad \pi\mathrm{N} \to \mathrm{NK}^-\mathrm{K}^{+,0} \ , \quad \pi\mathrm{Y} \to \mathrm{NK}^- \ , \end{gathered} \tag{A.11}$$

where Y denotes Λ or Σ hyperons.

The parametrization of the dependence of the production cross sections on the energy above the threshold, $\sigma{=}\sigma(\sqrt{s} - \sqrt{s_0})$, is based on the available data from elementary processes, including the near-threshold measurements from COSY [95]. Here $\sqrt{s}$ is the energy in the center-of-the-momentum reference frame of colliding particles, and $\sqrt{s_0}$ is the threshold energy of a given process. A full list of the considered production channels and parametrization of the cross sections can be found in [81]. Because of small cross sections, the production of K^+ and K^- mesons is treated perturbatively, which implies that hadrons in the input channel of the production processes are not changed, and the dynamical feedback from the mesons to the rest of the system is neglected.

K^+ and K^- mesons propagate according to the Hamilton's equations,

$$\dot{\boldsymbol{p}}(t) = -\nabla_{\boldsymbol{r}}(\omega_K) \ , \qquad \dot{\boldsymbol{r}}(t) = \nabla_{\boldsymbol{p}}(\omega_K) \ , \tag{A.12}$$

where ω_K is meson self-energy. When no in-medium effects are considered $(\omega_K^0)^2 = (m_K^2 + \boldsymbol{p}_K)$ and the second equation expresses the energy conservation law.

Mesons also make binary collisions with other particles in order to account for elastic and inelastic final-state interactions. The most dominant K^- meson absorption channel is the reversed process $\pi\mathrm{Y}{\leftarrow}\mathrm{NK}^-$.

In-medium modifications of meson self-energies show up in two different ways. First of all, the change of ω_K implies the change of the effective mass

$$m_K^\star = \omega_K(\boldsymbol{p} = 0) \ . \tag{A.13}$$

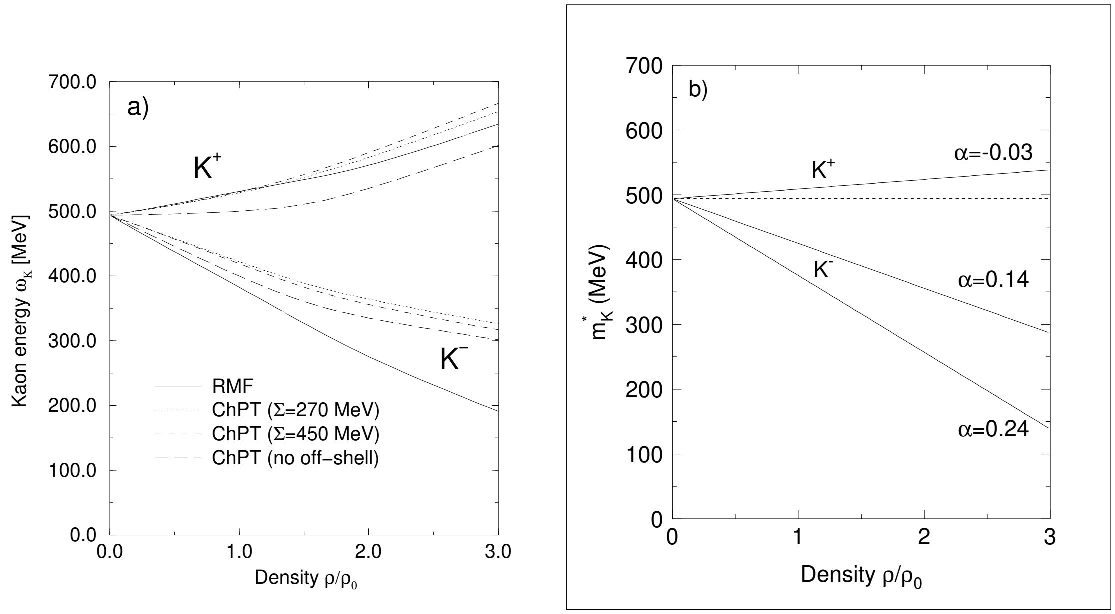

Figure A.1: *(a) The self-energies of K^+ and K^- mesons as a function of the medium density. The results obtained within the chiral perturbation theory (ChPT) and from the Walecka-type relativistic mean-field model (RMF) assuming the hard equation of state are shown. The plot is adapted from [39]. (b) Different parametrizations of the effective K^+ and K^- meson masses used in the RBUU model considered in this work.*

Because of this, the production threshold energy, $\sqrt{s_0}$, and the production cross sections, $\sigma(\sqrt{s} - \sqrt{s_0})$, get modified accordingly.

Secondly, the modification of the self-energy is equivalent to the existence of an effective potential defined as

$$U_{eff} = \omega_K - \omega_K^0 \ , \tag{A.14}$$

of which the gradient will show up in the second Hamilton's equation A.12. This will modify the propagation of particles through the medium, and change the final-state momentum-space distributions.

A detailed form of the kaon self-energy, ω_K, in the medium is a matter of debate. However, qualitatively different theoretical approaches come to similar conclusions, namely, that kaons feel in the medium a moderately repulsive potential, while antikaons experience a strong attractive force. In Figure A.1a the self-energies of K^+ and K^- mesons are shown as a function of the medium density. The results obtained within the chiral perturbation theory (labelled ChPT) and from the Walecka-type relativistic mean-field model (labelled RMF) are shown.

In the RBUU model considered in this work, K^+ and K^- meson self-energies are derived from the ChPT. In the leading order they are given by

$$\omega_{K\pm} = \left\{ \boldsymbol{p}^2 + m_K^2 \left(1 - \frac{\Sigma_{KN}}{f_K^2 m_K} \rho_S + \left(\frac{3\rho_N}{8 f_K^2 m_K} \right)^2 \right) \right\}^{1/2} \pm \frac{3\rho_N}{8 f_K^2} \ . \tag{A.15}$$

In the above formula, ρ_N is baryon density, ρ_s (the scalar density of nucleons) is approximately equal to ρ_N, f_K denotes the kaon decay constant and equals 93 MeV. The kaon-nucleon sigma term, Σ_{KN}, is determined from KN scattering lengths [43, 44]. However, the actual value is model dependent, and may vary from 270 to 450 MeV. The term proportional to Σ_{KN} gives rise to an attractive scalar effective potential for both K^+ and K^- mesons. On the other hand, there exist a vector part of the effective potential, which is attractive for K^- mesons and repulsive for K^+ mesons (the terms with ρ_N). Therefore, in total, the in-medium potential is strongly attractive for K^- mesons and slightly repulsive for K^+ mesons.

Since the value of Σ_{KN} is not known precisely, there are large uncertainties about the strength of in-medium effects on K^+ and K^- mesons (compare the results in Figure A.1a for different values of Σ_{KN}). Because of this and in order to simplify the calculations, in the RBUU model considered in this work, the change of K^+ and K^- meson masses is effectively parametrized by the linear dependence [81]

$$m_K^\star = m_K \left(1 - \alpha \frac{\rho}{\rho_0} \right) \ . \tag{A.16}$$

The experimental results are compared to predictions of the RBUU model with different values of α :

- $\alpha_{K^+,K^-} = 0$, i.e., no in-medium effects on kaons,
- $\alpha_{K^+} = -0.03$ and $\alpha_{K^-} = 0.24$, leading to a 15 MeV increase of the K^+ meson effective mass and a 120 MeV drop of the K^- meson effective mass at the normal nuclear matter density,
- $\alpha_{K^+} = -0.03$ and $\alpha_{K^-} = 0.14$, corresponding to less attraction of K^- mesons, i.e., a 70 MeV drop of the K^- meson effective mass at the normal nuclear matter density.

Figure A.1b shows the change of the effective masses of K^+ and K^- mesons with the density of the medium resulting from the above parametrization.

Bibliography

[1] H. Stöcker, W. Greiner, "*High energy heavy ion collisions – probing the equation of state of highly excited hadronic matter*", Phys. Rep. 137 (1986) 277

[2] J. Aichelin, H. Stöcker, "*Quantum molecular dynamics – a novel approach to n-body correlations in heavy-ion collisions*", Phys. Lett. B176 (1986) 14

[3] J. Aichelin, "*Quantum molecular dynamics – a dynamical microscopic n-body approach to investigate fragment formation and the nuclear equation of state in heavy-ion collisions*", Phys. Rep. 202 (1991) 233

[4] G. F. Bertsch, H. Kurse, S. Das Gupta, "*Boltzmann equation for heavy ion collisions*", Phys. Rev. C29, (1984) R673

[5] J. Aichelin, G. Bertsch, "*Numerical simulation of medium energy heavy-ion collisions*", Phys. Rev. C31 (1985) 1730

[6] G. Roche et al., "*Dielectron production in Ca+Ca collisions at 1.0 and 2.0 A GeV*", Phys. Rev. B226 (1989) 228

[7] R. J. Porter et al., "*Dielectron cross section measurements in nucleus-nucleus reactions at 1.0 A GeV*", Phys. Rev. Lett. 79 (1997) 1229

[8] The HADES Collaboration, "*Letter of intent for a High Acceptande Di-Electron Spectrometer*", GSI 1993, "*Technical proposal for a High Acceptande Di-Electron Spectrometer*", GSI 1994

[9] E. Bratkovskaya, W. Cassing, U. Mosel, "*Analysis of kaon production at SIS energies*", Nucl. Phys. A622 (1997) 593

[10] D. Miśkowiec et al., "*Observation of enhanced subthreshold K^+ production in central collisions between heavy ions*", Phys. Rev. Lett. 72 (1994) 3650

[11] Particle Data Group, "*Particle physics booklet*"

[12] C. B. Dover, G. E. Walker, "*The interaction of kaons with nucleons and nuclei*", Phys. Rep. 89 (1982) 1

[13] A. S. Carroll et al., "*Structure in K^--nucleon total cross sections below 1.1 GeV/c*", Phys. Rev. Lett. 37 (1976) 806

[14] R. W. Bland et al., "*The K^+-p interaction from 864 to 1585 MeV/c; cross section and mass distributions*", Nucl. Phys. B13 (1969) 595

[15] C. J. S. Damerell et al., "*K^+-n elastic and charge-exchange scattering between 430 and 940 MeV/c*", Nucl. Phys. B94 (1975) 374

[16] M. Ankina et al., "Λ *hyperon produced in central nucleus-nucleus interactions at 4.5 GeV/c momentum per incident nucleon*", Phys. Rev. Lett. 50 (1983) 1971

[17] M. Ankina et al., "*Characteristics of Λ and K^0 particles in central nucleus-nucleus collisions at 4.5 GeV/c momentum per incident nucleon*", Z. Phys. C25 (1984) 1

[18] J. W. Harris et al., "Λ *production near threshold in central nucleus-nucleus collisions*", Phys. Rev. Lett. 47 (1981) 229

[19] S. Schnetzer et al., "*Production of K^+ mesons in 2.1 GeV/nucleon nuclear collisions*", Phys. Rev. Lett. 49 (1982) 989

[20] A. Shor et al., "*Subthreshold antiproton, K^-, K^+, and energetic-pion production in relativistic nucleus-nucleus collisions*", Phys. Rev. Lett. 63 (1989) 2192

[21] A. Schröter et al., "*Subthreshold antiproton and K^- production in heavy-ion collisions*", Z. Phys. A350 (1994) 101

[22] J. Aichelin, C. M. Ko, "*Subthreshold kaon production as a probe of the nuclear equation of state*", Phys. Rev. Lett. 55 (1985) 2661

[23] P. Senger, H. Ströbele, "*Hadronic particle production in nucleus-nucleus collisions*" J.Phys. G25 (1999) R59

[24] C. Hartnack et al., "*Kaon production at subthreshold energies*", Nucl. Phys. A580 (1994) 643

[25] G. Q. Li, C. M. Ko, "*Subthreshold Kaon production and the nuclear equation of state* ", Phys. Lett. B349 (1995) 405

[26] D. Best et al., "*K^+ production in Ni+Ni collisions at incident energies between 1 and 2 A GeV*", Nucl. Phys. A625 (1997) 307

[27] J. Stachel, "*Tests of thermalization in relativistic nucleus-nucleus collisions*", Nucl. Phys. A610 (1996) 509c

[28] W. Weise, "*Hadrons in dense matter*", Nucl. Phys. A574 (1994) 347c

[29] V. Koch, "*Aspects of chiral symmetry*", Int. J. Mod. Phys. E6 (1997) 203

[30] S. Klimt et al., "*Generalized SU(3) Nambu-Jona-Lasinio model*", Nucl. Phys. A516 (1990) 429,469

[31] J. Gasser, H. Leutwyler, "*Quark Masses*", Phys. Rep. 87 (1982) 77

[32] J. F. Donoghue, "*Light quark masses and chiral symmetry*", Annu. Rev. Nucl. Part. Sci. 39 (1989) 1

[33] M. Lutz, S. Klimt, W. Weise, "*Meson properties at finite temperature and baryon density*", Nucl. Phys. A542 (1992) 521

[34] M. Lutz, A. Steiner, W. Weise, "*Kaon in baryonic matter*", Nucl. Phys. A574 (1994) 755

[35] C. M. Ko, V. Koch, G. Q. Li, "*Properties of hadrons in the nuclear medium*", Annu. Rev. Nucl. Part. Sci. 47 (1997) 505

[36] D. B. Kaplan, A. E. Nelson, "*Strange goings on in a dense nucleonic matter*" Phys. Lett. B175 (1986) 57

[37] A. E. Nelson, D. B. Kaplan "*Strange condensate realignment in relativistic heavy ion collisions*" Phys. Lett. B192 (1987) 193

[38] V. Koch, "*K^--proton scattering and $\Lambda(1405)$ in dense matter*", Phys. Lett. B337 (1994) 7

[39] J. Schaffner-Bielich, I. N. Mishustin, J. Bondorf, "*In-medium kaon production at the mean-field level*", Nucl. Phys. A625 (1997) 325

[40] G. Q. Li C.-H. Lee, G. E. Brown "*Kaons in dense matter, kaon production in heavy-ion collisions, and kaon condensation in neutron stars*", Nucl. Phys. A625 (1997) 372

[41] E. Friedman, A. Gal, C. J. Batty, "*K^+ nucleus reaction and total cross sections: new analysis of transmission experiments*", Phys. Rev. C55 (1997) 1304

[42] E. Friedman et al., "*Density dependence in kaonic atoms*", Phys. Lett. B308 (1993) 6

[43] A. D. Martin, "*Kaon-nucleon parameters*", Nucl. Phys. B179 (1981) 33

[44] T. Barnes, E. S. Swanson, "*Kaon-nucleon scattering amplitudes and Z^* enhancements from quark Born diagrams*", Phys. Rev. C49 (1994) 1166

[45] R. Barth et al., "*Subthreshold production of kaons and antikaons in nucleus-nucleus collisions at equivalent beam energies*", Phys. Rev. Lett. 78 (1997) 4007

[46] J. Schaffner-Bielich, V. Koch, M. Effenberger, "*Medium modified cross sections, temperature and finite momentum effects for antikaon production in heavy-ion collisions*", Nucl. Phys. A669 (2000) 153

[47] J. L. Ritman et al., "*On the transverse momentum distribution of strange hadrons produced in relativistic heavy ion collisions*", Z. Phys. A352 (1995) 355

[48] G. Q. Li, G. E. Brown, "K^+ *versus* Λ *flow in relativistic heavy-ion collisions*", Nucl. Phys. A636 (1998) 487

[49] C. Fuchs et al., "*Consequences of covariant kaon dynamics in heavy-ion collisions*", Phys. Lett. B434 (1998) 245

[50] C. David, C. Hartnack, J. Aichelin, "*On the flow of kaons produced in relativistic heavy-ion collisions*", Nucl. Phys. A650 (1999) 358

[51] Y. Shin et al., "*Enhanced out-of-plane emission of K+ mesons observed in Au+Au collisions at 1 A GeV*", Phys. Rev. Lett. 81 (1998) 1576

[52] A. Gobi et al., "*A highly-segmented* ΔE*-time-of-flight wall as forward detector of the* 4π*-system for charged particles at the SIS/ESR accelerator*", Nucl. Instr. Meth. A324 (1993) 156

[53] J. L. Ritman et al., "*The FOPI detector at SIS/GSI*", Nucl. Phys. B44 (1995) 708

[54] J. P. Alard et al., "*Midrapidity source of intermediate-mass fragments in highly central collisions of Au + Au at 150A MeV*", Phys. Rev. Lett. 69 (1992) 889

[55] C. Kuhn et al., "*Entropy production in the Au + Au reaction between 150 and 800 A MeV*", Phys. Rev. C48 (1993) 1232

[56] G. Poggi et al., "*Evidence for collective expansion in light-particle emission following Au + Au collisions at 100, 150 and 250A MeV*", Nucl. Phys. A586 (1995) 755

[57] M. Petrovici et al., "*Cluster formation during expansion of hot and compressed nuclear matter produced in central collisions of Au on Au at 250A MeV*", Phys. Rev. Lett. 74 (1995) 5001

[58] P. Crochet et al., "*Onset of nuclear matter expansion in Au+Au collisions*", Nucl. Phys. A624 (1997) 755

[59] D. Pelte et al., "*Charged pions from Ni on Ni collisions between 1 and 2 A GeV*", Z. Phys. A 359 (1997) 55

[60] M. Eskef et al., "*Identification of baryon resonances in central heavy-ion collisions at energies between 1 and 2 A GeV*", Eur. Phys. J. A. 3 (1998) 335

[61] D. Best, "*Production of positively charged Kaons in the system Ni+Ni at 1.45 and 1.93 A GeV*", PhD thesis, Ruprecht-Karls-Universität Heidelberg, 1996

[62] M. Kirejczyk, "*Identification and investigation of charged K mesons in FOPI spectrometer*", PhD thesis, Warsaw University, 2000

[63] C. Pinkenburg, "*Flow effects of charged pions in the system Au + Au at E = 1 A GeV*", PhD thesis, Ruprecht-Karls-Universität Heidelberg, 1995

[64] G. Goebels, "*Investigation of the Bose-Einstein correlations of charged pions in relativistic heavy-ion collisions of the systems Au + Au and Ni + Ni in the energy range from 1 A GeV to 2 A GeV*", PhD thesis, Ruprecht-Karls-Universität Heidelberg, 1995

[65] C. Plettner, "*Strangenesspoduktion bei kleinen transversalen Impulsen und mittleren Rapiditten in der Reaktion Ru+Ru at 1.69 A GeV*", PhD thesis, Technische Universität Dresden, 1999

[66] C. Cavata et al., "*Determination of impact parameter in relativistic nucleus-nucleus collisions*", Phys. Rev. C42 (1990) 1760

[67] J. Gosset et al., "*Central collisions of relativistic heavy ions*", Phys. Rev. C16 (1977) 629

[68] P. Danielewicz, G. Odyniec, "*Transverse momentum analysis of collective motion in relativistic nuclear collisions*", Phys. Lett. B157 (1985) 146

[69] J.-Y. Ollitrault, "*Reconstructing azimuthal distributions in nucleus-nucleus collisions*", Los Alamos preprint nucl-ex/9711003, submitted to Phys. Rev. C

[70] P. J. Siemens, J. O. Rassmussen, "*Evidence for a blast wave from compressed nuclear matter*", Phys. Rev. Lett. 42 (1979) 880

[71] W. Reisdorf et al., "*Central collisions of Au on Au at 150, 250 and 400 AMeV*", Nucl. Phys. A612 (1997) 493

[72] B. Hong et al., "*Abundance of Δ resonances in 58Ni+58Ni collisions between 1 and 2 A GeV*", Phys. Lett. B407 (1997) 115

[73] B. Hong et al., "*Stopping and radial flow in central nucleus-nucleus collisions between 1 and 2 GeV per nucleon*", Phys. Rev. C57 (1998) 244, Phys. Rev. C58 (1998) 603

[74] A. Andronic, "*New aspects on collective phenomena in relativistic heavy-ion collisions*", PhD thesis, NIPNE Bucharest, 1998

[75] C. A. Ogilvie et al., "*Transverse collective motion in intermediate-energy heavy-ion collisions*", Phys. Rev. C40 (1989) 2592

[76] P. Crochet et al., "*Sidewards flow of K^+ mesons in Ru+Ru and Ni+Ni reactions near threshold*", Phys. Lett. B in print

[77] P. Senger et al., "*Kaon production in relativistic nucleus-nucleus collisions*", Acta Phys. Pol. B27 (1996) 2993

[78] V. Metag, "*Near-threshold particle production : a probe for resonance matter formation in relativistic heavy ion collisions*", Prog. Part. Nucl. Phys. 30 (1993) 75

[79] N. Herrmann, "*Particle production and flow at SIS energies*", Nucl. Phys. A610 (1996) 49c

[80] E. Bratkovskaya et al., "*Aspects of thermal and chemical equilibration of hadronic matter*", Los Alamos preprint nucl-th/0001008, Nucl. Phys. A in press

[81] W. Cassing et al., "*Kaon versus antikaon production at SIS energies*", Nucl. Phys. A614 (1997) 415

[82] R. Kutsche, "*Untersuchungen der In-medium-Eigenschaften von K^0_s-Mesonen und Λ-Hyperonen an der Produktionsschwelle*", PhD thesis, Technische Universität Darmstadt, 2000

[83] Z. S. Wang et al., "*Role of the Coulomb interaction in the flow and the azimuthal distribution of kaons from heavy ion reactions*", Nucl. Phys. A628 (1998) 151

[84] K. Wiśniewski et al., "*Direct comparison of phase-space distributions of K^- and K^+ mesons in heavy-ion collisions at SIS energies – Evidence for in-medium modifications of kaons ?*", submitted to Eur. Phys. J. A

[85] F. Laue et al., "*Medium effects in kaon and antikaon production in nuclear collisions at subthreshold beam energies*", Phys. Rev. Lett. 82 (1999) 1640

[86] C. A. Ogilvie, "*Kaon production and multi-body collisions in dense nuclear matter*", Phys. Lett. B436 (1998) 238

[87] G. Q. Li, G. E. Brown, "*K^-/K^+ ratios in relativistic heavy-ion collisions*", Phys. Rev. C58 (1998) 1698

[88] A. Ayala, J. Kapusta, "*Coulomb effects on charged kaon distributions from Vlasov dynamics*", Phys. Rev. C56 (1997) 407

[89] H. W. Barz et al., "*Coulomb effects on particle spectra in relativistic nuclear collisions*", Phys. Rev. C57 (1998) 2536

[90] W. H. Press et al., "*Numerical Recipes in C (second edition)*", ISBN 0-521-43108-5, Cambridge University Press (1992) 707

[91] M. Lisa et al., "*Radial flow in Au+Au collisions at E=0.25 - 1.15 A GeV*", Phys. Rev. Lett. 75 (1995) 2662

[92] C. Hartnack et al., "*Modelling the many-body dynamics of heavy-ion collisions: present status and future perspective*", Eur. Phys. J. A1 (1998) 151

[93] H. Kruse et al., "*Vlasov-Uehling-Uhlenbeck theory of medium energy heavy-ion reactions: role of mean field dynamics and two-body collisions*", Phys. Rev. C31 (1985) 1770

[94] C. Gregoire et al., "*Semi-calssical dynamics of heavy-ion reactions*", Nucl. Phys. A465 (1987) 317

[95] J. T. Balewski et al., "Λ *hyperon production via* $pp \rightarrow pK^{+}\Lambda$ *reaction 2 MeV above threshold*" Phys. Lett. B388 (1996) 859, "*Meson production in p+p interaction at threshold*", Acta Phys. Pol. B27 (1996) 2911

Acknowledgments

First, I shall acknowledge the Nuclear Physics Division at the Warsaw University. In particular I owe to :

- Prof. dr hab. K. Siwek-Wilczyńska for her kind and careful supervision of all my scientific efforts and for taking a real care of other aspects of my work at Warsaw University.
- Dr Brunon Sikora for his very valuable help in solving many of the problems connected to this project and answering many of my questions.
- Dr Marek Kirejczyk for his kind assistance, fruitful discussions, and careful reading of the manuscript.

I shall also express my gratitude to the KP1/FOPI group in GSI Darmstadt for their remarkable hospitality and care during my fruitful stay there. In particular I am indebted to :

- Prof. dr hab. P. Braun–Munzinger, the head of KP1 division, who enabled me to work in GSI.
- Dr K. Hildenbrand, dr W. Reisdorf and dr A. Gobbi for kind assistance in my scientific activities.
- Prof. dr hab. N. Herrmann, the FOPI collaboration spokesperson, whose participation in my research work could not be possibly overemphasized.
- Dr. P. Crochet, dr R. Kutsche, dr A. Andronic, A. Devismes and T. Kress for a wonderful atmosphere I had in GSI.

I am very grateful to prof W. Cassing and dr E. Bratkovskaya from Universität Giessen for providing me with the results of the RBUU simulations.

Last, but not least, I shall thank a lot my mother who supported me all the time like only she could do.